Defense Threat Reduction Agency
8725 John J. Kingman Road, Stop 6201
Fort Belvoir, VA 22060-6201

DTRA-TR-24-02

Spatiotemporal Evolution of High-Density Surface Plasmas Produced by Prompt X-rays

FINAL REPORT

13 October 2023

PI: Dr. Miloshevsky, Email:gennady@vcu.edu

Virginia Commonwealth University

Cleared For Public Release

REPORT DOCUMENTATION PAGE

Form Approved
OMB No. 0704-0188

Public reporting burden for this collection of information is estimated to average 1 hour per response, including the time for reviewing instructions, searching existing data sources, gathering and maintaining the data needed, and completing and reviewing this collection of information. Send comments regarding this burden estimate or any other aspect of this collection of information, including suggestions for reducing this burden to Department of Defense, Washington Headquarters Services, Directorate for Information Operations and Reports (0704-0188), 1215 Jefferson Davis Highway, Suite 1204, Arlington, VA 22202-4302. Respondents should be aware that notwithstanding any other provision of law, no person shall be subject to any penalty for failing to comply with a collection of information if it does not display a currently valid OMB control number. **PLEASE DO NOT RETURN YOUR FORM TO THE ABOVE ADDRESS.**

1. REPORT DATE *(DD-MM-YYYY)*	2. REPORT TYPE	3. DATES COVERED *(From - To)*
10/13/2023	Final Report	03/23/2018-06/05/2023

4. TITLE AND SUBTITLE
Spatiotemporal Evolution of High-Density Surface Plasmas Produced by Prompt X-rays

5a. CONTRACT NUMBER

5b. GRANT NUMBER
HDTRA1-19-1-0019

5c. PROGRAM ELEMENT NUMBER

6. AUTHOR(S)
Miloshevsky Gennady

5d. PROJECT NUMBER

5e. TASK NUMBER

5f. WORK UNIT NUMBER

7. PERFORMING ORGANIZATION NAME(S) AND ADDRESS(ES) AND ADDRESS(ES)
Virginia Commonwealth University
Department of Mechanical and Nuclear Engineering
P.O. Box 843015
401 West Main Street, Richmond, VA 23284-3015

8. PERFORMING ORGANIZATION REPORT NUMBER

9. SPONSORING / MONITORING AGENCY NAME(S) AND ADDRESS(ES)
Defense Threat Reduction Agency/RD-NTS
8725 John J. Kingman Rd., MSC 6201
Ft. Belvoir, VA 22060-6201

10. SPONSOR/MONITOR'S ACRONYM(S)
DTRA/RD-NTS

11. SPONSOR/MONITOR'S REPORT NUMBER(S)
DTRA-TR-24-02

12. DISTRIBUTION / AVAILABILITY STATEMENT
Cleared for Public Release

13. SUPPLEMENTARY NOTES

14. ABSTRACT
A major effect of prompt cold X-rays released from a high-altitude nuclear detonation to a few microns of satellite surface materials is surface vaporization, ionization, and generation of high-density blow-off plasma. The physics mechanisms of cold X-ray absorption by metallic and dielectric materials, formation and expansion phases of produced warm and hot dense plasmas, and their optical and electrical properties are studied using an integration of high-fidelity computational models. The results provide valuable information for the basic science of cold X-ray effects on solar cell panels of satellites.

15. SUBJECT TERMS
Exo-atmospheric nuclear burst, cold X-rays, satellite's materials, solar cell panels, warm dense plasma, blow-off, dense plasma composition, optical and electrical properties, radiative transfer in plasmas

16. SECURITY CLASSIFICATION OF:			17. LIMITATION OF ABSTRACT	18. NUMBER OF PAGES	19a. NAME OF RESPONSIBLE PERSON
a. REPORT	b. ABSTRACT	c. THIS PAGE			Jacob Calkins
Unclassified	Unclassified	Unclassified	Unclassified	112	19b. TELEPHONE NUMBER *(include area code)* (510) 616-4033

FINAL REPORT

Grants No: HDTRA1-18-1-0025 and HDTRA1-19-1-0019

Project title: Spatiotemporal Evolution of High-Density Surface Plasmas Produced by Prompt X-rays

Recipient: Virginia Commonwealth University, Department of Mechanical and Nuclear Engineering, 401 West Main Street, P.O. Box 843015, Richmond, VA 23284-3015

PI: Dr. Miloshevsky, Phone: 804-827-0990, Email: gennady@vcu.edu

Period covered: March 23, 2018 - June 5, 2023

Date of report: October 13, 2023

DISCLAIMER

This report was prepared as an account of work sponsored by an agency of the United States Government. Neither the United States Government nor any agency thereof, nor any of their employees, makes any warranty, expressed or implied, or assumes any legal liability or responsibility for the accuracy, completeness, or usefulness of any information, apparatus, product, or process disclosed, or represents that its use would not infringe privately owned rights. Reference herein to any specific commercial product, process, or service by trade name, trademark, manufacturer, or otherwise does not necessarily constitute or imply its endorsement, recommendation, or favoring by the United States Government or any agency thereof. The views and opinions of authors expressed herein do not necessarily state or reflect those of the United States Government or any agency thereof.

Contents

Abstract

A high-altitude nuclear burst can radiate 70 to 80 percent of its released energy as X-rays. A major effect of prompt cold X-rays (~1 keV) to a few microns of satellite surface materials is surface vaporization, ionization, generation of high-density plasma and blow-off. Solar cells are more susceptible to cold X-rays, since the large surface area is exposed to radiation and cannot be substantially shielded. Implications of X-ray irradiation of solar cells are potentially quite serious. The surface plasmas can couple the solar cells to each other and to dielectric structures causing them to be destroyed. The objective of the research is to explore the physics mechanisms of cold X-ray absorption by metallic and dielectric materials, formation and expansion phases of produced warm and hot dense plasmas (WDP and HDP), and their optical and electrical properties. The study of the fundamental physics of the formation and spatiotemporal evolution of WDPs is performed using the Monte Carlo (MC) and Molecular Dynamics (MD) methods coupled with the Hartree-Fock-Slater (HFS) - Collisional-Radiative Steady-State (CRSS) model. The performed research is multi-disciplinary in nature, and covers the physics of X-ray transport and absorption by materials, WDP/HDP blow-off into vacuum, radiative transfer and energy redistribution in WDP/HDP, and optical and electrical properties of dense plasmas. Assuming the presence of cold X-rays from a nuclear event, the transition from the stage of X-ray absorption to the stage of material ionization, formation of WDP, spatiotemporal evolution and properties of WDP/HDP are investigated. The knowledge of the fundamental physics of WDP/HDP states provides valuable information for the basic science of solar cell protection from cold X-ray radiation produced by a high-altitude nuclear explosion.

1. Introduction

A typical thin-film solar cell structure generally consists of multiple layers of different materials coated onto glass or metal substrate [1]. The potential damage from high altitude nuclear detonations releasing up to 80 percent of energy as X-rays is highly vulnerable to satellite solar cells [2, 3]. Solar cells are more susceptible to prompt X-rays than other satellite's structures, since the large surface area is exposed to radiation and cannot be substantially shielded. A major effect of cold X-rays (~1 keV) to a few microns of satellite surface materials is surface vaporization, ionization, generation of warm and hot high-density plasmas near the surface, and blow-off [4, 5]. The plasma produced below the surface of material irradiated by X-rays can have electron number densities up to ~10^{22}-10^{23} cm^{-3} nearing the density of a solid. Electron temperature in this warm dense plasma (WDP) is in the range of 1-100 eV (~11,600 K - 1,160,000 K). As WDP expands above the surface, it transits to the hot dense plasma (HDP) state with electron number densities of ~10^{21}-10^{23} cm^{-3} and temperatures >100 eV. Implications of X-ray irradiation of solar cells are potentially quite serious. The expanding WDP and subsequently HDP may dramatically influence the performance of solar arrays. The damage can be produced by the expanding plasma in the gap between adjacent cells by short-circuiting the cells causing them to be destroyed.

Despite a large amount of accumulated experimental and theoretical knowledge for explanation and prediction of WDP/HDP properties [6], the scientific challenges are interdisciplinary spanning many subfields [7-10]. A comprehensive model that can describe high-energy density plasmas in their entirety and complexity has not been developed yet. This is because the state of transient WDP/HDP is challenging for theoretical and computational studies [11-13]. A complex interplay between collective ion couplings and quantum effects is occurring in WDP,

since both the plasma coupling parameter as well as the degeneracy parameter are close to unity [14]. The thermal, Coulomb and Fermi energies are nearly equal. Therefore, it is very difficult to model the physics of WDP due to the lack of a dominating energy scale. A numerical tool aiming to predict the formation and evolution of WDP on solar panels due to X-ray irradiation effects is extremely important [15]. Such a tool, which can simulate the formation, spatiotemporal evolution, and physical properties of WDP/HDP would provide a guide for determining the risks associated with a particular design of solar panels.

1.1 Background and motivation

A typical thin-film solar cell structure generally consists of multiple layers of different materials coated on a substrate (Fig. 1) [1]. Solar cells can have many variations of designs, styles, and components [16].

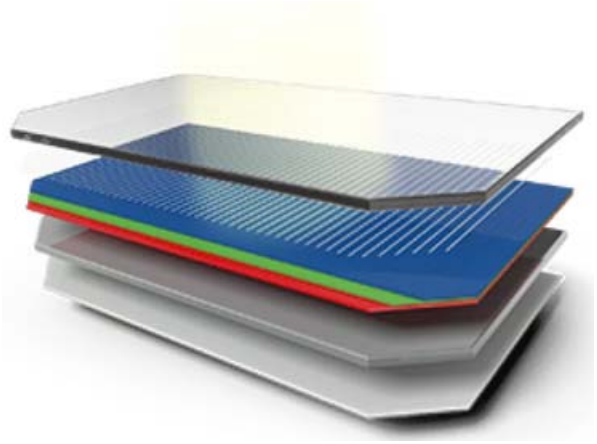

Fig. 1. Typical multiple layer solar cell structure.

A typical solar cell usually includes a metal frame for its installation, layers of anti-reflective coating, glass cover, multiple semiconductors, silicone glue, insulator and metal substrates, and metal junctions connecting a cell to the electric circuit. The multi-junction technology is used in solar cells for space applications [17]. The different semiconductor materials stacked on top of each other form multiple p-n junctions in cells. Separate layers of semiconductors (so called active element) are made of the materials like gallium indium phosphide (GaInP), indium gallium arsenide (InGaAs), and germanium (Ge) [18]. They respond to different wavelengths of incoming sunlight and have low temperature coefficient, high resistance to cosmic radiation, and much higher efficiency compared to that of single-junction cell designs.

For X-ray interaction with materials, the physical mechanisms are the photoelectric effect (and subsequent fluorescence), Compton scattering, and electron-positron pair production [19]. The photoelectric absorption dominates in the ultraviolet and cold X-ray regimes. In the photoelectric effect, a photon is absorbed by an atom with the subsequent ejection of an electron [20]. The atom may then fluoresce and emit a second photon of lower energy, or a second (Auger) electron may be emitted. Thus, a major effect of absorbed X-rays is the ionization of satellite surface materials and formation of warm high-density plasma near the surface.

The study of the absorption of cold X-rays in solar array materials and WDP evolution is performed using an integration of the Monte Carlo (MC) and Molecular Dynamics (MD) methods coupled with the Hartree-Fock-Slater (HFS) - Collisional-Radiative Steady-State (CRSS) model. To date, no integrated modeling on the atomistic scale has been performed on how cold X-rays can produce the expanding WDPs. Assuming the presence of cold X-rays from a nuclear event, the transition from the stage of X-ray transport and absorption to the stage of material ionization,

formation of WDP, and its spatiotemporal evolution and physical properties are investigated. Modeling results guide our understanding of the underlining physics of WDPs.

1.2 Objective and goals

The objective of research is to provide greater knowledge and understanding of the transport and absorption of cold X-rays in solar array materials, material melting and vaporization, ionization and plasma formation, spatiotemporal evolution, conductivity and electrical properties of WDP/HDP generated on the surface of solar cells of satellites by X-rays emitted from a high altitude nuclear detonation. The specific goals are

1) implementation of the geometry of solar cells, material composition and properties, flux and energy spectra of incident blackbody X-rays
2) MC modeling of deposited energy and power density distributions along the depth of layered structure of solar cells as a function of blackbody X-ray flux and energy
3) set-up and MD modeling of spatiotemporal evolution and expansion dynamics of WDPs into vacuum
4) HFS calculation of atomic data of WDP atoms and ions such as atomic energy levels, wavefunctions, transition probabilities, ionization potentials, oscillator strengths, photoionization cross-sections, etc.
5) CRSS calculation of populations of atomic levels, ion and electron concentrations for relevant WDP densities and temperatures
6) CRSS calculation of emission and absorption spectra of WDP ions and atoms

7) modeling of radiation transfer, emitted and absorbed power density of photons in the core of WDP, and spectral energy fluxes of X-rays emitted from WDP into space
8) modeling of the electrical conductivity of WDP

1.3 Project duration and tasks

The project was accomplished during March 2018 - June 2023. Due to PI's move on January 1, 2019 from Purdue University to Virginia Commonwealth University (VCU), this project was transferred to VCU on March 6, 2019. No-cost extension for this project was approved by DTRA for the last two years due to the Covid-19 outbreak in Spring 2020 and restrictions on student hiring to work on this project. The work in this project has been broken down into a series of the following tasks

- Modeling of the energy deposition by cold X-rays into solar cell materials
- Modeling of the expansion dynamics of WDP
- Analysis of spatial and temporal evolution of temperature, density, and pressure profiles of WDP and HDP along the depth of material
- Quantum calculations of ionic composition and optical properties of WDP
- Modeling of radiative transfer in WDP
- Modeling of the electrical conductivity of WDP

2. Accomplished work and results

The unique, novel capabilities of an integration of different computational models were employed to perform atomistic simulations of the formation and expansion of warm and hot dense plasmas induced by cold X-rays from a nuclear event. An overview of developed models, performed work, and results is provided below.

2.1 Geometry of solar cells, material composition, and properties

The information on geometry, material composition, structure and components of solar cells was provided by Dr. Phillip Jenkins from Naval Research Laboratory. The schematic of solar cell used in the modeling is illustrated in Fig. 2.

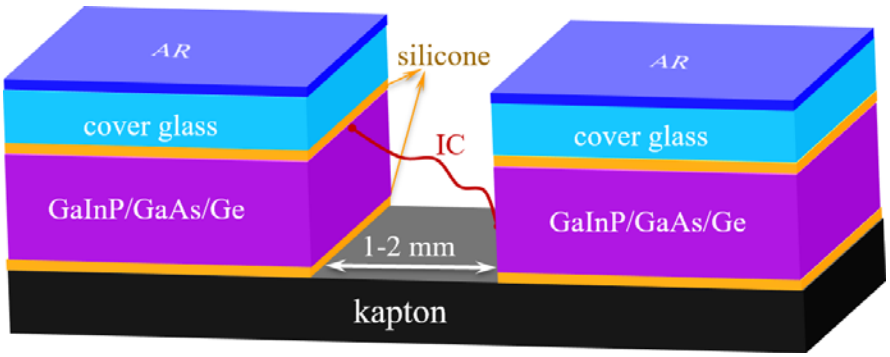

Fig. 2. Thin-film solar cell structure composed of multiple layers of different materials.

The layers of solid materials and their physical properties are as follows

Layer 1: Anti-Reflective (AR) coating, MgF_2, with thickness of 0.12 μm and mass density of 3.148 g/cm^3

Layer 2: 100 μm thick CMX cover glass, a cerium doped borosilicate glass, with mass density of 2.6 g/cm^3 and composition of 63.6 wt% SiO_2; 10.4 wt% B_2O_3; 4.5 wt% ZnO; 2.7 wt% BaO; 7.7 wt% K_2O; 4.7 wt% Al_2O_3; 4.6 wt% CeO_2; and 1.8 wt% U_3O_8

Layer 3: silicone adhesive DC 93-500 with thickness of 12 μm, mass density of 0.965 g/cm^3, and chemical formula $CH_3[Si(CH_3)_2O]_nSi(CH_3)_3$, where *n* is the number of repeating monomer $[SiO(CH_3)_2]$ units

Layer 4: active semiconductor composed of layers of GaInP with thickness of 0.8 μm and mass density of 4.475 g/cm^3, GaAs with thickness of 3.6 μm and mass density of 5.32 g/cm^3, and Ge with thickness of 300 μm and mass density of 5.3234 g/cm^3

Layer 5: silicone adhesive GE-566 with the same parameters as silicone DC 93-500

Layer 6: kapton substrate with thickness of 25 μm, mass density of 1.43 g/cm^3, and chemical formula $(C_{22}H_{10}N_2O_5)_n$, where *n* is the number of repeating monomer units

It is seen that the active semiconductor element GaInP/GaAs/Ge is shielded by layers of AR, CMX, and Silicone. However, there is a gap between the adjacent solar cells with spacing ~1-2 mm. Some designs of solar panels for space applications can have a filling placed in gaps. However, the semiconductor elements are not shielded in many designs and can be directly exposed to X-ray radiation when a solar panel is oriented under some angle relative to the X-ray source. Implications of X-ray irradiation in this case could be quite serious resulting in the coupling of the unshielded GaInP/GaAs/Ge elements in gaps by the dense surface plasmas and to the dielectric structures causing them to be destroyed.

2.2 Energy spectra and flux of incident blackbody X-rays

The energy spectrum of the source of X-ray radiation originating from a nuclear fireball in space is represented by the blackbody Planck's function [2, 21]. Spectral distribution of photon flux emitted from a blackbody in terms of photon frequency v can be written as

$$\frac{dN(v,T)}{dv} = \frac{2\pi v^2}{c^2}\frac{1}{\exp(hv/kT)-1} \quad \left[\frac{1}{cm^2 \cdot s \cdot Hz}\right], \tag{1}$$

where $h = 4.1356677 \times 10^{-18}\ keV \cdot s$ is Planck's constant, $c = 2.99792458 \times 10^{10}\ cm/s$ is speed of light, $k = 1.380649 \times 10^{-23}\ J/K$ is Boltzmann's constant, and T is temperature, $kT\ [keV]$ is thermal energy. This spectral photon flux can be written in terms of photon energy $\varepsilon = hv$ as

$$\frac{dN(\varepsilon,T)}{d\varepsilon} = \frac{2\pi \varepsilon^2}{c^2h^3}\frac{1}{\exp(\varepsilon/kT)-1} \quad \left[\frac{1}{cm^2 \cdot s \cdot keV}\right]. \tag{2}$$

The spectral energy as a function of photon energy is shown in Fig. 3 for three thermal energies of fireball: 0.1 keV, 1 keV, and 10 keV. The photon flux, i.e. number of photons emitted per second per unit surface area of a blackbody, can be evaluated by numerical integration taken over the corresponding spectral energy intervals

$$N(\Delta\varepsilon_i, T) = \frac{2\pi}{c^2 h^3} \int_{\varepsilon_i}^{\varepsilon_{i+1}} \frac{\varepsilon^2}{exp(\varepsilon/kT) - 1} d\varepsilon \quad \left[\frac{1}{cm^2 \cdot s}\right]. \tag{3}$$

The numerical integration was performed using an accurate method of Gaussian quadratures. The photon flux as a function of photon energy was stored in arrays and used to sample the energy of X-rays incident on the surface of solar cells.

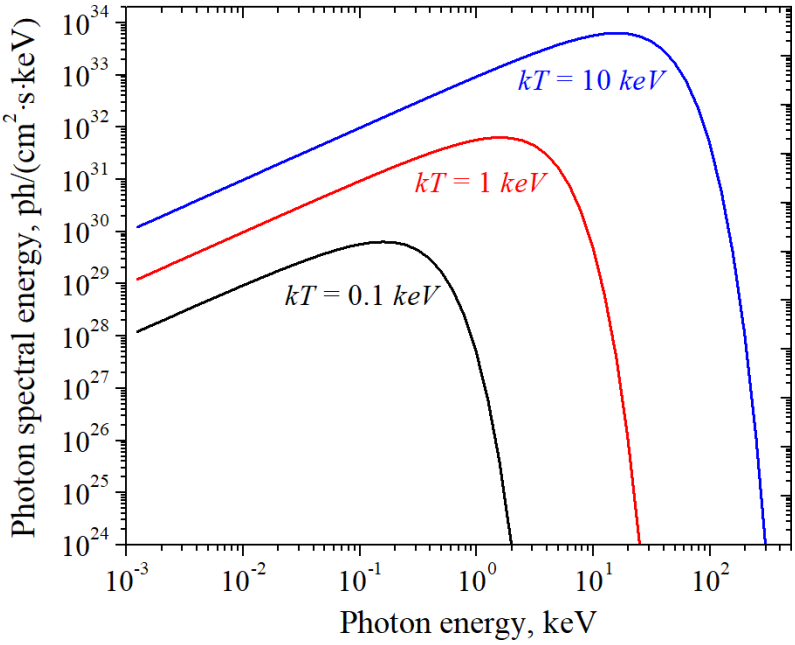

Fig. 3. X-ray spectral energy as a function of photon energy for blackbody thermal energy of 0.1, 1, and 10 keV.

The energy distribution of X-ray flux is shown in Fig. 4 for three values of thermal energy of a fireball. It is seen that the flux of X-rays is extremely high. For example, for $kT = 1\ keV$ corresponding to $T \sim 12 \times 10^6\ K$, the total flux summed over the energy intervals is about 2.4 ×

$10^{32}\ ph/(cm^2 \cdot s)$. This numerical X-ray flux value can be compared to the total photon flux evaluated from an analytic formula

$$F_{ph} = \frac{4\pi\zeta(3)}{c^2 h^3} k^3 T^3 \approx 2.38 \times 10^{32} \left[\frac{ph}{cm^2 \cdot s}\right], \tag{4}$$

where $\zeta(3) \approx 1.2$ is known as Apéry's constant. A very good agreement confirms the validity of X-ray flux integration. Blackbody spectra of X-ray flux shown in Fig. 4 are used in the MC simulation to sample the energy of an incident X-ray.

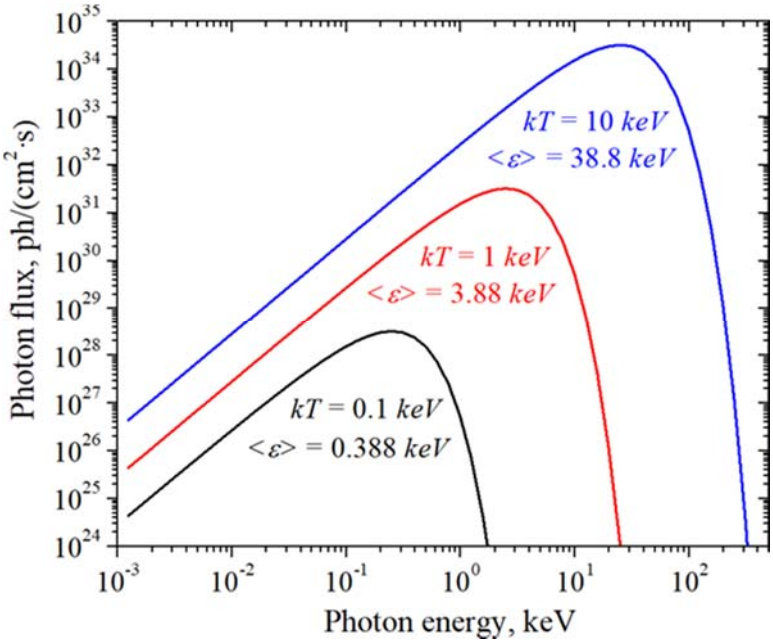

Fig. 4. X-ray flux as a function of photon energy for blackbody thermal energy of 0.1, 1, and 10 keV.

Fortunately, the X-ray flux decreases as the inverse square of the distance from a point where a weapon was detonated at high altitude. Assuming the radius R_0 of a spherical blackbody fireball

with temperature T shown in Fig. 5, the rate (photons per second) of photon emission in the energy interval $\Delta\varepsilon_i$ from the surface area ($2\pi R_0^2$) of the hemisphere is

$$N_0(\Delta\varepsilon_i, T) = 2\pi R_0^2 N(\Delta\varepsilon_i, T) \left[\frac{photons}{s}\right]. \quad (5)$$

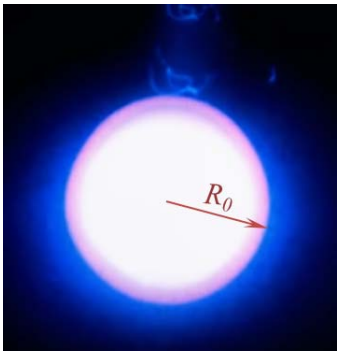

Fig. 5. Nuclear fireball with radius R_0.

The flux of photons at distance d is then

$$N(\Delta\varepsilon_i, T, d) = \frac{N_0(\Delta\varepsilon_i, T)}{2\pi d^2} = \frac{2\pi R_0^2 N(\Delta\varepsilon_i, T)}{2\pi d^2} = \frac{R_0^2}{d^2} N(\Delta\varepsilon_i, T) \left[\frac{photons}{cm^2 \cdot s}\right] \quad (6)$$

For $R_0 = 1\ m$ and $d = 100\ km$, a geometric factor of X-ray flux reduction is $R_0^2/d^2 = 10^{-10}$. This geometric factor of X-ray flux reduction was implemented in the MC modeling of the energy deposition into the layers of solar cells and Ge material.

2.3 Power density distributions along the depth of layered structure of solar cells

Photons with the energy in keV range penetrating into a material are either absorbed (photoabsorption) or scattered (Compton scattering) by the atomic electrons. The transport of photons is characterized by relatively infrequent isolated collisions with a relatively large free path between them. The basic interaction of X-rays with the energy of interest (~1 keV) is photoabsorption [20]. X-ray interacts with an atomic electron resulting in its ejection from an atomic shell. The created vacancy is then filled by one of outer-shell electrons. The process of photoabsorption is completed by the emission of other photon or ejection of Auger-electron. The maximum cross sections of photoabsorption occur near the photoionization thresholds. The HFS model was used to calculate the cross sections of photoabsorption for each atomic shell of elements and tabulated data were used. The distribution of energy deposited by X-rays in layered materials of solar cells was evaluated using the MC model. The MC method makes it possible to simulate random trajectories of X-rays as real ones using the cross sections of interaction processes.

GEANT4 is an open source C++ toolkit for 3D MC modeling of the transport of radiation in materials [22, 23]. It can treat a variety of different particles within a wide range of energies providing several physics models for describing interactions between particles and target atoms. The electromagnetic interactions of electrons and photons are tracked down to zero residual range (energy). The tracking of charged particles in GEANT4 to zero energies enables accurate prediction of their transport and deposited energy distributions. Production thresholds for secondary particles expressed in terms of range cutoffs r_c allow to control the number of secondary particle generations, thus leading to more accurate analysis using small values of r_c. The low energy Livermore model [24] is used to describe the electromagnetic physics processes for photons

and electrons such as the photo-electric effect, Compton scattering, Rayleigh scattering, gamma conversion, bremsstrahlung, impact ionization, fluorescence and Auger-electron emission.

The Modeling Ionizing Radiation Deep Insulator Charging (MIRDIC) code based on GEANT4 libraries was developed in C++. The MC model was implemented in the MIRDIC-GEANT4 code including all possible interactions of photons and secondary particles with materials. The main stages are as follows: (1) The set-up of geometry and selection of materials, primary incident particles, and physics models for interaction processes is implemented in mirdicDetectorConstruction() and mirdicPrimaryGeneratorAction() functions; (2) The C++ function mirdicRunAction() sets the MC run, creates histogram bins for deposited energy distribution along the depth of material, post-processes, and writes data in files. Histograms with equal, grading, and logarithmic bin spacing are implemented; (3) The collection of information on a particle's energy at the end of each MC step and its binning into histograms is accomplished by mirdicSteppingAction() function; (4) The C++ function mirdicTrackingAction () identifies the end of photons and electron's trajectories and bins the deposited energy into histograms. This code was originally developed in collaboration with the NASA's Marshal Space Flight Center for computational studies of the impact of Jovian electrons and photons on a multi-layer configuration of the solid rocket motor (Europa Lander project) [25] and adapted for this research.

The MIRDIC-GEANT4 code was validated against the available computational and experimental data. The profile of energy deposition by 1 MeV electrons into Be-Au-Be slabs calculated using MIRDIC-GEANT4 is compared in Fig. 6 to those computed using the MONSOL code [26] and experimental data (calorimetric measurements performed at Sandia Laboratories) [27]. The comparison of MIRDIC-GEANT4 and experimental results is shown in Fig. 7 for 1 MeV electrons incident on C-Ta-C slabs.

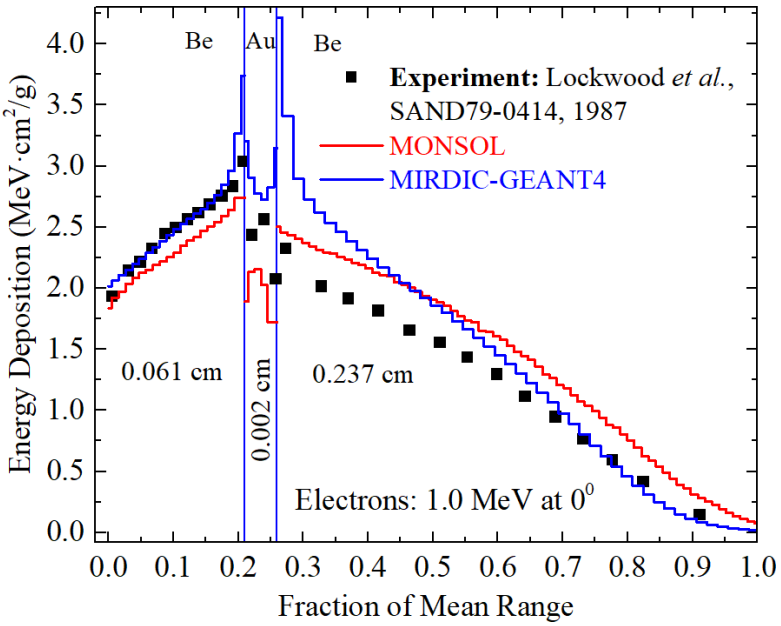

Fig. 6. Comparison of the energy deposition profiles produced by the monoenergetic electrons with 1 MeV at normal incidence onto the Be-Au-Be slabs.

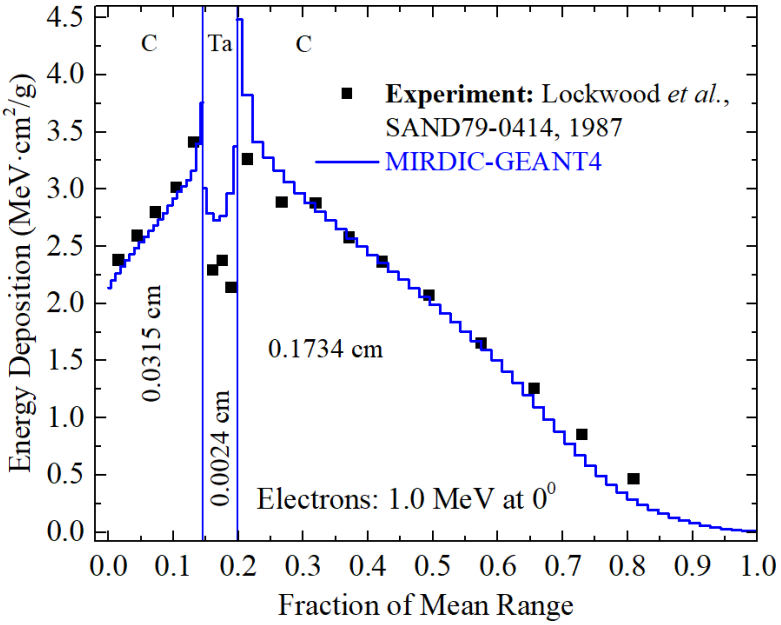

Fig. 7. Comparison of the energy deposition profiles produced by the monoenergetic electrons with 1 MeV at normal incidence onto the C-Ta-C slabs.

The monoenergetic electrons are assumed to impinge normally on the slab targets. The computed and experimental profiles are presented in scaled quantities of the mean range of electrons in slabs. The measured and simulated energy deposition profiles are close to each other within the uncertainties of calorimetric measurements and statistical errors of the MC method. The shapes of profiles rise to the broad peaks for 3-slab targets and then gradually drop to zero values. The discontinuity in both calculated and experimental energy deposition profiles is observed at the interfaces of slabs (Figs. 6 and 7) due to discrete changes in stopping power between slab materials. It is important to note that in this case, as shown in Fig. 6 and 7, the absorbed dose is higher in the slabs with lower mass density (Be and C), even though the total volumetric energy deposition (not shown) is much greater in the high density slabs (Au and Ta). This is explained by the fact that deposited energy is a measurement of energy per unit mass. The electronic stopping power is also defined per unit mass, and is lower for these higher density materials. Therefore, in this instance, it is the lighter materials that yield a higher deposited energy.

The X-ray transport in multi-slab materials of solar arrays (Fig. 8), generation of secondary photons and electrons, and their energy deposition was then investigated using the MIRDIC-GEANT4 code.

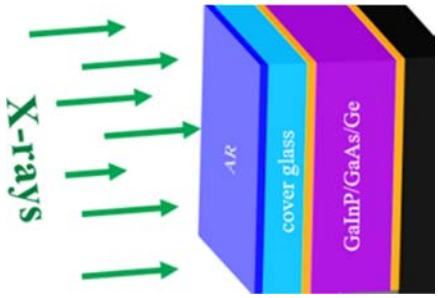

Fig. 8. X-ray flux incident on multiple layers of solar cell.

The distribution of power density generated by blackbody X-rays with the thermal energy of 0.1 keV, 1 keV, and 10 keV along the depth of multi-slab system is shown in Fig. 9.

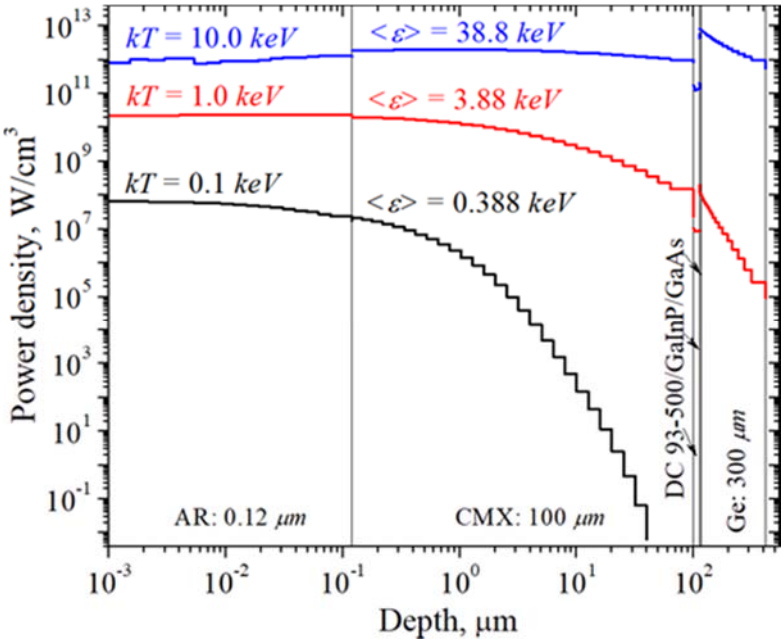

Fig. 9. The power density produced by blackbody X-rays along the depth of multi-layer system of solar cells.

The X-rays are assumed to incident normally on the surface of solar panels. It can be seen that power density increases by orders of magnitude with increasing the temperature of fireball or the energy of X-rays. The power density is deposited into the active semiconductor by blackbody X-rays originating from a fireball with the thermal energy about 1 keV or higher. It should be noted that the monoenergetic X-rays with the energy corresponding to the thermal energy of a fireball and total (integrated over Planck's spectrum) X-ray flux can be used for quick estimate of the power density (see Fig. 10). However, the depth of power density deposition is underestimated for the monoenergetic X-rays.

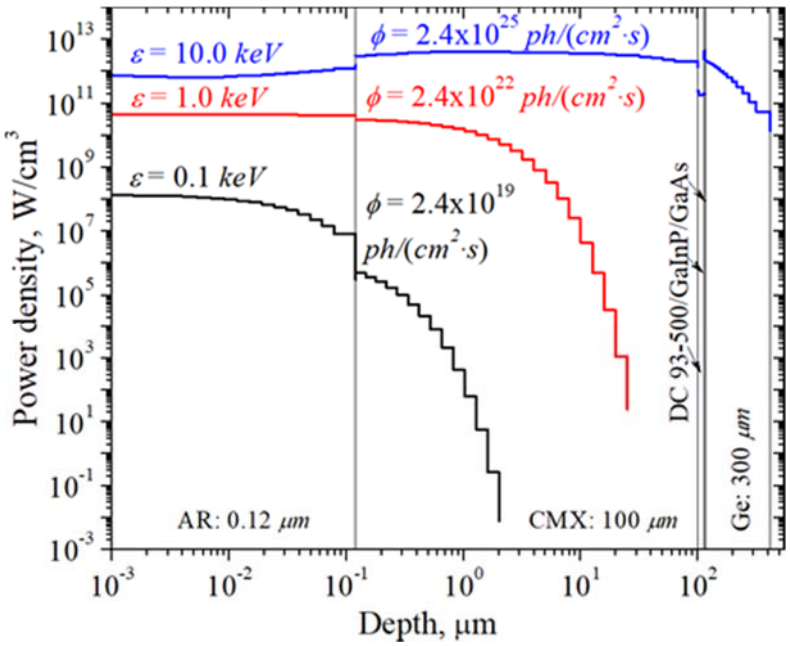

Fig. 10. The power density produced by monoenergetic X-rays along the depth of multi-layer system of solar cells.

The profiles of power density produced by blackbody and monoenergetic X-rays along the depth of a single Ge slab (Fig. 11) are also calculated and shown in Figs. 12 and 13.

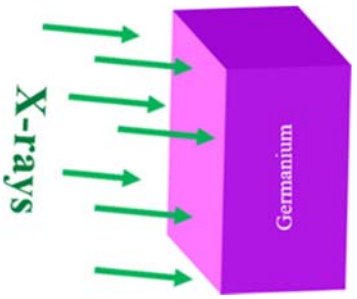

Fig. 11. X-ray flux incident on a layer of Ge.

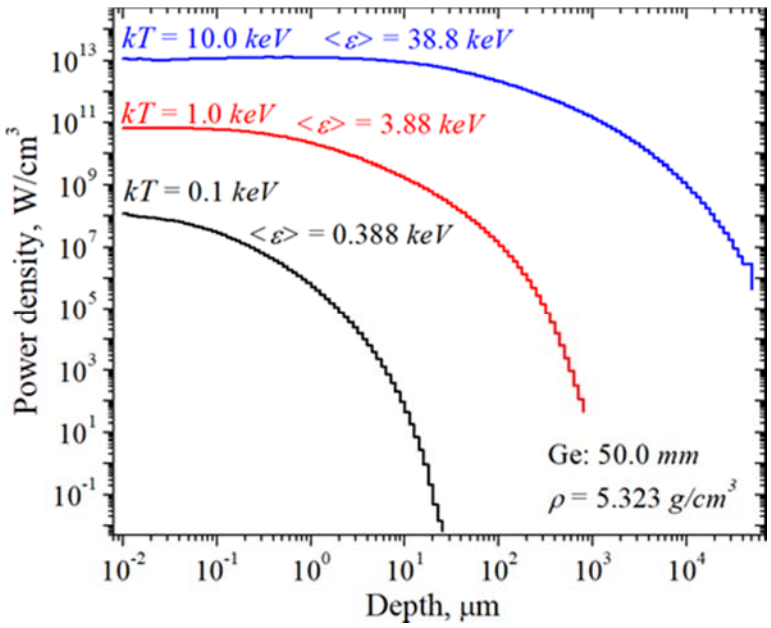

Fig. 12. The power density profiles produced by blackbody X-rays along the depth of a Ge slab of solar cells.

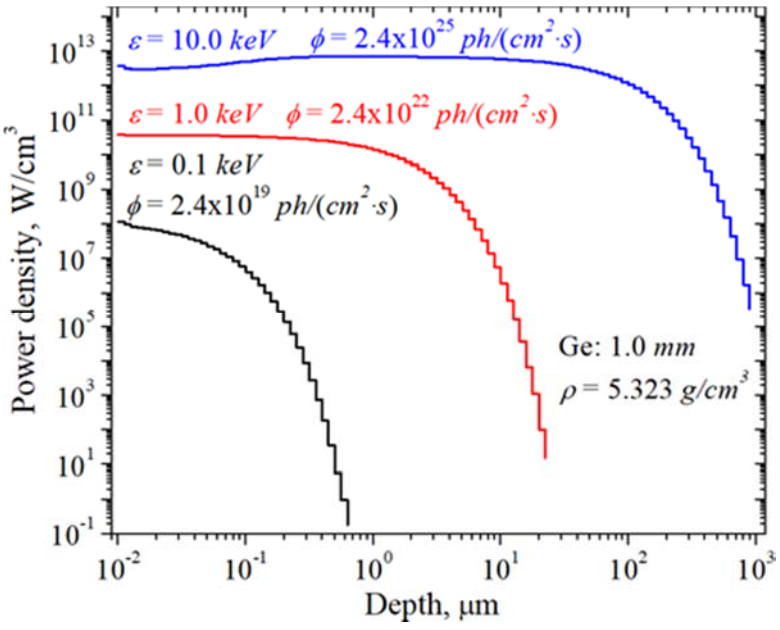

Fig. 13. The power density profiles produced by monoenergetic X-rays along the depth of a Ge slab of solar cells.

The irradiation conditions were the same as in the case of multi-slab system accept the incidence angle of X-rays that was 80^0 with the surface of Ge slab. It is seen that the power density increases by 5 orders of magnitude with increasing the blackbody temperature (energy) of X-rays from 0.1 keV to 10.0 keV. The range of power density deposition is about 50 times higher for X-rays with Planck's blackbody spectrum compared to that by monoenergetic X-rays.

2.4 MD modeling of spatiotemporal evolution of warm and hot dense plasmas

The MD method predicts how every atom in the system moves over time based on the physics model governing the interactions between atoms [28]. The classical MD method treats every atom as a discrete entity. The position $\mathbf{x}_k$ and velocity $\mathbf{v}_k$ of each $k\text{-}th$ atom of mass m_k is changed due the force $\mathbf{F}_k$ produced by all of the other atoms at the location of $k\text{-}th$ atom under consideration [29]

$$m_k \frac{d\mathbf{v}_k}{dt} = \mathbf{F}_k, \tag{7}$$

$$\frac{d\mathbf{x}_k}{dt} = \mathbf{v}_k. \tag{8}$$

The force $\mathbf{F}_k$ on $k\text{-}th$ atom can be calculated using a model for the pairwise interaction potential

$$\mathbf{F}_k = -\sum_{\substack{j=1 \\ j\neq k}}^{N} \frac{\partial U(\mathbf{r}_{kj})}{\partial \mathbf{r}_{kj}}, \tag{9}$$

where $U(\mathbf{r}_{kj})$ and $\mathbf{r}_{kj} = |\mathbf{r}_k - \mathbf{r}_j|$ are the potential and separation distance between atoms k and j, and N is the total number of atoms. These Newton's laws of motion are used to describe the evolution of N atoms in space and time by calculating the forces on atoms and then updating their position and velocity. The MD accuracy is affected by the accuracy of the interatomic potentials and the numerical algorithms used for finite difference approximation of Newton's equations. Very short time steps on the order of a few femtoseconds are used in an MD simulation to ensure numerical stability. A typical MD simulation can involve millions to billions of time steps. This causes the MD simulations to be computationally very expensive.

The MD modeling of WDP/HDP blow-off was performed using LAMMPS, Large-scale Atomic/Molecular Massively Parallel Simulator, developed and maintained at Sandia National Laboratories [30, 31]. LAMMPS is an open source, classical MD code. It is written in C++ with capability to model atomic, polyatomic, metallic or granular systems using a variety of force fields and boundary conditions. LAMMPS integrates Newton's equations of motion (Eqs. 7 and 8) for collections of discrete atoms interacting via interatomic potentials $U(\mathbf{r}_{kj})$ (Eq. 9) with no explicit electrons taken into account. For computational efficiency, neighbor lists are used in LAMMPS to track neighboring atoms. It is a scalable code able to run on one processor as well as thousands of processors. Spatial decomposition techniques are used to partition the computational domain into 3D sub-domains, which are assigned to the processors.

Accurate potential models for $U(\mathbf{r}_{kj})$ are needed to describe the interactions between atoms. The choice of the interatomic potentials is very important issue. These potentials are the estimates derived from *ab initio* calculations or experiments. The potential functions available in LAMMPS were carefully examined for proper modeling the solar cell system composed from

metals, compounds, oxides, and dielectric materials. The assumption of a two-body interaction is often used in MD simulations. The available pair potentials are Lennard-Jones, Buckingham, Morse, Born-Mayer-Huggins, Yukawa, etc. However, the interactions on the atomic scale are fundamentally multi-body in nature, especially for metals. Therefore, a special attention was payed to many-body potentials such as the embedded atom method (EAM), Finnis/Sinclair EAM, modified EAM (MEAM), embedded ion method (EIM), Stillinger-Weber, Tersoff, etc. The EAM potential [32] combines two-body and multi-body interactions in metals. It improves pair potentials by accounting for the electron density. Each atom is considered embedded in a background electron gas created by neighboring atoms. The embedding function is introduced that is the energy required to insert one atom into the electron gas of a given density. The potential energy of i-th atom is given by

$$U_i = f_\alpha\left(\sum_{i\neq j}\rho_\beta(r_{ij})\right)+\frac{1}{2}\sum_{i\neq j}\phi_{\alpha\beta}(r_{ij}), \tag{10}$$

where f_α is an embedding function that represents the energy required to place atom i of type α into the electron gas, ρ_β is the contribution to the electron charge density from atom j of type β at the location of atom i, r_{ij} is the distance between atoms i and j, and $\phi_{\alpha\beta}$ is a pair-wise potential. The first term in Eq. 10, accounting for the compressibility of the electron gas, expands slightly the volume of solid and gives the correct elastic constants. The pair interaction term is purely repulsive. It can be considered as the geometric mean of the pair interaction for individual species. The energy of an atom in the composite and pure material can be calculated with the same embedding function. For a pure material, three functions must be specified: the embedding

function, a pair-wise interaction, and an electron density function. For a material with two sorts of atoms, the EAM potential involves seven functions: three pair-wise interactions (α-α, α-β, β-β), two embedding functions, one for each type of atom, and two electron density functions. These functions are available in LAMMPS as tables.

The development of many-body potentials for semiconductors is even more challenging. Semiconductor materials may undergo the phase changes that affects an atomic structure and coordination number. The three-body Tersoff potential [33, 34] that includes an angular contribution was developed and parametrized for semiconductor materials and their compounds. It accounts for the effects of angles between bonds on the electron distributions. For example, the interaction energy between i-th and j-th silicon atoms can be represented by the following expression

$$U_{ij} = f_c(r_{ij})\left(Ae^{-\lambda_1 r_{ij}} - B_{ij}e^{-\lambda_2 r_{ij}}\right), \tag{11}$$

where

$$B_{ij} = \left(1 + \beta^n \varsigma_{ij}^n\right)^{-1/2n}, \tag{12}$$

$$\varsigma_{ij} = \sum_{k \neq i,j} f_c(r_{ik})\mathrm{g}(\theta_{ijk})e^{\lambda_2^3 (r_{ij} - r_{ik})^3}, \tag{13}$$

$$\mathrm{g}(\theta) = 1 + c^2/d^2 - c^2/(d^2 + (h - \cos\theta)^2). \tag{14}$$

The angular dependence θ_{ijk} between bonds ij and ik is introduced using the function ς_{ij}. The bond order function B_{ij} represents multibody effects. Function $f_c(r_{ij})$ is a cut-off radius function used to evaluate the cutoff radius for the potential. The parameters A, λ_1, λ_2, β, n, c, d, h used in the above equations can be found in ref. [35].

2.4.1 Momentum scaling model

The electrons are not treated explicitly in the classical MD simulations. Without electrons, it is not possible to model the absorption of laser or X-ray energy and heat exchange between the electrons and lattice atoms. To resolve this problem, the momentum scaling model (MSM) is introduced here to directly account for the heating of the atoms by electrons [36-38]. In the MSM approach the momentum (velocity) of k-th atom $\mathbf{p}_k = m_k \mathbf{v}_k$ is rescaled at every time step Δt by a scaling factor β_k. This results in the increase of temperature of ions T_i in each MD cell. In the MSM-MD, the kinetic energy of *k-th* atom after each time step Δt is determined as [38]

$$K_k(t + \Delta t) = K_k(t) + \Delta t S(z_k, r_k, t)/N_a. \quad (15)$$

The laser or X-ray energy deposition $S(z_k, r_k, t)$ is calculated at the location of each k-th atom. Here $K_k(t)$ and $K_k(t + \Delta t)$ are the kinetic energy of *k-th* atom at times t and $t + \Delta t$. The number density is calculated as

$$N_a = \rho N_A / W, \quad (16)$$

where ρ is the mass density of material, N_A is Avogadro number, and W is the molar weight. The number density N_a can be assumed to be a constant on timescale of pulse duration <1 ps. Thus, the amount of radiation source energy

$$\Delta K_k(t) = \Delta t S(z_k, r_k, t)/N_a \quad (17)$$

that is absorbed by k-*th* atom is calculated as a product of the power density S and time step Δt divided by the atomic number density N_a. This deposited energy is transformed to the kinetic energy

$$\Delta K_k(t) = K_k(t + \Delta t) - K_k(t) \tag{18}$$

of k-*th* atom. This expression can be rewritten as

$$\Delta K_k(t) + K_k(t) = K_k(t + \Delta t) \tag{19}$$

Dividing both sides of this expression by $K_k(t)$ and equating to β_k^2, one can arrive to

$$\Delta K_k(t)/K_k(t) + 1 = K_k(t + \Delta t)/K_k(t) = \beta_k^2. \tag{20}$$

Thus, the scaling factor of each k-*th* atom can be expressed through the radiation energy deposition $\Delta K_k(t)$ as

$$\beta_k = \sqrt{1 + \Delta K_k(t)/K_k(t)}. \tag{21}$$

On the other side, it means that the kinetic energy of k-*th* atom scales as

$$K_k(t + \Delta t) = \beta_k^2 K_k(t), \quad \text{or} \quad p_k^2(t + \Delta t) = \beta_k^2 p_k^2(t). \tag{22}$$

In terms of velocity, this can be expressed as

$$v_k^2(t+\Delta t) = \beta_k^2 v_k^2(t) \tag{23}$$

or

$$v_{k\,x}^2(t+\Delta t) + v_{k\,y}^2(t+\Delta t) + v_{k\,z}^2(t+\Delta t) = \beta_k^2 \left(v_{k\,x}^2(t) + v_{k\,y}^2(t) + v_{k\,z}^2(t)\right). \tag{24}$$

From this expression, it follows that the x, y and z components of velocity of k-th atom at $t+\Delta t$ are obtained by scaling its velocity components at t by a factor β_k as

$$v_{k\,x}(t+\Delta t) = \beta_k v_{k\,x}(t), \tag{25}$$

$$v_{k\,y}(t+\Delta t) = \beta_k v_{k\,y}(t), \tag{26}$$

$$v_{k\,z}(t+\Delta t) = \beta_k v_{k\,z}(t). \tag{27}$$

The components of force on k-*th* atom can be then calculated as

$$\Lambda_{k\,x}(t+\Delta t) = (\beta_k - 1) m_k v_{k\,x}(t)/\Delta t, \tag{28}$$

$$\Lambda_{k\,y}(t+\Delta t) = (\beta_k - 1) m_k v_{k\,y}(t)/\Delta t, \tag{29}$$

$$\Lambda_{k\,z}(t+\Delta t) = (\beta_k - 1) m_k v_{k\,z}(t)/\Delta t. \tag{30}$$

The MD equation (7) is modified to the MSM-MD equation as

$$m_k \frac{d\mathbf{v}_k}{dt} = \mathbf{F}_k + \mathbf{\Lambda}_k, \tag{31}$$

where $\mathbf{\Lambda}_k$ is the force due to radiation source with the force components (equations 28-30) determined from the MSM. The MSM-MD approach allows to model very large systems with tens to hundreds of millions of atoms. The MSM coupled with the MD method was implemented in LAMMPS. The original MSM-LAMMPS code was used for investigating femtosecond laser ablation of aluminum and distribution of nano-clusters in a plasma plume (Fig. 14 shows a snapshot of an atomic system with ~10^7 Al atoms at 4.8 ps) [38].

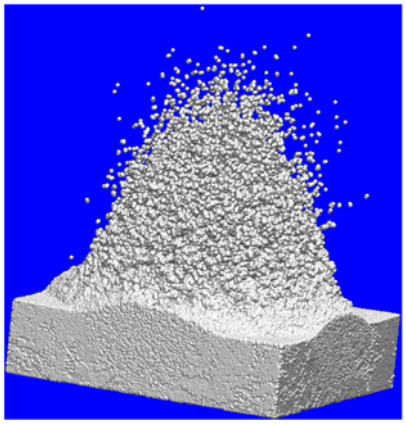

Fig. 14. Snapshot of Al plasma plume with Al atoms and nano-clusters at time moment of 4.8 ps.

2.4.2 MSM-MD modeling of X-ray induced Ge blow-off into vacuum

The MSM-MD model is appropriate for simulations of time-dependent X-ray interactions with materials and well suitable for the study of spatiotemporal evolution of WDP/HDP. The MSM-MD model was updated and utilized for investigating the X-ray induced ablation and blow-off of Ge material into vacuum. This approach involves a direct rescaling of the kinetic energy of Ge atoms by a factor accounting for the X-ray energy deposition on each atom. X-rays are absorbed on the electrons dominantly contributing to the thermal heat conduction. The profiles of absorbed

power density along the depth of Ge layer (Figs. 12 and 13) calculated by MIRDIC-GEANT4 are used in the MSM-MD model as a source term. The time-dependent information on the spatial distribution of density, temperature, and pressure fields of expanding WDP/HDP are derived from the MSM-MD simulations.

The study of X-ray induced blow-off has been proceeded through the following steps: 1) computational domain construction; 2) relaxation and equilibration; 3) computational runs; and 4) post processing of simulation results. On the *first* stage of domain construction, atoms are organized into a crystal structure according to the type of material and its lattice data. The size of domain, atoms locations, and microstructure interfaces between layers of materials are specified. An atomic system with millions of atoms are studied using supercomputers with multi-processors. The schematic of MD box and finite size cells for calculating the bulk properties of the expanding WDP are illustrated in Fig. 15. A small MD box embedded in the bulk Ge material and filled with ~10 million of Ge atoms is considered. The MSM-MD setup of this MD-box is shown in Fig. 16. The size of MD box is $45.264 \times 45.264 \times 2829\ nm^3$. The three-body Tersoff potential function is used to describe the interaction between Ge atoms. The power density distribution along the depth calculated by the MIRDIC-GEANT4 code is used as an input in the MD equations of atom motion (second term in Eq. 31). Due to the severe limitations of MD method on the number of atoms (size of system) and duration of simulation, the power density generated by monoenergetic X-rays with 0.1 keV and 2.4×10^{19} ph/(cm^2·s) (Fig. 13) was employed in MSM-MD simulations. The thickness of Ge layer was 0.11316 μm that is smaller than the depth of energy deposition ~0.6 μm.

The macroscopic physical and thermodynamic quantities such as the potential and kinetic energy, temperature, pressure, etc. are evaluated by taking the time averages over MD configurations. The average potential energy $\langle U \rangle$ can be estimated by averaging its values as

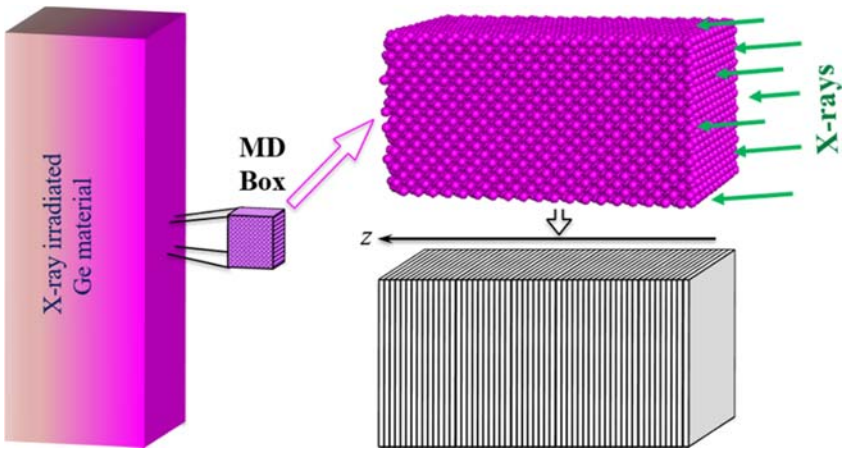

Fig. 15. The bulk Ge material, small MD box filled with Ge atoms, and finite size cells along the depth of a Ge slab irradiated by X-rays.

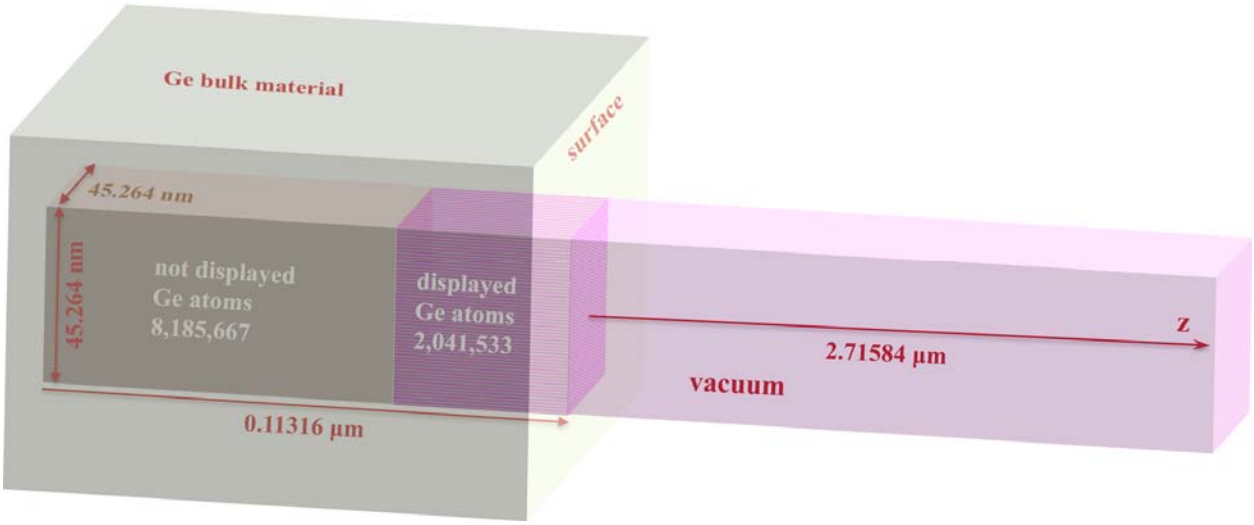

Fig. 16. The set-up of MD box filled with more than 10 million of Ge atoms for studying their blow-off into vacuum under the irradiation by X-rays.

$$\langle U(t)\rangle = \sum_k \sum_{j>k} U\left(\left|\mathbf{r}_k(t) - \mathbf{r}_j(t)\right|\right). \quad (32)$$

The average kinetic energy can be easily evaluated during the MD run as

$$\langle K(t)\rangle = \frac{1}{2}\sum_k m_k[\mathbf{v}_k(t)]^2. \quad (33)$$

The total energy $\langle E(t)\rangle = \langle U(t)\rangle + \langle K(t)\rangle$ is conserved with time, while there is the energy exchange between kinetic and potential parts resulting in their fluctuations. During the MD simulation, however, there are small fluctuations in the total energy caused by errors in the time integration of Newtonian equations of atom motion. An estimate of temperature can be obtained from the average kinetic energy as

$$T = \frac{2\langle K(t)\rangle}{3Nk_B}. \quad (34)$$

The evaluation of pressure in the MD simulation based on the Clausius virial equation can be written as

$$P = \frac{Nk_BT}{V} + \frac{1}{d \cdot V}\langle \sum_{k=1}^{N} \mathbf{r}_k(t) \cdot \mathbf{F}_k(t)\rangle, \quad (35)$$

where d is the dimensionality of the system (2 or 3) and V is the volume. This equation reduces to the equation of state of the ideal gas when the second term is zero (non-interacting atoms). Other

physical and thermodynamic properties such as the mean square displacement of atoms, phase transition from solid to liquid, melting temperature, pair correlation function, static and dynamic structure factors can be also evaluated in the MSM-MD simulation. Finite size cells (Fig. 15) are used for evaluating the averages of temperature, density, and pressure along the depth of a Ge slab. Cells contain ~50,000 - 60,000 Ge atoms.

The *second* step is to relax and equilibrate all the atoms to their lowest energy state. Periodic x- and y-boundaries and non-periodic z-boundaries are considered. The surface atoms may have high potential energy and move during equilibration into new positions with lower energy. The relaxation and equilibrium processes take place at isothermal conditions bringing the system into a specified temperature regime. The number of particles N, volume V of the simulation box, and temperature T (canonical NVT ensemble) were kept constant in the equilibration simulations. To keep constant temperature, the MD system was connected to a thermal bath providing or absorbing the heat, thus maintaining the constant temperature.

In the *third* step, the domain is subjected to applied X-ray irradiation (MIRDIC-GEANT4 code) and the MSM-MD modeling is performed. The modeling of expansion of produced WDP/HDP is then accomplished. The computational runs can be repeated for various irradiation conditions. Each MSM-MD simulation can be started from the same equilibrated domain configuration.

In the *fourth* step, the simulation results are post processed. During the MSM-MD simulation, the location of all atoms, their velocities, forces are written into files. This information is collected at a certain number of time steps as snapshots. RasMol visualization software package [39] was used to read this information, render atom locations into images, and examine the motion and behavior of the atoms during the MSM-MD simulation.

2.5 Analysis of spatiotemporal evolution of temperature, density, and pressure profiles of WDP/HDP along the depth of Ge material

The outcomes of the MSM-MD simulations are 1) 3D snapshots of atomic positions; and 2) distributions of density, temperature, and pressure along the depth of Ge material at specific times. The focus is on the understanding of the WDP phase formation, spatiotemporal evolution, and transition from the absorption of X-rays in a bulk solid to development of WDP/HDP that shields a solid material. The 3D snapshots in Fig. 17 illustrate the initiation, formation, and expansion of WDP phase near the surface of Ge material at very early times.

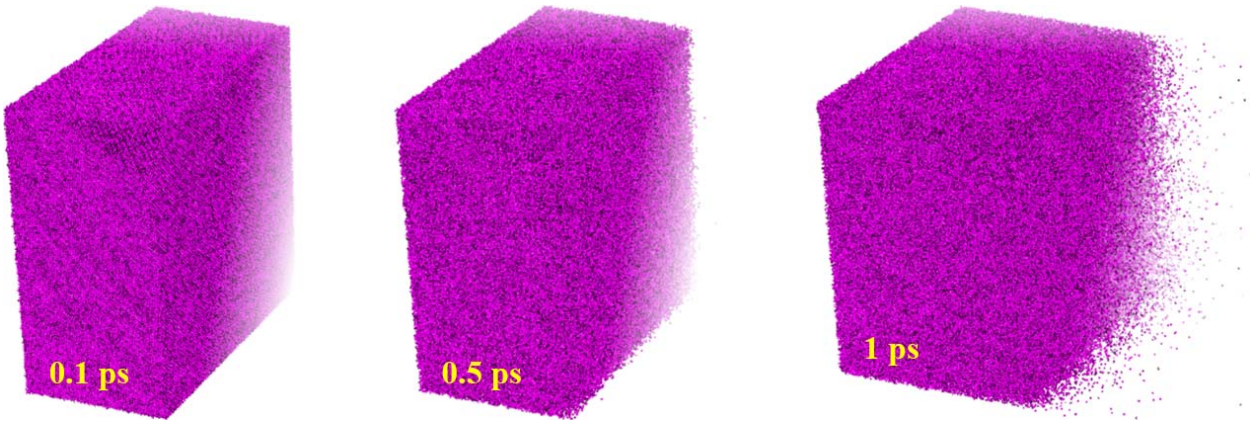

Fig. 17. Snapshots of Ge WDP near the surface for early times.

The MD box contains more than 10 million of discrete Ge atoms (Fig. 16) and only about 2 million of atoms are illustrated in snapshots (Fig. 17) below the surface. RasMol visualization software has failed to display all 10 million atoms. At 0.1 ps, the right-hand side (front face) of the box

corresponds approximately to the surface of unshielded active Ge element of solar cell. During this short time the Ge atoms didn't change significantly their crystallographic positions. This is because the energy transfer between the hot electrons and cold ions is still insignificant during this short time interval. At 0.5 ps, the surface is slightly expanded and becomes rougher. This means that melting and disintegration of Ge material occurs at this time. The individual Ge atoms can be now observed near the surface. At 1 ps, the WDP is formed on the surface shielding the bulk of Ge material. The expansion of WDP phase and blow-off into vacuum begins. A large number of individual atoms and small atomic clusters are created in the front of expanding WDP. The 3D snapshots of WDP expansion into vacuum are shown in Fig. 18 for later time moments from 2 ps to 10 ps. WDP expands ~1.8 μm during ~10 ps.

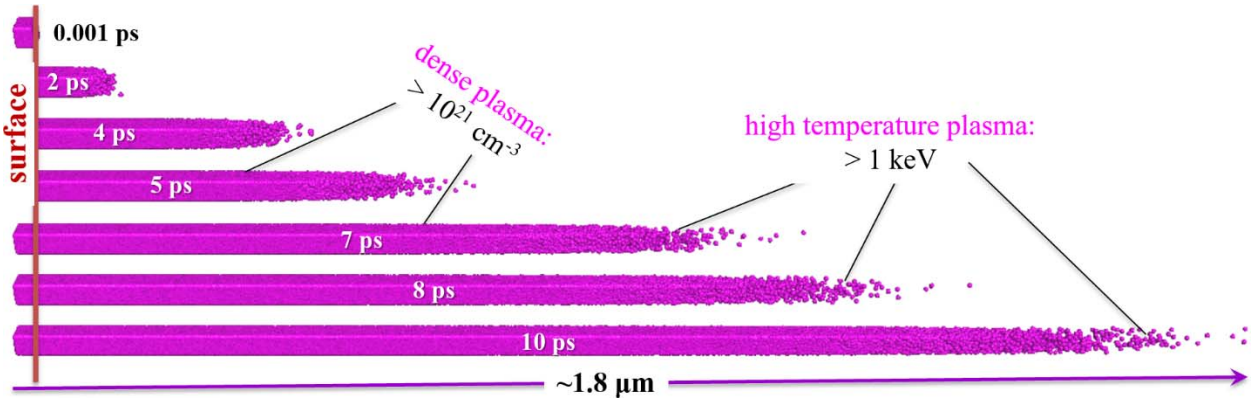

Fig. 18. 3D snapshots of X-ray induced WDP and HDP blow-off into vacuum.

The time evolution of density and temperature along Z-depth of the Ge sample after irradiation with X-rays is illustrated in Figs. 19 and 20, respectively. The original position of the surface corresponds to zero. The Ge material is located below and vacuum is above zero.

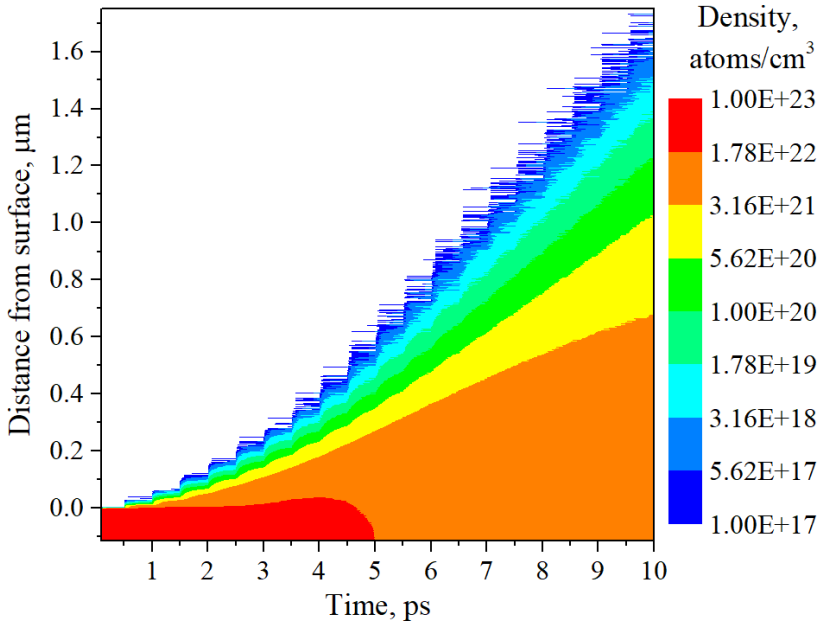

Fig. 19. Density color maps of WDP and HDP formed below and above the surface of a Ge slab during 10 ps.

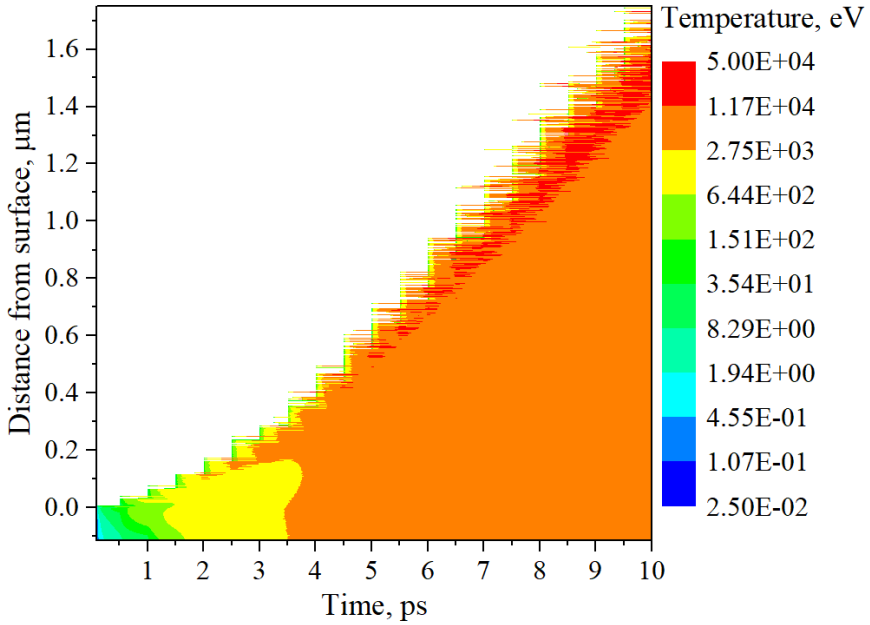

Fig. 20. Temperature color maps of WDP and HDP formed below and above the surface of a Ge slab during 10 ps.

Temperature of Ge sample below the surface increases to tens of eV (still <100 eV) during ~0.5 ps, but density remains near solid density (~10^{23} atoms/cm^3) during this time. This state of Ge material corresponds to the WDP state. After that the temperature rises to several keV during 5 ps (Fig. 20) with density still corresponding to the solid state density of Ge material (Fig. 19). This is the state of material that corresponds to the Hot Dense Plasma (HDP) state with near-solid density (~10^{23} atoms/cm^3) and temperatures >>100 eV. It means that the irradiated solid region is melted, evaporated near the surface, and expanded into vacuum (Fig. 18). It is seen in Figs. 19 and 20 that after $\gtrsim$ 1 – 1.5 ps the expanding plasma contains the HDP below and above the surface of material. Therefore, the WDP state is short lived below the surface of Ge material during ~1 ps - 1.5 ps, and then the HDP states occur below and above the original surface in the expanding plasma. After ~5 ps the dense plasma $\gtrsim 10^{21}$ atoms/cm^3 exists below and above the surface (Fig. 19). The temperature of plasma increases more than 2 keV above and below the surface (Fig. 20).

The analysis of the stress created in the bulk can shed light on the phase change in the Ge material due to the absorption of X-rays. The color map of stress is shown in Fig. 21. The stress is illustrated along the depth of Ge layer for different times. Green color in the map means unstressed state. The stress could be positive or negative corresponding to compression or expansion (distress) in Ge material. The analysis of stress data in files revealed that the negative stress occurs locally at some tiny points only during the time interval less than 1 ps. This corresponds to the initial stage of relaxation of the solid-state material after the absorption of X-rays. Therefore, the locations of negative stress are not visible in Fig. 21. At later times the stress is only positive corresponding to the expanding WDP/HDP under high pressure. It is seen that the value of stress is highest, ~168

Mbar, from ~2 ps to ~4 ps inside the solid material. From ~4 ps to ~6.5 ps, the stress drops to ~94 Mbar in the formed HDP. The value of stress is ~45 Mbar after 6.5 ps in the expanding HDP.

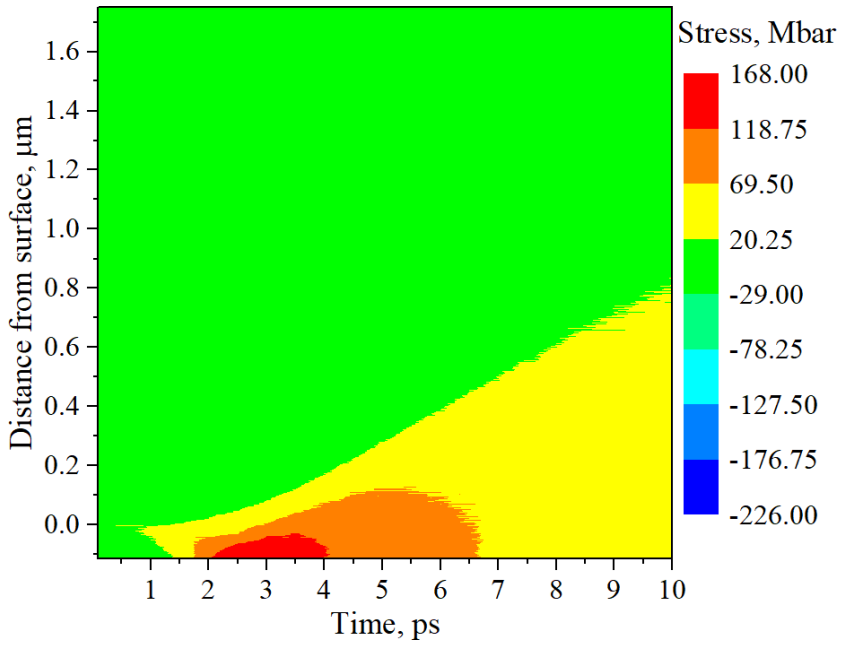

Fig. 21. Color map of stress induced by the absorption of X-rays in Ge layer.

2.6 Calculation of atomic data, electron and ion plasma composition, and optical properties of WDPs and HDPs

2.6.1 HFS atomic data of atoms and ions

The structure of atomic energy levels, wavefunctions, transition probabilities, ionization potentials, oscillator strengths, photoionization cross-sections have been calculated using the Radiative Emissivity and Opacity of Dense Plasmas (REODP) computer code [15] that implements the quantum-level HFS model [15, 40, 41]. The dynamic and static electron

correlations missing in the HFS theory were included using the Multi-Configuration and Configuration-Interaction methods [42, 43]. The HFS model follows an approach within the central symmetry approximation, i.e. an N-electron atom is considered as spherically symmetrical quantum system. The nucleus is treated as a point charge with infinite mass (Born-Oppenheimer approximation). The wavefunction of a N-electron atom can be represented as the product of radial and angular wavefunctions $\Psi(\vec{r}_1,\vec{r}_2,\ldots,\vec{r}_n) = R(r_1,r_2,\ldots,r_N)\times Y(\theta_1\varphi_1,\theta_2\varphi_2,\ldots,\theta_N\varphi_N)$. The angular wave-functions are usual spherical harmonics that can be found separately. The HFS method approximately solves the radial Schrödinger equation. Let us consider a configuration of the nl-shell given by its principal quantum number n and orbital quantum number l with q_{nl} equivalent electrons. The HFS energy levels are calculated for the whole configurations, i.e. one atomic level corresponds to each pair of nl quantum numbers, neglecting the spin-orbit splitting. The Schrödinger equation for radial wave function $R_{nl}(r)$ in approximation of nl-configurations can be written as follows

$$\left(\frac{d^2}{dr^2}+\frac{2Z(r)}{r}+V_{ex}(r)-\frac{l(l+1)}{r^2}+\varepsilon_{nl}\right)R_{nl}(r)=0\,, \tag{36}$$

where

$$\frac{Z(r)}{r}=\int_r^\infty\frac{1}{r_*^2}\left(Z_0-\int_0^{r_1}\rho(x)dx\right)dr_*\,,\qquad V_{ex}(r)=-\frac{3}{2}\left(\frac{3}{\pi}\rho(r)\right)^{1/3},\qquad \rho(r)=\sum_{nl}q_{nl}R_{nl}^2(r)\,. \tag{37}$$

Here r is the distance from the nucleus, r_* is the integration variable, ε_{nl} is the binding energy of electron, Z_0 is the nucleus charge, $Z(r)$ is the effective charge of the ion field, $V_{ex}(r)$ is the

potential of exchange interaction, $\rho(r)$ is the electronic density inside the atom. The exchange term provides a lowering of the overall energy due to spin correlation keeping like-spin electrons being apart. The integral in the expression for $Z(r)/r$ takes into account the inner screening of the nucleus by outer electrons.

Equation (36) involves the electrostatic and exchange atomic potentials, which are also the subject for determination. They are expressed through the wave functions of other atomic electrons. Equation (36) with additional conditions (37) presents the HFS system. The statistical approximation of the $\rho^{1/3}$ type suggested by Slater is used for the exchange potential $V_{ex}(r)$ in the HFS method. As the system (36-37) is of an implicit type, it is solved self-consistently by means of the iterative methods. As 0-th approximation, a hydrogen-like wavefunction R_{nl}^0 is used. Once the eigenvalues ε_{nl} and eigen-wavefunctions $R_{nl}(r)$ are determined from Eq. (36), the charge distribution in the atom and the exchange potential are calculated from Eq. (37). Equation (36) is solved again giving new wavefunctions. The solution is considered to be converged when the eigenvalues are accurate as $\left|\varepsilon_{nl}^i - \varepsilon_{nl}^{i-1}\right| \Big/ \varepsilon_{nl}^i \le \delta$ with δ chosen small enough. The wavefunction $R_{nl}(r)$ is calculated for each pair of the nl-quantum numbers. The eigenvalue ε_{nl} is simultaneously determined.

The perturbation theory of the non-relativistic HFS wavefunctions is used to account for the relativistic effects thus significantly improving the atomic data. The energy level shifts due to the velocity dependence of electron mass and spin-orbit interactions are corrected within the limits of perturbation method as described in [44]. The radial HFS wavefunctions are used to calculate the Slater integrals that define the direct and exchange electronic interactions between different atomic shells. The angular functions of the equivalent electrons within a shell as well as those of

different shells are expressed through the matrix elements. For light elements ($Z < 30$) the *LS*-coupling scheme is used to represent the energy states and spectral transitions of ions and atoms. In this *LS*-coupling approximation, the electrostatic interaction between electrons has a much greater value than the spin-orbit interaction. The well justified, adequately developed HFS model is used for calculating the atomic data such as energies of atomic levels, ionization potentials, oscillator strengths, transition probabilities, and photoionization cross-sections.

The calculated atomic data are illustrated for Ge with Z = 32 [45]. The electronic configuration of Ge is $1s^2 2s^2 2p^6 3s^2 3p^6 3d^{10} 4s^2 4p^2$. The ionization potential for each atomic electron in Ge is given in Table 1 starting with outermost electrons and going to the inner electrons. It is seen that the energy required to ionize the electrons increases reaching about ~13-14 keV for the K-shell electrons.

Table 1. The ionization potentials of Ge atoms and ions.

# of e^-	**I [eV]**	**# of e^-**	**I [eV]**	**# of e^-**	**I [eV]**	**# of e^-**	**I [eV]**
1	7.880000	9	214.1346	17	616.9337	25	2452.075
2	15.93000	10	249.5517	18	659.2881	26	2582.238
3	34.21000	11	286.6669	19	702.2554	27	2713.932
4	45.71000	12	325.4206	20	745.7837	28	2846.616
5	93.50000	13	365.7580	21	839.2684	29	3069.507
6	118.8686	14	407.6249	22	885.3021	30	3199.132
7	148.6983	15	534.2858	23	2197.544	31	13567.19
8	180.4910	16	575.2468	24	2323.767	32	14114.09

The energy of atomic levels for the neutral (z = 0) Ge atom, singly-ionized (z = 1) and doubly-ionized (z = 2) Ge ions are listed below in Table 2. The energy values are provided for both bounded (negative values) and unbounded (positive values) states. The energy of levels for other Ge ions up to z = 31 have been also calculated and used in the modeling.

Table 2. The energy of atomic levels for neutral Ge atom, singly-ionized and doubly-ionized Ge ions.

Ion Charge: z = 0	**Ion Charge: z = 1**	**Ion Charge: z = 2**
n = 1 l = 0 E = -0.110772E+05 eV	n = 1 l = 0 E = -0.110790E+05 eV	n = 1 l = 0 E = -0.110722E+05 eV
n = 2 l = 0 E = -0.140213E+04 eV	n = 2 l = 0 E = -0.140385E+04 eV	n = 2 l = 0 E = -0.139681E+04 eV
n = 2 l = 1 E = -0.124129E+04 eV	n = 2 l = 1 E = -0.124303E+04 eV	n = 2 l = 1 E = -0.123601E+04 eV
n = 3 l = 0 E = -0.174451E+03 eV	n = 3 l = 0 E = -0.176154E+03 eV	n = 3 l = 0 E = -0.169060E+03 eV
n = 3 l = 1 E = -0.122568E+03 eV	n = 3 l = 1 E = -0.124268E+03 eV	n = 3 l = 1 E = -0.117166E+03 eV
n = 3 l = 2 E = -0.335689E+02 eV	n = 3 l = 2 E = -0.352342E+02 eV	n = 3 l = 2 E = -0.280682E+02 eV
n = 4 l = 0 E = -0.866506E+01 eV	n = 4 l = 0 E = -0.929844E+01 eV	n = 4 l = 0 E = 0.000000E+00 eV
n = 4 l = 1 E = 0.000000E+00 eV	n = 4 l = 1 E = 0.000000E+00 eV	n = 4 l = 1 E = 0.100188E+02 eV
n = 4 l = 2 E = 0.634011E+01 eV	n = 4 l = 2 E = 0.973944E+01 eV	n = 4 l = 2 E = 0.210286E+02 eV
n = 4 l = 3 E = 0.702987E+01 eV	n = 4 l = 3 E = 0.125241E+02 eV	n = 4 l = 3 E = 0.265327E+02 eV
n = 5 l = 0 E = 0.491605E+01 eV	n = 5 l = 0 E = 0.797901E+01 eV	n = 5 l = 0 E = 0.201264E+02 eV
n = 5 l = 1 E = 0.587746E+01 eV	n = 5 l = 1 E = 0.988871E+01 eV	n = 5 l = 1 E = 0.228817E+02 eV
n = 5 l = 2 E = 0.701303E+01 eV	n = 5 l = 2 E = 0.124531E+02 eV	n = 5 l = 2 E = 0.267624E+02 eV
n = 5 l = 3 E = 0.733589E+01 eV	n = 5 l = 3 E = 0.137491E+02 eV	n = 5 l = 3 E = 0.292914E+02 eV
n = 6 l = 0 E = 0.651839E+01 eV	n = 6 l = 0 E = 0.118091E+02 eV	n = 6 l = 0 E = 0.264073E+02 eV
n = 6 l = 1 E = 0.684756E+01 eV	n = 6 l = 1 E = 0.125628E+02 eV	n = 6 l = 1 E = 0.275901E+02 eV
n = 6 l = 2 E = 0.732616E+01 eV	n = 6 l = 2 E = 0.137118E+02 eV	n = 6 l = 2 E = 0.294229E+02 eV
n = 6 l = 3 E = 0.750214E+01 eV	n = 6 l = 3 E = 0.144154E+02 eV	n = 6 l = 3 E = 0.307940E+02 eV
n = 7 l = 0 E = 0.709663E+01 eV	n = 7 l = 0 E = 0.134033E+02 eV	n = 7 l = 0 E = 0.292469E+02 eV
n = 7 l = 1 E = 0.724785E+01 eV	n = 7 l = 1 E = 0.137776E+02 eV	n = 7 l = 1 E = 0.298625E+02 eV
n = 7 l = 2 E = 0.749617E+01 eV	n = 7 l = 2 E = 0.143937E+02 eV	n = 7 l = 2 E = 0.308747E+02 eV
n = 7 l = 3 E = 0.760239E+01 eV	n = 7 l = 3 E = 0.148173E+02 eV	n = 7 l = 3 E = 0.317007E+02 eV
n = 8 l = 0 E = 0.737109E+01 eV	n = 8 l = 0 E = 0.142219E+02 eV	n = 8 l = 0 E = 0.307745E+02 eV
n = 8 l = 1 E = 0.745286E+01 eV	n = 8 l = 1 E = 0.144347E+02 eV	n = 8 l = 1 E = 0.311353E+02 eV
n = 8 l = 2 E = 0.759850E+01 eV	n = 8 l = 2 E = 0.148036E+02 eV	n = 8 l = 2 E = 0.317534E+02 eV
n = 8 l = 3 E = 0.766746E+01 eV	n = 8 l = 3 E = 0.150782E+02 eV	n = 8 l = 3 E = 0.322894E+02 eV
n = 9 l = 0 E = 0.752288E+01 eV	n = 9 l = 0 E = 0.146981E+02 eV	n = 9 l = 0 E = 0.316909E+02 eV
n = 9 l = 1 E = 0.757202E+01 eV	n = 9 l = 1 E = 0.148305E+02 eV	n = 9 l = 1 E = 0.319203E+02 eV
n = 9 l = 2 E = 0.766480E+01 eV	n = 9 l = 2 E = 0.150691E+02 eV	n = 9 l = 2 E = 0.323255E+02 eV
n = 9 l = 3 E = 0.771207E+01 eV	n = 9 l = 3 E = 0.152571E+02 eV	n = 9 l = 3 E = 0.326929E+02 eV
n = 10 l = 0 E = 0.761561E+01 eV	n = 10 l = 0 E = 0.149996E+02 eV	n = 10 l = 0 E = 0.322839E+02 eV
n = 10 l = 1 E = 0.764741E+01 eV	n = 10 l = 1 E = 0.150875E+02 eV	n = 10 l = 1 E = 0.324387E+02 eV
n = 10 l = 2 E = 0.771017E+01 eV	n = 10 l = 2 E = 0.152507E+02 eV	n = 10 l = 2 E = 0.327187E+02 eV
n = 10 l = 3 E = 0.774399E+01 eV	n = 10 l = 3 E = 0.153850E+02 eV	n = 10 l = 3 E = 0.329815E+02 eV

The energy and wavelength for transitions between various atomic levels in the neutral Ge atom are shown in Table 3. Indexes *ni, li* and *nf, lf* mean the initial and final states with the corresponding principal and orbital quantum numbers. These data on radiative transitions are available for all types of Ge ions.

Table 3. The energy and wavelength for transitions between atomic levels in neutral Ge atom.

ni =	4	li =	0	==>	nf =	4	lf =	1	E =	0.866506E+01	eV 0.143085E+03 nm
ni =	4	li =	0	==>	nf =	5	lf =	1	E =	0.145425E+02	eV 0.852564E+02 nm
ni =	4	li =	0	==>	nf =	6	lf =	1	E =	0.155126E+02	eV 0.799247E+02 nm
ni =	4	li =	0	==>	nf =	7	lf =	1	E =	0.159129E+02	eV 0.779143E+02 nm
ni =	4	li =	0	==>	nf =	8	lf =	1	E =	0.161179E+02	eV 0.769232E+02 nm
ni =	4	li =	0	==>	nf =	9	lf =	1	E =	0.162371E+02	eV 0.763587E+02 nm
ni =	4	li =	0	==>	nf =	10	lf =	1	E =	0.163125E+02	eV 0.760058E+02 nm
ni =	4	li =	1	==>	nf =	4	lf =	2	E =	0.634011E+01	eV 0.195555E+03 nm
ni =	4	li =	1	==>	nf =	5	lf =	0	E =	0.491605E+01	eV 0.252203E+03 nm
ni =	4	li =	1	==>	nf =	5	lf =	2	E =	0.701303E+01	eV 0.176791E+03 nm
ni =	4	li =	1	==>	nf =	6	lf =	0	E =	0.651839E+01	eV 0.190207E+03 nm
ni =	4	li =	1	==>	nf =	6	lf =	2	E =	0.732616E+01	eV 0.169235E+03 nm
ni =	4	li =	1	==>	nf =	7	lf =	0	E =	0.709663E+01	eV 0.174709E+03 nm
ni =	4	li =	1	==>	nf =	7	lf =	2	E =	0.749617E+01	eV 0.165397E+03 nm
ni =	4	li =	1	==>	nf =	8	lf =	0	E =	0.737109E+01	eV 0.168203E+03 nm
ni =	4	li =	1	==>	nf =	8	lf =	2	E =	0.759850E+01	eV 0.163169E+03 nm
ni =	4	li =	1	==>	nf =	9	lf =	0	E =	0.752288E+01	eV 0.164809E+03 nm
ni =	4	li =	1	==>	nf =	9	lf =	2	E =	0.766480E+01	eV 0.161758E+03 nm
ni =	4	li =	1	==>	nf =	10	lf =	0	E =	0.761561E+01	eV 0.162803E+03 nm
ni =	4	li =	1	==>	nf =	10	lf =	2	E =	0.771017E+01	eV 0.160806E+03 nm
ni =	4	li =	2	==>	nf =	4	lf =	3	E =	0.689766E+00	eV 0.179748E+04 nm
ni =	4	li =	2	==>	nf =	5	lf =	3	E =	0.995785E+00	eV 0.124509E+04 nm
ni =	4	li =	2	==>	nf =	6	lf =	1	E =	0.507457E+00	eV 0.244325E+04 nm
ni =	4	li =	2	==>	nf =	6	lf =	3	E =	0.116204E+01	eV 0.106695E+04 nm
ni =	4	li =	2	==>	nf =	7	lf =	1	E =	0.907740E+00	eV 0.136586E+04 nm
ni =	4	li =	2	==>	nf =	7	lf =	3	E =	0.126229E+01	eV 0.982219E+03 nm
ni =	4	li =	2	==>	nf =	8	lf =	1	E =	0.111275E+01	eV 0.111421E+04 nm
ni =	4	li =	2	==>	nf =	8	lf =	3	E =	0.132735E+01	eV 0.934071E+03 nm
ni =	4	li =	2	==>	nf =	9	lf =	1	E =	0.123191E+01	eV 0.100644E+04 nm
ni =	4	li =	2	==>	nf =	9	lf =	3	E =	0.137196E+01	eV 0.903699E+03 nm
ni =	4	li =	2	==>	nf =	10	lf =	1	E =	0.130731E+01	eV 0.948395E+03 nm
ni =	4	li =	2	==>	nf =	10	lf =	3	E =	0.140389E+01	eV 0.883149E+03 nm
ni =	4	li =	3	==>	nf =	6	lf =	2	E =	0.296284E+00	eV 0.418464E+04 nm
ni =	4	li =	3	==>	nf =	7	lf =	2	E =	0.466295E+00	eV 0.265892E+04 nm
ni =	4	li =	3	==>	nf =	8	lf =	2	E =	0.568629E+00	eV 0.218041E+04 nm
ni =	4	li =	3	==>	nf =	9	lf =	2	E =	0.634926E+00	eV 0.195273E+04 nm
ni =	4	li =	3	==>	nf =	10	lf =	2	E =	0.680302E+00	eV 0.182249E+04 nm
ni =	5	li =	0	==>	nf =	5	lf =	1	E =	0.961403E+00	eV 0.128962E+04 nm
ni =	5	li =	0	==>	nf =	6	lf =	1	E =	0.193151E+01	eV 0.641903E+03 nm
ni =	5	li =	0	==>	nf =	7	lf =	1	E =	0.233179E+01	eV 0.531712E+03 nm
ni =	5	li =	0	==>	nf =	8	lf =	1	E =	0.253681E+01	eV 0.488741E+03 nm
ni =	5	li =	0	==>	nf =	9	lf =	1	E =	0.265596E+01	eV 0.466814E+03 nm
ni =	5	li =	0	==>	nf =	10	lf =	1	E =	0.273136E+01	eV 0.453928E+03 nm
ni =	5	li =	1	==>	nf =	4	lf =	2	E =	0.462651E+00	eV 0.267987E+04 nm
ni =	5	li =	1	==>	nf =	5	lf =	2	E =	0.113557E+01	eV 0.109182E+04 nm
ni =	5	li =	1	==>	nf =	6	lf =	0	E =	0.640935E+00	eV 0.193443E+04 nm

ni = 5 li = 1 ==> nf = 6 lf = 2 E = 0.144870E+01 eV 0.855830E+03 nm
ni = 5 li = 1 ==> nf = 7 lf = 0 E = 0.121918E+01 eV 0.101695E+04 nm
ni = 5 li = 1 ==> nf = 7 lf = 2 E = 0.161871E+01 eV 0.765944E+03 nm
ni = 5 li = 1 ==> nf = 8 lf = 0 E = 0.149364E+01 eV 0.830081E+03 nm
ni = 5 li = 1 ==> nf = 8 lf = 2 E = 0.172105E+01 eV 0.720400E+03 nm
ni = 5 li = 1 ==> nf = 9 lf = 0 E = 0.164543E+01 eV 0.753508E+03 nm
ni = 5 li = 1 ==> nf = 9 lf = 2 E = 0.178734E+01 eV 0.693679E+03 nm
ni = 5 li = 1 ==> nf = 10 lf = 0 E = 0.173815E+01 eV 0.713311E+03 nm
ni = 5 li = 1 ==> nf = 10 lf = 2 E = 0.183272E+01 eV 0.676504E+03 nm
ni = 5 li = 2 ==> nf = 4 lf = 3 E = 0.168438E-01 eV 0.736082E+05 nm
ni = 5 li = 2 ==> nf = 5 lf = 3 E = 0.322863E+00 eV 0.384015E+04 nm
ni = 5 li = 2 ==> nf = 6 lf = 3 E = 0.489116E+00 eV 0.253486E+04 nm
ni = 5 li = 2 ==> nf = 7 lf = 1 E = 0.234818E+00 eV 0.528001E+04 nm
ni = 5 li = 2 ==> nf = 7 lf = 3 E = 0.589365E+00 eV 0.210369E+04 nm
ni = 5 li = 2 ==> nf = 8 lf = 1 E = 0.439833E+00 eV 0.281889E+04 nm
ni = 5 li = 2 ==> nf = 8 lf = 3 E = 0.654431E+00 eV 0.189453E+04 nm
ni = 5 li = 2 ==> nf = 9 lf = 1 E = 0.558989E+00 eV 0.221801E+04 nm
ni = 5 li = 2 ==> nf = 9 lf = 3 E = 0.699041E+00 eV 0.177363E+04 nm
ni = 5 li = 2 ==> nf = 10 lf = 1 E = 0.634384E+00 eV 0.195440E+04 nm
ni = 5 li = 2 ==> nf = 10 lf = 3 E = 0.730966E+00 eV 0.169617E+04 nm
ni = 5 li = 3 ==> nf = 7 lf = 2 E = 0.160275E+00 eV 0.773569E+04 nm
ni = 5 li = 3 ==> nf = 8 lf = 2 E = 0.262610E+00 eV 0.472123E+04 nm
ni = 5 li = 3 ==> nf = 9 lf = 2 E = 0.328907E+00 eV 0.376958E+04 nm
ni = 5 li = 3 ==> nf = 10 lf = 2 E = 0.374282E+00 eV 0.331258E+04 nm
ni = 6 li = 0 ==> nf = 6 lf = 1 E = 0.329173E+00 eV 0.376654E+04 nm
ni = 6 li = 0 ==> nf = 7 lf = 1 E = 0.729456E+00 eV 0.169968E+04 nm
ni = 6 li = 0 ==> nf = 8 lf = 1 E = 0.934471E+00 eV 0.132679E+04 nm
ni = 6 li = 0 ==> nf = 9 lf = 1 E = 0.105363E+01 eV 0.117674E+04 nm
ni = 6 li = 0 ==> nf = 10 lf = 1 E = 0.112902E+01 eV 0.109816E+04 nm
ni = 6 li = 1 ==> nf = 5 lf = 2 E = 0.165465E+00 eV 0.749306E+04 nm
ni = 6 li = 1 ==> nf = 6 lf = 2 E = 0.478593E+00 eV 0.259060E+04 nm
ni = 6 li = 1 ==> nf = 7 lf = 0 E = 0.249068E+00 eV 0.497793E+04 nm
ni = 6 li = 1 ==> nf = 7 lf = 2 E = 0.648604E+00 eV 0.191155E+04 nm
ni = 6 li = 1 ==> nf = 8 lf = 0 E = 0.523532E+00 eV 0.236823E+04 nm
ni = 6 li = 1 ==> nf = 8 lf = 2 E = 0.750938E+00 eV 0.165106E+04 nm
ni = 6 li = 1 ==> nf = 9 lf = 0 E = 0.675319E+00 eV 0.183594E+04 nm
ni = 6 li = 1 ==> nf = 9 lf = 2 E = 0.817235E+00 eV 0.151712E+04 nm
ni = 6 li = 1 ==> nf = 10 lf = 0 E = 0.768044E+00 eV 0.161429E+04 nm
ni = 6 li = 1 ==> nf = 10 lf = 2 E = 0.862611E+00 eV 0.143731E+04 nm
ni = 6 li = 2 ==> nf = 5 lf = 3 E = 0.973511E-02 eV 0.127358E+06 nm
ni = 6 li = 2 ==> nf = 6 lf = 3 E = 0.175988E+00 eV 0.704503E+04 nm
ni = 6 li = 2 ==> nf = 7 lf = 3 E = 0.276237E+00 eV 0.448833E+04 nm
ni = 6 li = 2 ==> nf = 8 lf = 1 E = 0.126705E+00 eV 0.978529E+04 nm
ni = 6 li = 2 ==> nf = 8 lf = 3 E = 0.341303E+00 eV 0.363267E+04 nm
ni = 6 li = 2 ==> nf = 9 lf = 1 E = 0.245861E+00 eV 0.504287E+04 nm
ni = 6 li = 2 ==> nf = 9 lf = 3 E = 0.385913E+00 eV 0.321275E+04 nm
ni = 6 li = 2 ==> nf = 10 lf = 1 E = 0.321256E+00 eV 0.385936E+04 nm
ni = 6 li = 2 ==> nf = 10 lf = 3 E = 0.417838E+00 eV 0.296728E+04 nm
ni = 6 li = 3 ==> nf = 8 lf = 2 E = 0.963569E-01 eV 0.128672E+05 nm
ni = 6 li = 3 ==> nf = 9 lf = 2 E = 0.162654E+00 eV 0.762258E+04 nm
ni = 6 li = 3 ==> nf = 10 lf = 2 E = 0.208029E+00 eV 0.595994E+04 nm

ni = 7 li = 0 ==> nf = 7 lf = 1 E = 0.151216E+00 eV 0.819917E+04 nm
ni = 7 li = 0 ==> nf = 8 lf = 1 E = 0.356230E+00 eV 0.348045E+04 nm
ni = 7 li = 0 ==> nf = 9 lf = 1 E = 0.475386E+00 eV 0.260807E+04 nm
ni = 7 li = 0 ==> nf = 10 lf = 1 E = 0.550781E+00 eV 0.225106E+04 nm
ni = 7 li = 1 ==> nf = 6 lf = 2 E = 0.783100E-01 eV 0.158325E+05 nm
ni = 7 li = 1 ==> nf = 7 lf = 2 E = 0.248321E+00 eV 0.499291E+04 nm
ni = 7 li = 1 ==> nf = 8 lf = 0 E = 0.123249E+00 eV 0.100597E+05 nm
ni = 7 li = 1 ==> nf = 8 lf = 2 E = 0.350655E+00 eV 0.353579E+04 nm
ni = 7 li = 1 ==> nf = 9 lf = 0 E = 0.275035E+00 eV 0.450794E+04 nm
ni = 7 li = 1 ==> nf = 9 lf = 2 E = 0.416952E+00 eV 0.297358E+04 nm
ni = 7 li = 1 ==> nf = 10 lf = 0 E = 0.367760E+00 eV 0.337133E+04 nm
ni = 7 li = 1 ==> nf = 10 lf = 2 E = 0.462327E+00 eV 0.268174E+04 nm
ni = 7 li = 2 ==> nf = 6 lf = 3 E = 0.597763E-02 eV 0.207414E+06 nm
ni = 7 li = 2 ==> nf = 7 lf = 3 E = 0.106226E+00 eV 0.116717E+05 nm
ni = 7 li = 2 ==> nf = 8 lf = 3 E = 0.171293E+00 eV 0.723815E+04 nm
ni = 7 li = 2 ==> nf = 9 lf = 1 E = 0.758500E-01 eV 0.163460E+05 nm
ni = 7 li = 2 ==> nf = 9 lf = 3 E = 0.215902E+00 eV 0.574261E+04 nm
ni = 7 li = 2 ==> nf = 10 lf = 1 E = 0.151245E+00 eV 0.819757E+04 nm
ni = 7 li = 2 ==> nf = 10 lf = 3 E = 0.247827E+00 eV 0.500285E+04 nm
ni = 7 li = 3 ==> nf = 9 lf = 2 E = 0.624051E-01 eV 0.198676E+05 nm
ni = 7 li = 3 ==> nf = 10 lf = 2 E = 0.107780E+00 eV 0.115034E+05 nm
ni = 8 li = 0 ==> nf = 8 lf = 1 E = 0.817661E-01 eV 0.151633E+05 nm
ni = 8 li = 0 ==> nf = 9 lf = 1 E = 0.200922E+00 eV 0.617076E+04 nm
ni = 8 li = 0 ==> nf = 10 lf = 1 E = 0.276317E+00 eV 0.448703E+04 nm
ni = 8 li = 1 ==> nf = 7 lf = 2 E = 0.433059E-01 eV 0.286299E+05 nm
ni = 8 li = 1 ==> nf = 8 lf = 2 E = 0.145640E+00 eV 0.851304E+04 nm
ni = 8 li = 1 ==> nf = 9 lf = 0 E = 0.700207E-01 eV 0.177068E+05 nm
ni = 8 li = 1 ==> nf = 9 lf = 2 E = 0.211937E+00 eV 0.585004E+04 nm
ni = 8 li = 1 ==> nf = 10 lf = 0 E = 0.162745E+00 eV 0.761829E+04 nm
ni = 8 li = 1 ==> nf = 10 lf = 2 E = 0.257313E+00 eV 0.481842E+04 nm
ni = 8 li = 2 ==> nf = 7 lf = 3 E = 0.389194E-02 eV 0.318566E+06 nm
ni = 8 li = 2 ==> nf = 8 lf = 3 E = 0.689583E-01 eV 0.179796E+05 nm
ni = 8 li = 2 ==> nf = 9 lf = 3 E = 0.113568E+00 eV 0.109172E+05 nm
ni = 8 li = 2 ==> nf = 10 lf = 1 E = 0.489106E-01 eV 0.253491E+05 nm
ni = 8 li = 2 ==> nf = 10 lf = 3 E = 0.145493E+00 eV 0.852169E+04 nm
ni = 8 li = 3 ==> nf = 10 lf = 2 E = 0.427141E-01 eV 0.290265E+05 nm
ni = 9 li = 0 ==> nf = 9 lf = 1 E = 0.491352E-01 eV 0.252333E+05 nm
ni = 9 li = 0 ==> nf = 10 lf = 1 E = 0.124530E+00 eV 0.995615E+04 nm
ni = 9 li = 1 ==> nf = 8 lf = 2 E = 0.264845E-01 eV 0.468139E+05 nm
ni = 9 li = 1 ==> nf = 9 lf = 2 E = 0.927815E-01 eV 0.133630E+05 nm
ni = 9 li = 1 ==> nf = 10 lf = 0 E = 0.435896E-01 eV 0.284435E+05 nm
ni = 9 li = 1 ==> nf = 10 lf = 2 E = 0.138157E+00 eV 0.897416E+04 nm
ni = 9 li = 2 ==> nf = 8 lf = 3 E = 0.266123E-02 eV 0.465891E+06 nm
ni = 9 li = 2 ==> nf = 9 lf = 3 E = 0.472708E-01 eV 0.262285E+05 nm
ni = 9 li = 2 ==> nf = 10 lf = 3 E = 0.791955E-01 eV 0.156555E+05 nm
ni = 10 li = 0 ==> nf = 10 lf = 1 E = 0.318055E-01 eV 0.389820E+05 nm
ni = 10 li = 1 ==> nf = 9 lf = 2 E = 0.173864E-01 eV 0.713109E+05 nm
ni = 10 li = 1 ==> nf = 10 lf = 2 E = 0.627618E-01 eV 0.197547E+05 nm
ni = 10 li = 2 ==> nf = 9 lf = 3 E = 0.189543E-02 eV 0.654123E+06 nm
ni = 10 li = 2 ==> nf = 10 lf = 3 E = 0.338202E-01 eV 0.366599E+05 nm

2.6.2 Populations of atomic levels, electron and ion composition of Ge WDP

The calculated atomic data are then used in the collisional-radiative steady-state (CRSS) model [15, 44] for calculating the populations of atomic levels, ion and electron plasma composition, and ionization balance. The collisional processes include collisional excitation and re-excitation, collisional ionization, and three-body recombination. The radiative processes include discrete spontaneous transitions, photo-recombination, and dielectronic recombination. The semi-empirical formulas involving the calculated HFS data are used to evaluate the cross-sections of these collisional and radiative processes [44]. The CRSS model satisfactorily describes only the optically thin plasma. For the optically thick plasma, the self-consistent effects due to the non-local radiative flux are taken into account in the form of escape factor [44] for line transitions and direct photoionization for the continuum spectrum. The CRSS populations of atomic levels for a range of plasma densities and temperatures are calculated according to the system of kinetic equations [44]

$$\frac{dn_i}{dt} = -n_i \sum_{j \neq i} K_{ij} + \sum_{i \neq j} n_j K_{ji} = 0 \,, \tag{38}$$

where n_i and n_j are populations of atomic levels i and j, K_{ij} and K_{ji} are transition rates from level i to other levels j and from other levels j to this level i, respectively. One equation corresponds to each atomic level. The rates are expressed through the cross-section of collisional and radiative processes using semi-empirical formula [44]. From the calculated population of

atomic levels n_i, ion and electron concentrations, N_i and N_e, can be determined for a given plasma density and temperature.

For high-density plasmas, the nearby ions play a significant role leading to the effects such as alterations of electronic structure and energy levels of ions, reduction of ionization potentials, spectral line shift and broadening, changes in line shapes, absorption and emission spectra [15]. At high densities, the wavefunctions of several neighboring ions overlap forming quasi-molecules. In low-temperature and high-density plasma, the ions are packed tightly. The sphere that encloses the nucleus, bound electrons and free electrons of each ion can be considered as an appropriate model. The charge neutrality is satisfied inside the ion sphere volume with a uniform electron distribution. Beyond the ion sphere the plasma is assumed as an electrically neutral background. The atomic data calculated for the isolated ions are used in the HFS-CRSS model with the ionization potential depression (continuum lowering). The ionization potential I_i of i-th isolated ion is reduced by the value $\Delta I_i = I_i - I_i'$ that is calculated as

$$\Delta I_i = \frac{3}{2}\frac{Ry\, a_0\, i}{R_i}\left\{\left[1+\left(\frac{R_D}{R_i}\right)^3\right]^{2/3} - \left(\frac{R_D}{R_i}\right)^2\right\}, \tag{39}$$

where I_i' is the lowered ionization potential of i-th ion in a dense plasma, i is the ion charge or the number of electrons removed from the ion, Ry is the Rydberg constant, a_0 is the Bohr radius, $R_i = \left[(3(i+1))/(4\pi N_e)\right]^{1/3}$ is the ion-sphere radius of i-th ion, N_e is the density of free electrons, $R_D = \sqrt{kT_e/\left(4\pi N_e\left(1+\langle Z\rangle\right)e^2\right)}$ is the Debye radius, T_e is the electron temperature, $\langle Z\rangle = N_e / N$ and N are the average charge state and the number density of the ions. This equation interpolates

between the low-density Debye screening and the high-dense ion-sphere limit. A sphere is constructed around each ion with the point charge Ze in such a way that the neutralizing electrons exactly cancel the charge of the ion. Some of these electrons are bound and some of them are free. The reduction ΔI_i results in lowering of continuum level, shifts of bound-electron energy levels towards the continuum, and disappearance of bound states. All the energy levels are shifted by the same amount (to first approximation), so that the energy difference between the levels is not changed. As plasma density increases, the orbitals with energies above the lowered ionization potential I_i' are treated as ionized. The energy levels belonging to those orbitals are removed from the CRSS rate equations. This procedure reduces the number of bound electron states in the ions.

The shift in the positions of spectral lines, called the polarization shift, is occurred in dense plasmas. The polarization induced by free electrons modifies the energy of photons emitted during a transition between two levels. Assuming a uniform electron distribution in the ion sphere, the shift of a spectral line in i-th ion is calculated as follows

$$\Delta\varepsilon_i = \frac{1}{2}\frac{(i+1)e^2}{R_i^3}\left(r_b^2 - r_a^2\right), \tag{40}$$

where $r_a^2 = \langle a \,|\, r^2 \,|\, a \rangle$ and $r_b^2 = \langle b \,|\, r^2 \,|\, b \rangle$ are the average values of the square of radial distance r at the initial state $|\, a \rangle$ and the final state $|\, b \rangle$ of photon transition between two discrete energy levels. The values of r_a^2 and r_b^2 are determined from the HFS model. The line shift $\Delta\varepsilon_i$ is negative meaning that the photon wavelength is increased (red shift). The wavelength shift of spectral lines is rather small.

The number density of free electrons and the average charge state of Ge ions are plotted in Fig. 22 for the solid-state density plasma as a function of temperature [45].

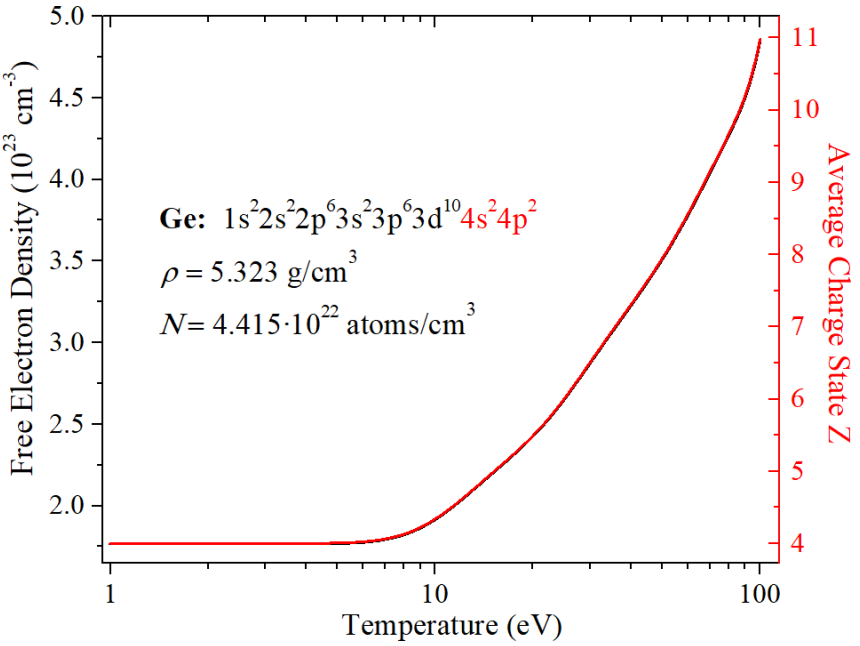

Fig. 22. The number density of free electrons in Ge WDP at solid density as a function of temperature.

It is seen in Fig. 22 that even at low temperatures, ~1 eV, the four outer electrons from the 4s and 4p shells are ionized (see the scale in red on the right-hand side of plot) in the solid-state warm Ge plasma. As the WDP temperature increases from ~10 eV to ~100 eV, the average charge of plasma increases with ~11 electrons ionized at 100 eV and the number density of free electrons reaches ~5·10^{23} cm^{-3}.

The charge state distribution of ion species in Ge WDP of the solid-state density as a function of temperature is illustrated in Fig. 23.

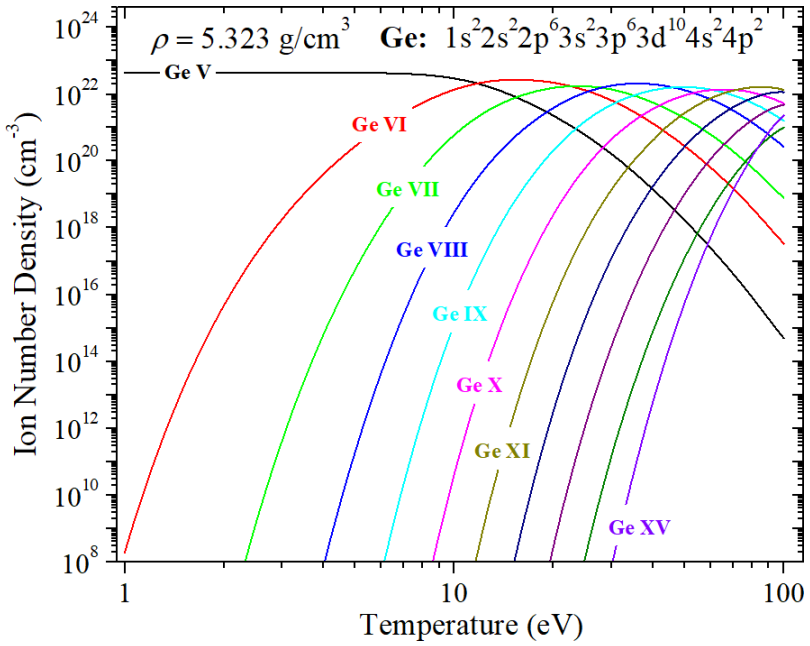

Fig. 23. The number density of different ion species in Ge WDP at solid density as a function of temperature.

It is seen that the lowest charge state at 1 eV corresponds to the Ge V ions. The ionic charge states with two electrons in the 4s orbital and two electrons in the 4p orbital do not survive the ionization potential lowering due to density effects. With increasing the temperature up to ~10 eV, the number density of various multi-ionized Ge ions (Ge VI, Ge VII, Ge VIII, etc.) is increasing successively as a function of temperature. The warm dense Ge plasma is composed from Ge V at ~1 eV to Ge XI at ~100 eV. At this high temperature ~100 eV, the 3d shell of Ge is completely ionized. The general feature of the charge state distribution of Ge ions is that the partial density of the most abundant charge state shifts toward the highly charged ions as the temperature increases.

2.6.3 Emission spectra of Ge WDP

The emission of photons in plasma originates from three types of radiative transitions: bound-bound, bound-free and free-free transitions [44]. In the HFS-CRSS model, the total absorption coefficient depends on the plasma temperature $T = T_e$, plasma density N and photon energy ε. It can be expressed as the sum of contributions from bound-bound, bound-free and free-free transitions [44]

$$Q_{tot}(T,N,\varepsilon) = Q_{bb}(T,N,\varepsilon) + Q_{bf}(T,N,\varepsilon) + Q_{ff}(T,N,\varepsilon), \tag{41}$$

with

$$Q_{bb}(T,N,\varepsilon) = \sum_i \sum_j \sigma_{ij}^{bb}(\varepsilon) \cdot K_{ij}(T,N), \tag{42}$$

$$Q_{bf}(T,N,\varepsilon) = \sum_i \sum_j \sigma_{ij}^{bf}(\varepsilon) \cdot K_{ij}(T,N), \tag{43}$$

$$Q_{ff}(T,N,\varepsilon) = N_e(T,N) \times \sum_i \sigma_i^{ff}(T,\varepsilon)\left(1 - e^{-\varepsilon/kT}\right) N_i(T,N). \tag{44}$$

The corresponding cross-sections of radiative transition processes σ are calculated using semi-empirical formula [44]. Line radiation absorbed or emitted from bound-bound transitions has a peak of intensity at an energy corresponding to the energy difference between two bound levels. The profiles of spectral lines include natural (radiation damping), Stark, Doppler and resonance broadening. The main part of the line transitions is non-uniformly distributed over low photon energies with line intensities having non-regular character. The bound-free transitions correspond to ionization/recombination radiation whose energies are the sum of the kinetic energy of the

ionizing/recombining electron and the binding energy of the shell that the electron leaves/drops from/to. This radiation is distributed over higher photon energies starting with a discontinuity at the threshold energy corresponding to the binding energy. Bremsstrahlung radiation originates from free-free transitions when a free electron changes its kinetic energy in a collision with electrons and ions. This radiation is distributed over all photon energies.

The emissivity of Ge WDP is shown in Figs. 24 and 25 for 40 and 80 eV, respectively. The emission spectra are plotted for plasma density of $0.01\rho_0$, $0.1\rho_0$ and ρ_0, where $\rho_0 = 5.323$ g/cm^3 is the solid density of Ge [45]. The emissivities are shown in the soft X-ray and UV regions. There is photon emission in spectral lines at density of $0.01\rho_0$ that increases with the increase of temperature from 40 eV to 80 eV. More spectral lines are present in the soft X-ray region from 2 nm to 10 nm at higher temperature.

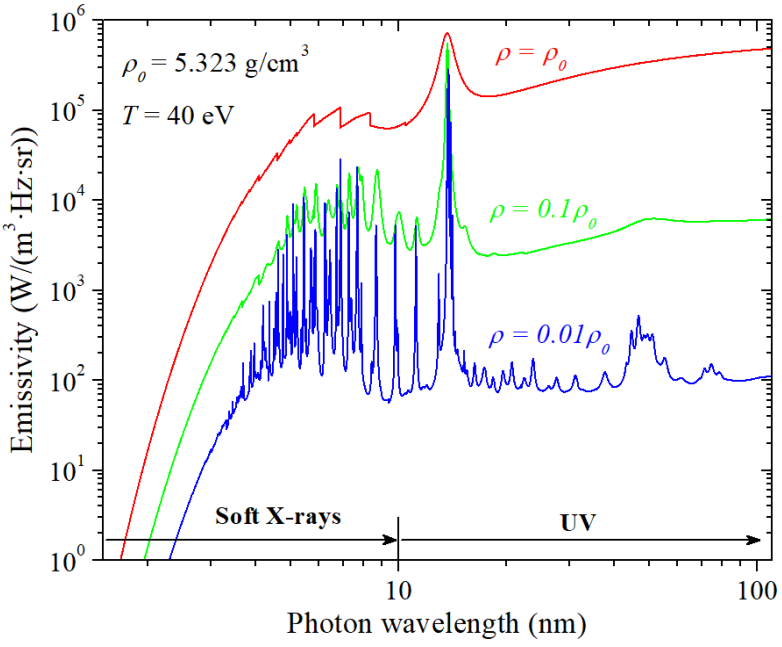

Fig. 24. The emissivities of Ge plasma at temperature of 40 eV as a function of photon wavelength for three values of mass density.

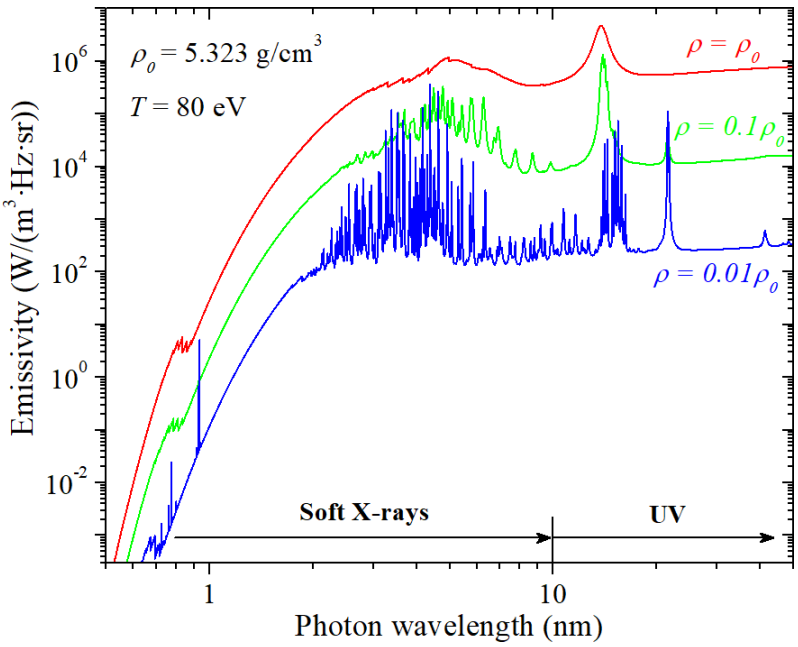

Fig. 25. The emissivities of Ge plasma at temperature of 80 eV as a function of photon wavelength for three values of mass density.

The shift of X-ray emission in lines to shorter wavelengths is observed with increase of temperature. As the density is increased to $0.1\rho_0$, the overall emissivity of Ge plasma is also increased. However, many emission lines disappear in the spectrum due to the depression of the ionization potential resulting in broadening, overlapping, and vanishing of these spectral lines. At solid density ρ_0, there is no line emission present in the spectrum. The emissivity is higher, but the emitted radiation is continuous.

2.7 Modeling of radiation transfer in warm and hot dense plasmas

The transfer of radiation in a plasma is generally described by complicated radiative transfer equations. Due to the great complexity of the problem the existing standard methods (flux-limited diffusion, differential or integral finite difference schemes) quite often treat not the most general case of solving the three-dimensional, multi-frequency, time-dependent radiative transfer equations. An alternative approach to solving the radiative transfer problem is a MC technique [46]. It is based on tracing individual photons along their direction of propagation within a plasma. The MC code MCOURT standing for **M**onte **C**arlo of **O**ptical and **U**ltraviolet **R**adiative **T**ransfer was developed for studying the radiative transfer of photons and X-rays in plasmas. The MCOURT code can treat inhomogeneous radiative sources in the 3D Cartesian and cylindrical geometry. It is intended to be an accurate alternative to the current codes which rely on algorithms based on an approximate solution of the Boltzmann equation of radiation transfer. The MCOURT code was validated against several analytical benchmark problems showing a very good agreement for predicting the radiation transfer in plasmas.

2.7.1 Validation of MCOURT results against the 1D analytical benchmark problem

The radiative transfer calculated from the MCOURT code was validated against the 1D analytical benchmark problem. The theory for analytical calculations of the energy and number of emitted photons is briefly outlined. Volume of plasma is split into cells. The energy of photons emitted from i, j, k plasma cell can be calculated as follows

$$E_{i,j,k} = \pi \int_{\varepsilon} k\left(\varepsilon, T_{i,j,k}\right) B\left(\varepsilon, T_{i,j,k}\right) d\varepsilon \,, \tag{45}$$

where ε is the energy of photons, $T_{i,j,k}$ is the temperature in i, j, k cell and $k\left(\varepsilon, T_{i,j,k}\right)$ is the emission coefficient which is assumed to be constant within i, j, k cell. The Planck function [47]

$$B\left(\varepsilon, T_{i,j,k}\right) = \frac{8\pi\varepsilon^3}{c^2 h^3} \frac{1}{\exp(\varepsilon / kT_{i,j,k}) - 1} \tag{46}$$

accounts for the emission in all directions (angle averaged). The energy emitted from the whole volume can be calculated as the sum $E = \sum_{i,j,k} V_{i,j,k} E_{i,j,k}$, where $V_{i,j,k}$ is the volume of i, j, k cell. The number of photons emitted from i, j, k plasma cell is calculated as

$$N_{i,j,k} = \pi \int_{\varepsilon} k\left(\varepsilon, T_{i,j,k}\right) \frac{B\left(\varepsilon, T_{i,j,k}\right)}{\varepsilon} d\varepsilon \,. \tag{47}$$

The total number of photons generated in the whole volume is $N = \sum_{i,j,k} V_{i,j,k} N_{i,j,k}$. For 1D analytic benchmark problem, a temperature profile of the Xe plasma is demonstrated in Fig. 26. The plasma is hot (~300 eV) near Z ~ 0 cm, and the temperature drops sharply below ~1 eV within ~150 cm. The plasma density is 10^{20} cm^{-3}. The grid step along the plasma depth (Z-axis) was chosen to be 10 cm. In other two directions (X and Y coordinates), the plasma is homogeneous within each cell. In those directions a single cell with the size 10^{20} cm was used to represent an infinite plasma layer.

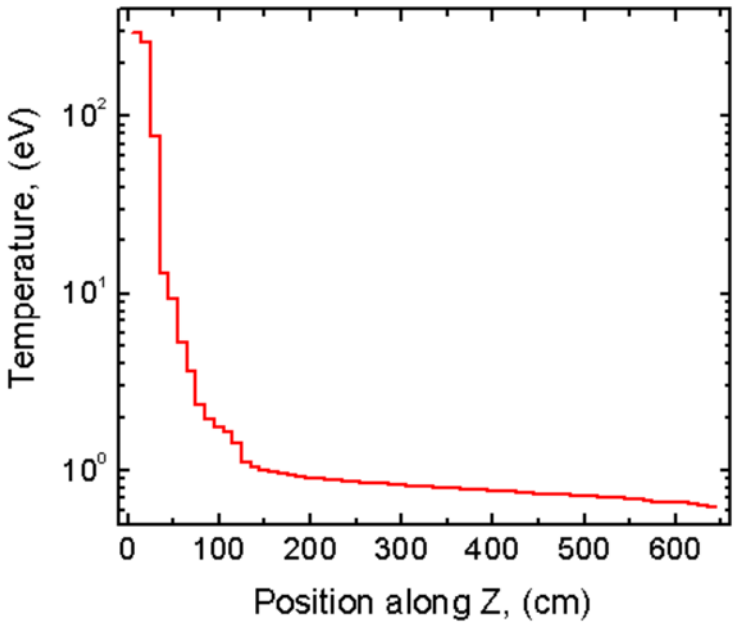

Fig. 26. A temperature profile of the Xe plasma.

To avoid the escape of photons from the faces that are perpendicular to the X and Y axes the position of photons was always started on the Z-axis. One million of photon histories was followed. The MC averaged total emission energy is $3.925 \cdot 10^{-2}$ MW. The MC averaged number of total emission photons is $1.58 \cdot 10^{21}$ photons/sec. The MC average of the emission energy per photon ε_{avg} is 155.197 eV. These values are in very good agreement with those calculated analytically. The analytical value of the total emission energy is $3.917 \cdot 10^{-2}$ MW. The total number of photons emitted from the plasma volume is $1.58 \cdot 10^{21}$ photons/sec. The average emission energy per photon $\varepsilon_{avg} = E / N$ is 154.9 eV.

The analytically calculated and MC sampled energy density profiles of emitted photons as a function of the plasma depth are shown in Fig. 27. The energy distribution (red curve) was calculated from Eq. (45). The blue curve is a result of the MC average over one million of photons.

It is seen in Fig. 27 that the agreement is perfect. The MC sampled distribution (blue curve) of the number of emitted photons as a function of the plasma depth is compared in Fig. 28 with the analytic distribution (red curve) calculated using Eq. (47). The agreement is also perfect.

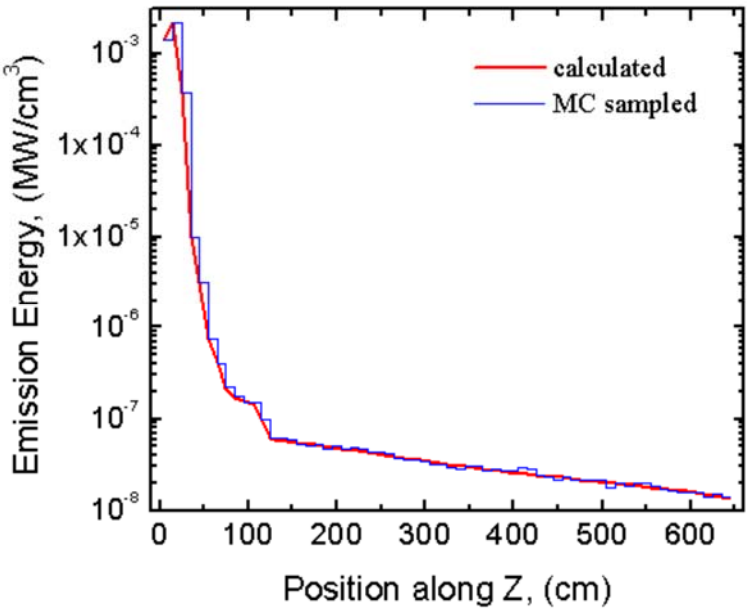

Fig. 27. The energy density of emitted photons as a function of plasma depth.

The distributions of absorbed energy and the number of absorbed photons are shown in Figs. 29 and 30, respectively. The emission energy and photon number are also illustrated. The redistribution of the photon energy from hot plasma region into cold region is clearly seen. The total energy absorbed in the plasma volume is $1.954 \cdot 10^{-2}$ MW. It is about 50% of the emission energy. The total number of photons absorbed in the plasma volume is $3.406 \cdot 10^{20}$ photons/sec.

As a source of atomic data for MCOURT, the absorption and emission coefficients in a range of plasma densities and temperatures calculated from the HFS-CRSS model are used. The detailed spectra with fully resolved spectral lines are implemented in the MCOURT simulations

of radiation transfer. MCOURT is used to model the transport of visible, ultraviolet and X-ray radiation in WDP with gradients of density and temperature. The studies are focused on the redistribution of energy in WDP due to radiative transfer.

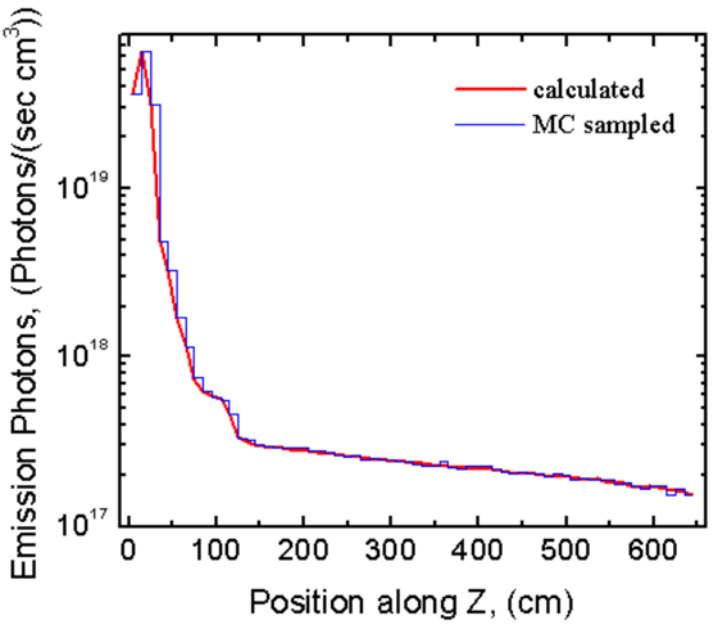

Fig. 28. The number of emitted photons as a function of plasma depth.

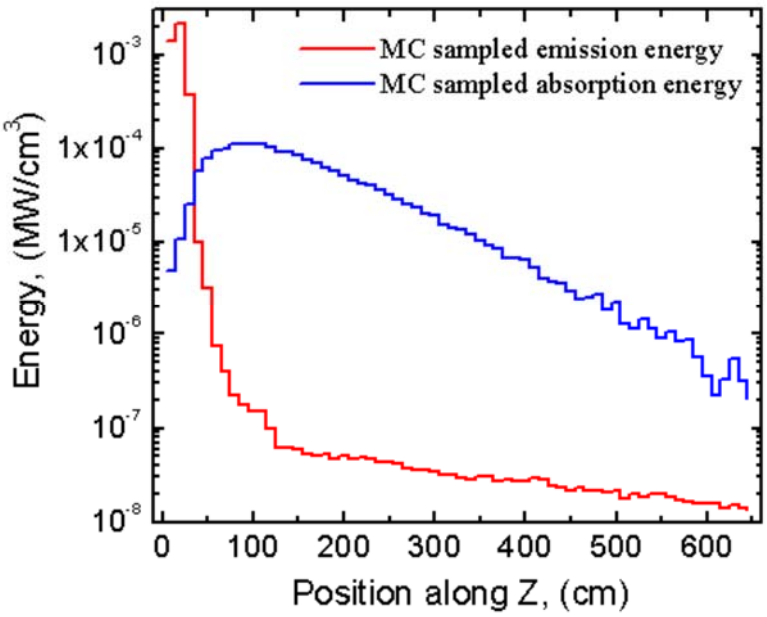

Fig. 29. The distribution of emitted and absorbed photon energy along the plasma depth.

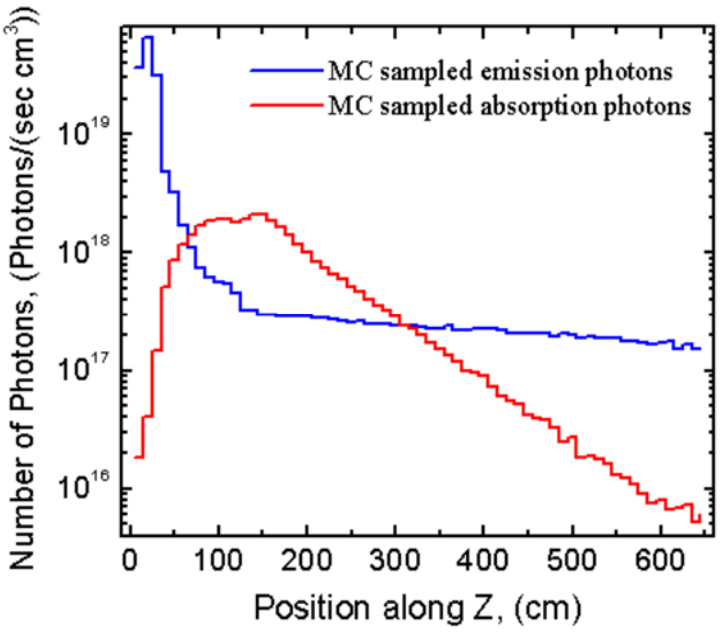

Fig. 30. The distribution of emitted and absorbed photons along the plasma depth.

2.7.2 MCOURT results on X-ray transport in warm and hot dense plasmas

The MCOURT code was used to investigate the transport of photons in Ge plasma with gradients of density and temperature. Profiles of density and temperature of WDP or HDP along the depth of Ge layer are extracted from the results of MSM-MD simulations for specific times (0.5 ps, 5 ps, and 10 ps) and used as an input for the MCOURT modeling of radiation transfer. The emission and absorption coefficients of Ge plasma calculated from the HFS-CRSS model were used as an input data for the modeling of the transport of visible, ultraviolet, and X-ray radiation. A table of the emission and absorption coefficients of Ge plasma was created in a wide range of mass density (from $7 \cdot 10^{-5}$ g/cm^3 to 7 g/cm^3) and temperature (from 0.025 eV to 20,000 eV) using 12 points per the order of density and temperature. This table covers the entire range of densities

and temperatures occurring in the Ge plasma during the X-ray induced blow-off. The detailed absorption and emission coefficients with fully resolved spectral lines (99,998 points over the range of photon energy from 0.05 eV to 100,000 eV) were used. The size of file with the optical properties of Ge plasma is about 10 GB.

The MCOURT modeling studies are focused on the redistribution of energy in a WDP or HDP due to the transport of photons and the prediction of spectral energy fluxes of photons emitted from a WDP or HDP into the free space (vacuum). The three cases of the energy and photon number redistribution due to the radiation transport and radiative fluxes emitted from a WDP or HDP are illustrated.

1) First case illustrates the mass density and temperature profiles of Ge plasma at time of 0.5 ps shown in Figs. 31 and 32, respectively. The depth of Ge layer treated in the MSM-MD modeling was 0.11316 μm. The Z-origin of Ge plasma (Z = 0) is taken at the bottom of MD-box. The original surface of a solid Ge layer is marked in Figs. 31 and 32 by a black line. It is seen in Fig. 31 that the main part of a Ge layer still remains at solid density of 5.323 g/cm^3 at time of 0.5 ps. The mass density drops to ~2 g/cm^3 slightly below the surface and sharply decreases to ~10^{-4} g/cm^3 above the surface within ~0.006 μm indicating the generation of a low-density Ge plasma. However, at 0.5 ps the temperature of solid Ge layer is already increased from ~6 eV at Z = 0 to ~70 eV near the surface (Fig. 32). The temperature of low-density plasma generated above the surface ranges from ~40 eV to ~600 eV.

Since the periodic X- and Y-boundaries were implemented in the MSM-MD modeling, the radiation transport problem was treated as a 1D problem. Photons were originated on the Z axis.

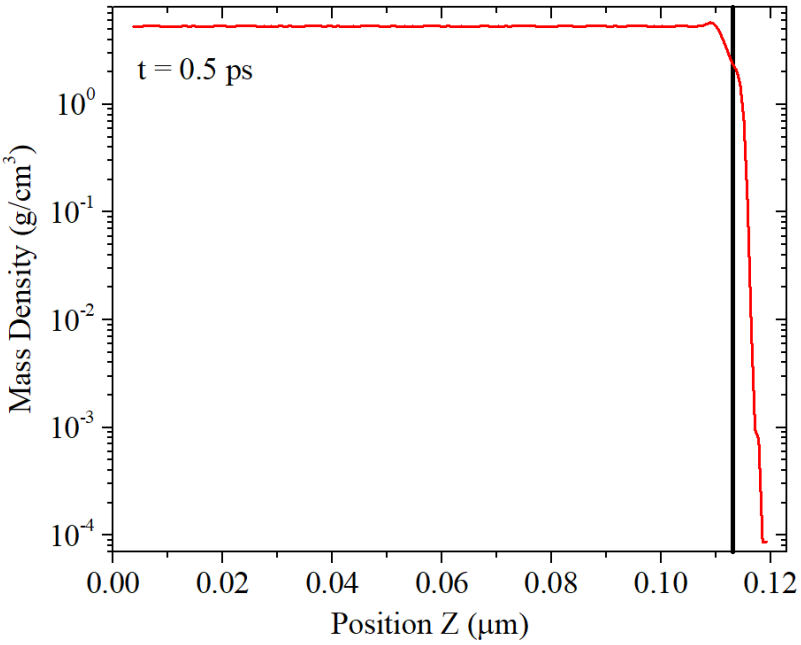

Fig. 31. Mass density of Ge plasma as a function of depth at 0.5 ps.

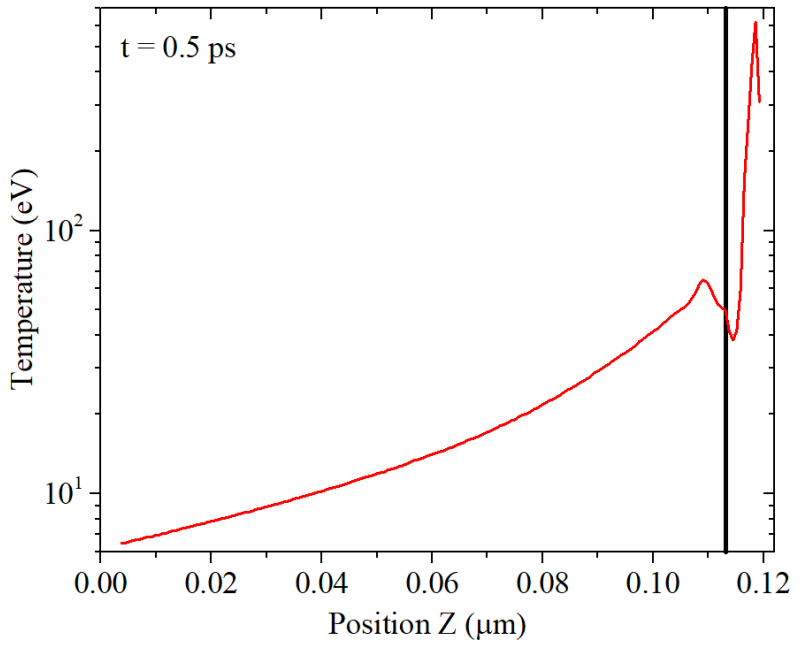

Fig. 32. Temperature of Ge plasma as a function of depth at 0.5 ps.

The lateral size of the box for radiation transport was set to a large value (10^{10} cm), so photons never escape through the lateral sides. However, photons were allowed to escape through the plane at Z = 0 into the bulk Ge material because the size of MD box filled with more than 10 million of Ge atoms was still limited to extent sufficiently deeply into the material.

The integral values of emitted, absorbed, and escaped radiation power as well as the total rates of emission, absorption, and escape of photons in/from a plasma layer with non-zero mass density are presented in Table 4.

Table 4. Total emitted, absorbed, and escaped radiation power and total rates of emission, absorption, and escape of photons from Ge plasma.

Total Emission Power, *GW*	Total Absorbed Power, *GW*	Total Escaped Power into Vacuum, *GW*	Total Escaped Power into Bulk, *GW*	Average Energy of Emitted Photons, *eV*	Rate of Photon Emission, *photons/s*	Rate of Photon Absorption, *photons/s*	Rate of Photon Escape into Vacuum, *photons/s*	Rate of Photon Escape into Bulk, *photons/s*
948.56	595.96	323.42	29.18	18.2	$3.26 \cdot 10^{29}$	$3.0 \cdot 10^{29}$	$2.24 \cdot 10^{28}$	$3.47 \cdot 10^{27}$

It is seen that the average energy of emitted photons is 18.2 eV. The analysis of these integral values demonstrates that the percentage of radiation power absorbed in a plasma is 62.8%. The considerable amount of radiation power, ~37.2%, is escaped. From this, the radiation power emitted into a vacuum, ~91.7%, is significantly higher than that deposited into the bulk Ge, ~8.3%. Concerning the rates of photon absorption and escape, they are 92.1% and 7.9%. The amount of photons escaped from a plasma is distributed as follows: 86.6% is emitted into a vacuum and 13.4% is escaped into a bulk Ge. This indicates that a significant portion of radiation power and number of photons generated in a plasma is irradiated into a vacuum and deposited into a bulk volume of Ge. The profiles of emitted and absorbed power density are shown in Fig. 33.

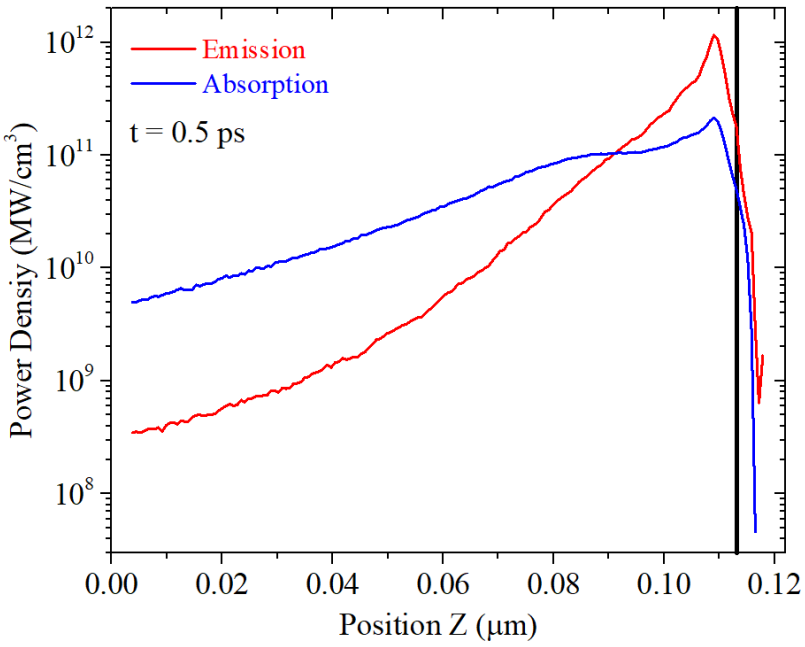

Fig. 33. Profiles of emitted and absorbed power density along the depth of a plasma at 0.5 ps.

It is seen that the energy is redistributed in a plasma by the radiation transport. The peak of photon emission and absorption occurs near Z ~ 0.11 μm, below the surface. At this peak, the emission power density is higher on both sides of the surface compared to the absorption power density. However, it is seen in Fig. 33 that a significant portion of emitted power density is redeposited into a dense, solid-state plasma in the region ~<0.09 μm. At Z = 0, the power density redeposited by the radiation transport is more than an order of magnitude higher than the emitted power density. This fact indicates that the radiative transfer is a quite important phenomenon that should be included in the modeling of the expanding plasma. This is also confirmed by the distribution of emitted and absorbed rates of photon number density along the depth of a plasma layer shown in Fig. 34. Rate of absorbed photons per unit volume is higher in the dense region ~<0.08 μm.

The spectral energy flux of photons that are escaped into a vacuum is shown in Fig. 35.

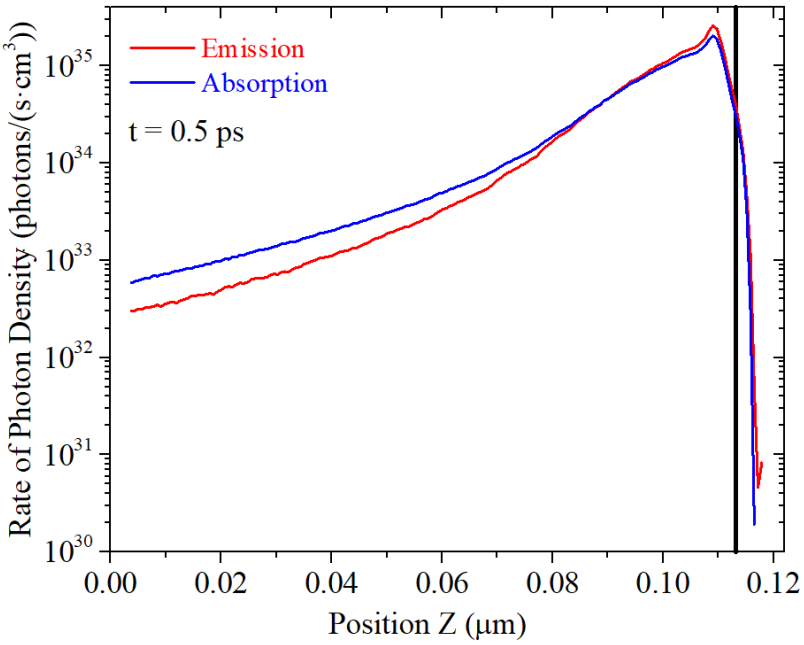

Fig. 34. Profiles of emitted and absorbed photons along the depth of a plasma at 0.5 ps.

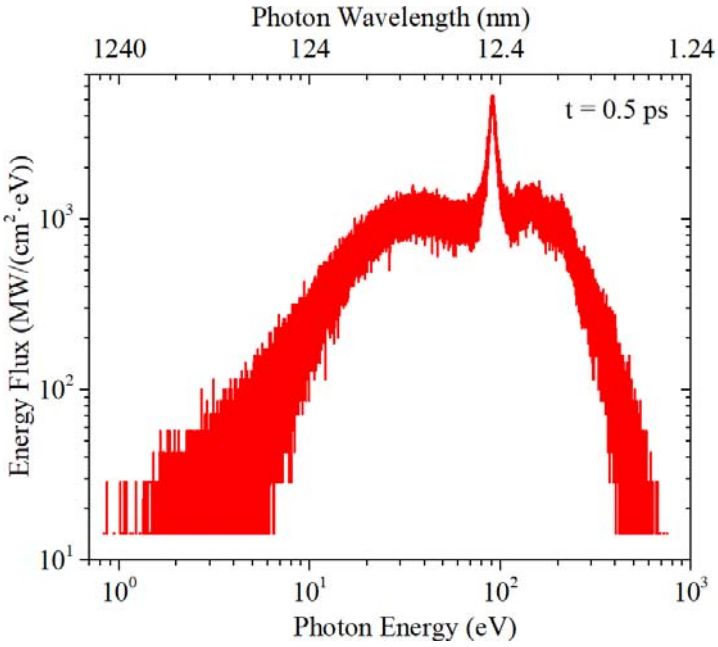

Fig. 35. Spectral energy flux of photons emitted from a plasma into a vacuum at 0.5 ps.

There is a peak in the flux for photons with the energy ~90 eV (~13.78 nm). The fraction of photons with lower (up to ~1 eV or ~1240 nm) and higher (up to ~1000 eV or ~1.24 nm) energies is significantly decreased. Thus, the emission spectrum of photons covers a range from near-infrared light to soft X-rays.

The angular distribution of photon energy flux emitted into a vacuum is illustrated in Fig. 36. The angle is counted from the normal to the target surface. It is seen that the majority of photons is emitted within 0 - 70 deg relative to the normal. The radiation flux decreases sharply near the surface (>70 deg).

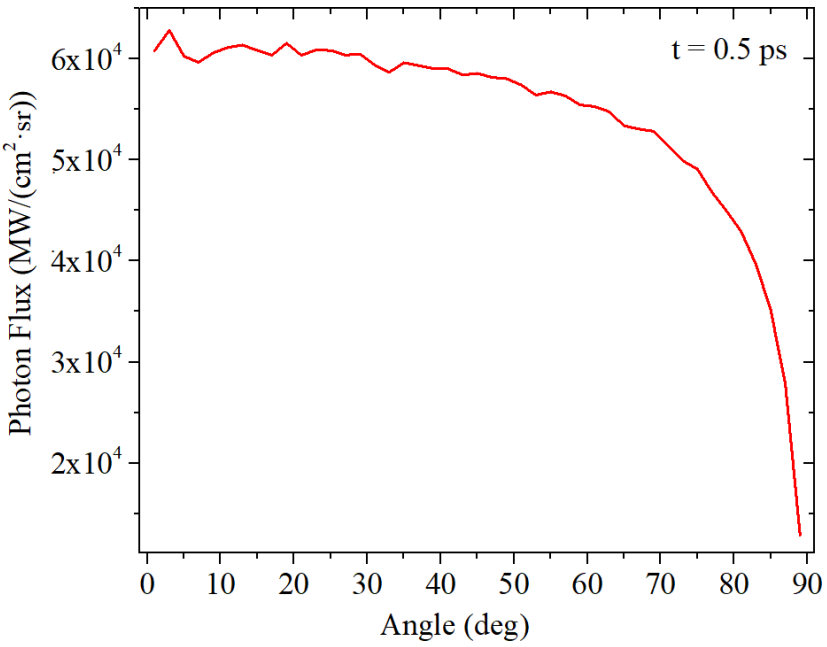

Fig. 36. Angular energy flux of photons emitted from a plasma into a vacuum at 0.5 ps.

2) Second case illustrates the mass density and temperature profiles of Ge plasma at time of 5 ps shown in Figs. 37 and 38, respectively.

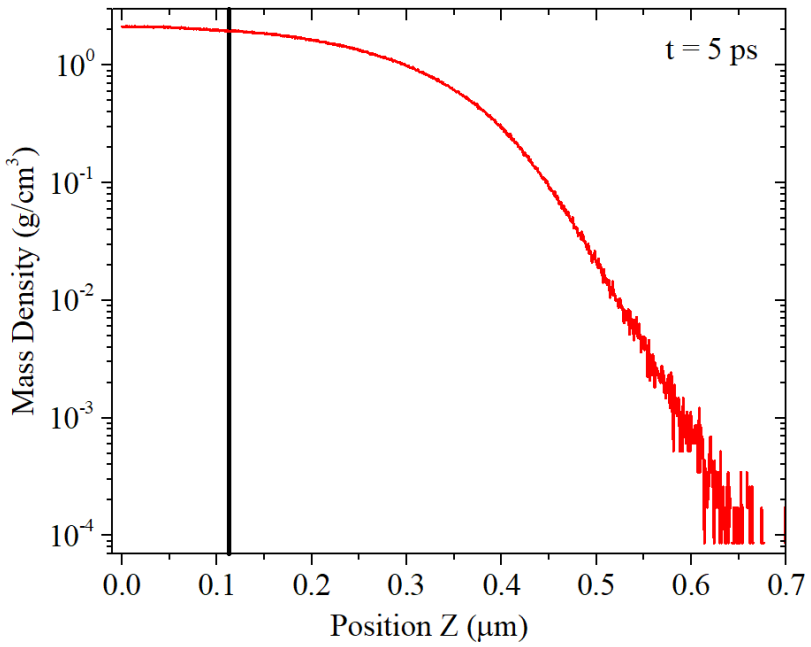

Fig. 37. Mass density of Ge plasma as a function of depth at 5 ps.

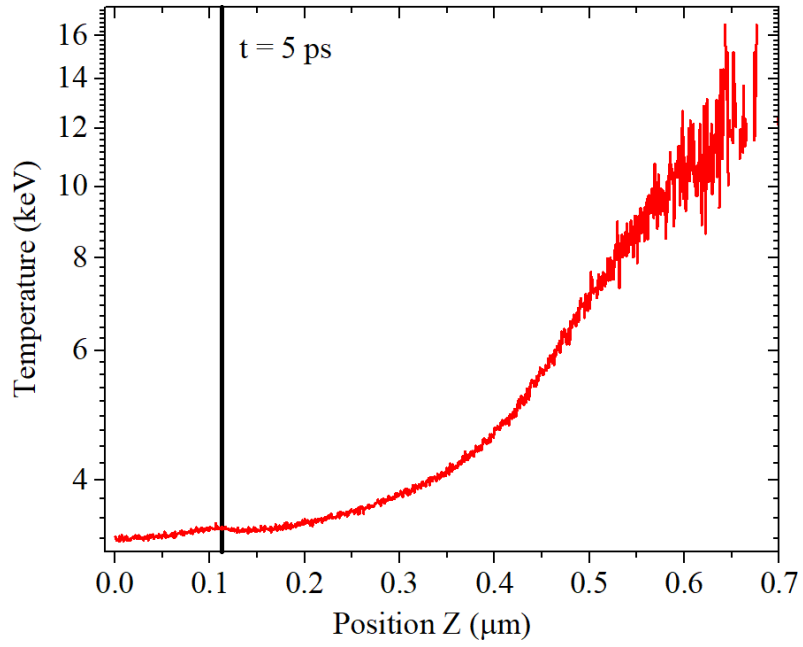

Fig. 38. Temperature of Ge plasma as a function of depth at 5 ps.

It is seen in Fig. 37 that the density of Ge plasma decreases to ~2 g/cm^3 in the original solid-state region (on the left side from black vertical line). The plasma expands up to ~0.7 μm into a vacuum with the mass density dropping to ~10^{-4} g/cm^3. The fluctuation of mass density is seen at the front of an expanding plasma due to a small number of Ge atoms in cells. Some cells do not contain yet any atoms. The temperature (Fig. 38) reaches ~3.4 keV below the original surface marked by a black vertical line and increases up to ~10 – 16 keV in the low-density plasma that expands into a vacuum.

The total emitted, absorbed, and escaped power and total rates of emission, absorption, and escape of photons in/from a plasma layer are given in Table 5.

Table 5. Total emitted, absorbed, and escaped power and total rates of emission, absorption, and escape of photons from Ge plasma.

Total Emission Power, *GW*	Total Absorbed Power, *GW*	Total Escaped Power into Vacuum, *GW*	Total Escaped Power into Bulk, *GW*	Average Energy of Emitted Photons, *keV*	Rate of Photon Emission, *photons/s*	Rate of Photon Absorption, *photons/s*	Rate of Photon Escape into Vacuum, *photons/s*	Rate of Photon Escape into Bulk, *photons/s*
14021613.6	7870399.7	3121665.4	3029548.5	3.45	$2.53 \cdot 10^{31}$	$1.4 \cdot 10^{31}$	$5.7 \cdot 10^{30}$	$5.6 \cdot 10^{30}$

The total rates of energy and photon number at 5 ps are increased significantly by many orders of magnitude as Ge plasma expands into a vacuum. The average energy of emitted photons increases to ~3.45 keV. Another feature is that the amount of escaped radiation from a plasma increases to ~44%. The photon emission into a vacuum and a bulk Ge material becomes comparable. The profiles of emitted and absorbed power density are shown in Fig. 39. It is seen that the absorption rate of radiation energy is higher near the front of expanding plasma. This correlates with the rates

of absorbed and emitted photon number density shown in Fig. 40. Thus, rates of absorbed energy density and absorbed photon number density at 5 ps are lower in the plasma region ~<0.45 μm.

Fig. 41 shows the spectral energy flux of photons emitted into a vacuum. The X-ray portion of spectrum extends to the region of hard X-rays (> 10 keV) with shorter wavelengths. The emission of X-rays in characteristic spectral lines can be seen.

Fig. 42 shows the angular distribution of photon energy flux emitted into a vacuum at 5 ps. It is similar in shape to that illustrated in Fig. 36 at 0.5 ps. However, the energy flux increases by four orders of magnitude.

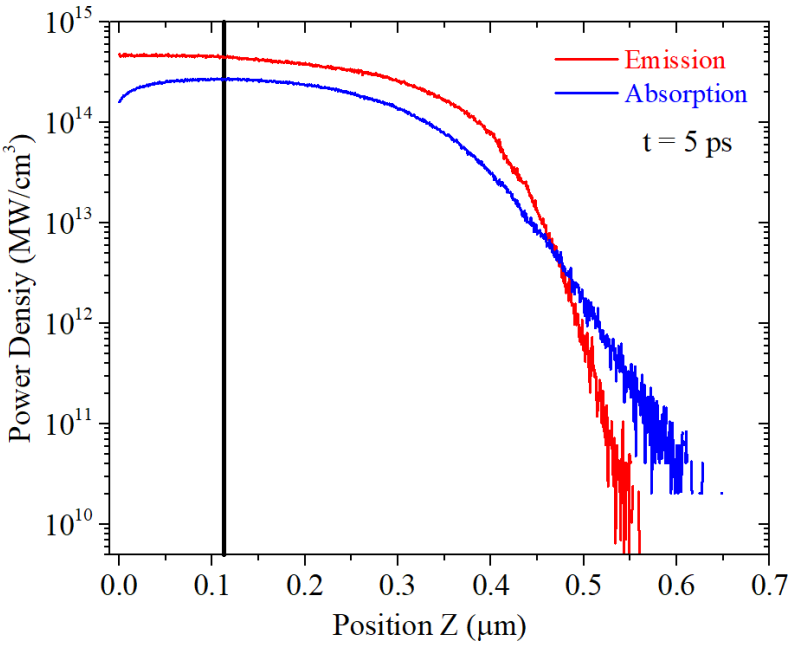

Fig. 39. Profiles of emitted and absorbed power density along the depth of a plasma at 5 ps.

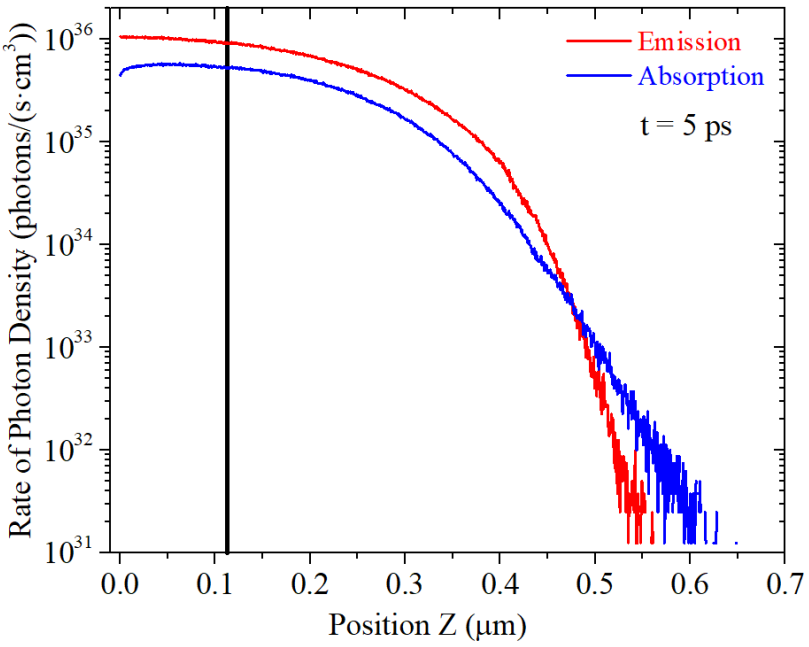

Fig. 40. Profiles of emitted and absorbed photons along the depth of a plasma at 5 ps.

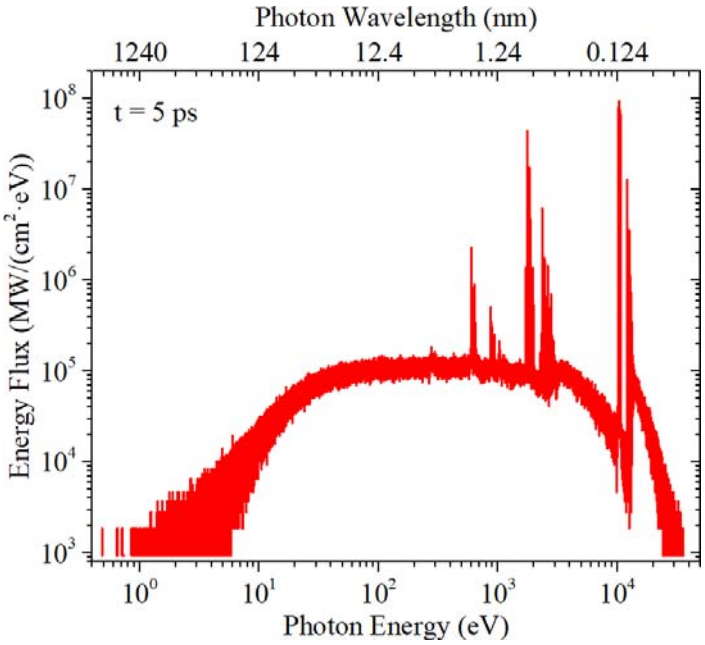

Fig. 41. Spectral energy flux of photons emitted from a plasma into a vacuum at 5 ps.

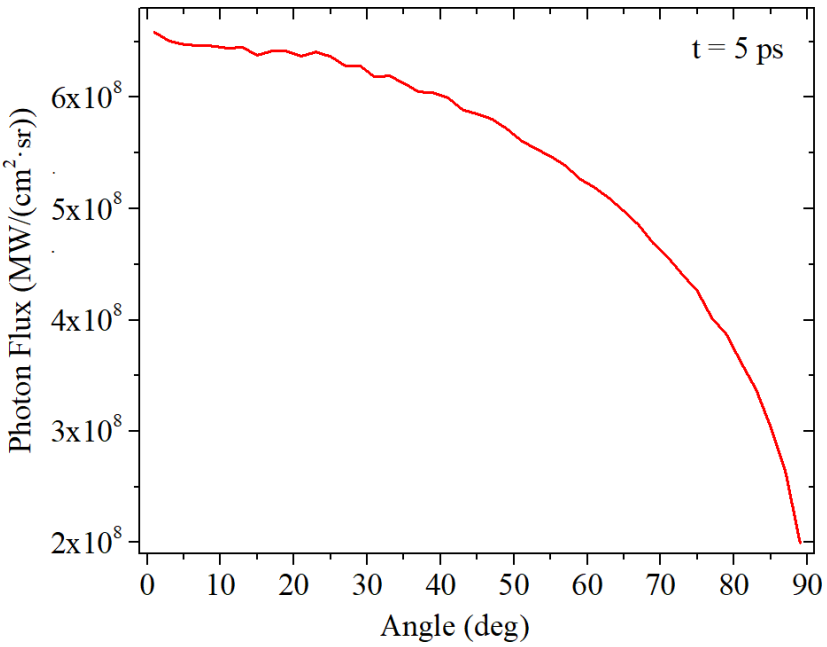

Fig. 42. Angular energy flux of photons emitted from a plasma into a vacuum at 5 ps.

3) Third case illustrates the mass density and temperature profiles of Ge plasma at time of 10 ps that are shown in Figs. 43 and 44, respectively. The plasma expands up to ~1.8 μm. The density drops to ~0.8 g/cm^3 behind the initial interface (black vertical line) between the solid Ge material and vacuum with the decrease in plasma density up to ~10^{-4} g/cm^3. The profile of temperature along the depth of plasma (Fig. 44) is slightly modified compared to that one shown in Fig. 38 at 5 ps. The temperature is slightly increased to ~4.4 keV below the original surface of Ge material and then increases up to ~12 – 18 keV in the low-density plasma that expanded into a vacuum.

The total power and total rates of emission, absorption, and escape of photons in/from a plasma layer are provided in Table 6. The average energy of emitted photons is increased to ~6.68 keV at 10 ps, so the total rates of energy and photon number are also slightly increased compared to those corresponding to 5 ps.

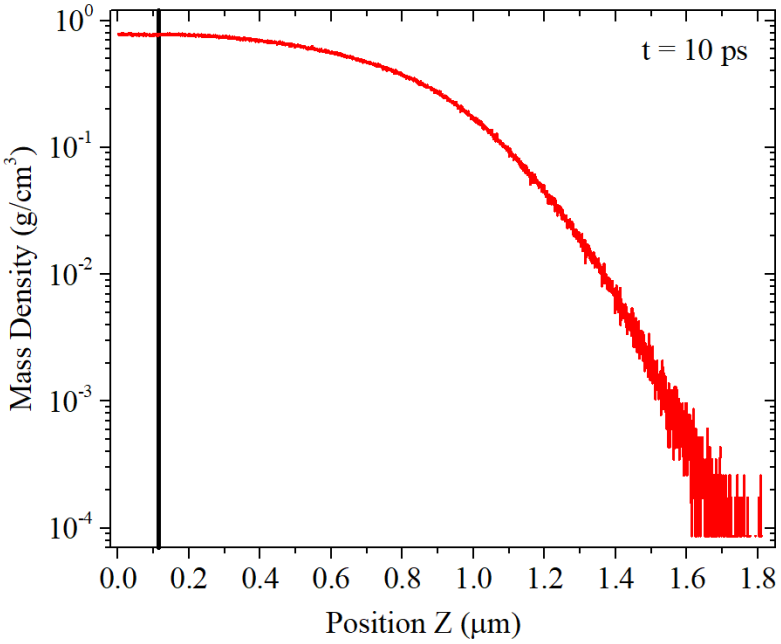

Fig. 43. Mass density of Ge plasma as a function of depth at 10 ps.

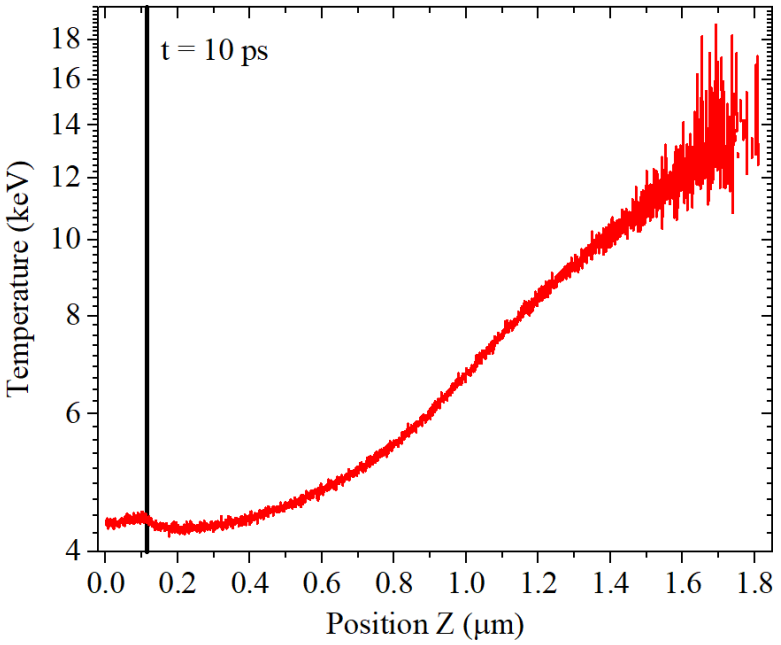

Fig. 44. Temperature of Ge plasma as a function of depth at 10 ps.

Table 6. Total power and total rates of emission, absorption, and escape of photons from Ge plasma.

Total Emission Power, *GW*	Total Absorbed Power, *GW*	Total Escaped Power into Vacuum, *GW*	Total Escaped Power into Bulk, *GW*	Average Energy of Emitted Photons, *keV*	Rate of Photon Emission, *photons/s*	Rate of Photon Absorption, *photons/s*	Rate of Photon Escape into Vacuum, *photons/s*	Rate of Photon Escape into Bulk, *photons/s*
18663018.4	10932958.2	3943300.8	3786759.3	6.68	$1.75 \cdot 10^{31}$	$9.53 \cdot 10^{30}$	$4.03 \cdot 10^{30}$	$3.92 \cdot 10^{30}$

The profiles of emitted and absorbed power density and the rates of absorbed and emitted photon number density are shown in Figs. 45 and 46. The behavior of emission and absorption rates is similar to that observed at 5 ps: less absorption of the emitted radiation in the bulk plasma region ~<1.2 μm and its higher absorption in the vicinity of the front of expanding plasma.

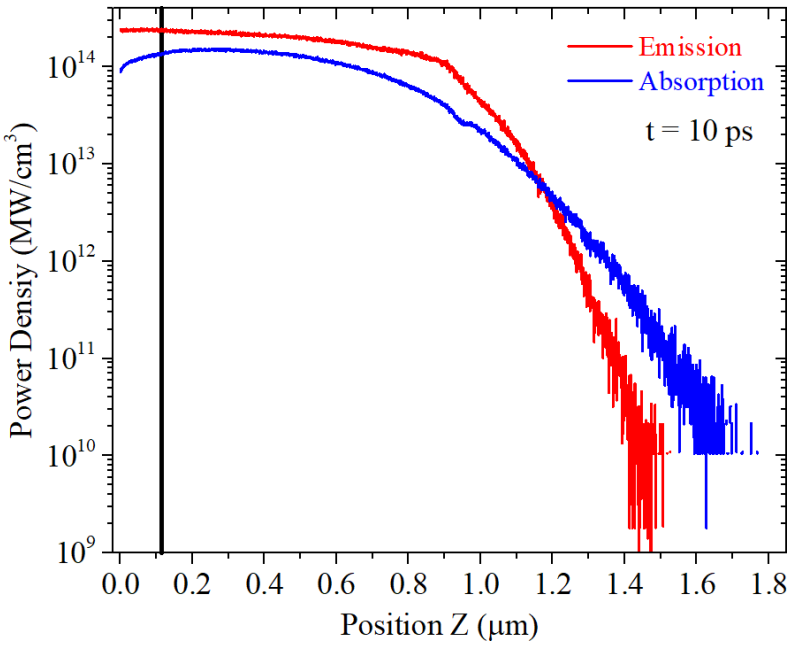

Fig. 45. Profiles of emitted and absorbed power density along the depth of a plasma at 10 ps.

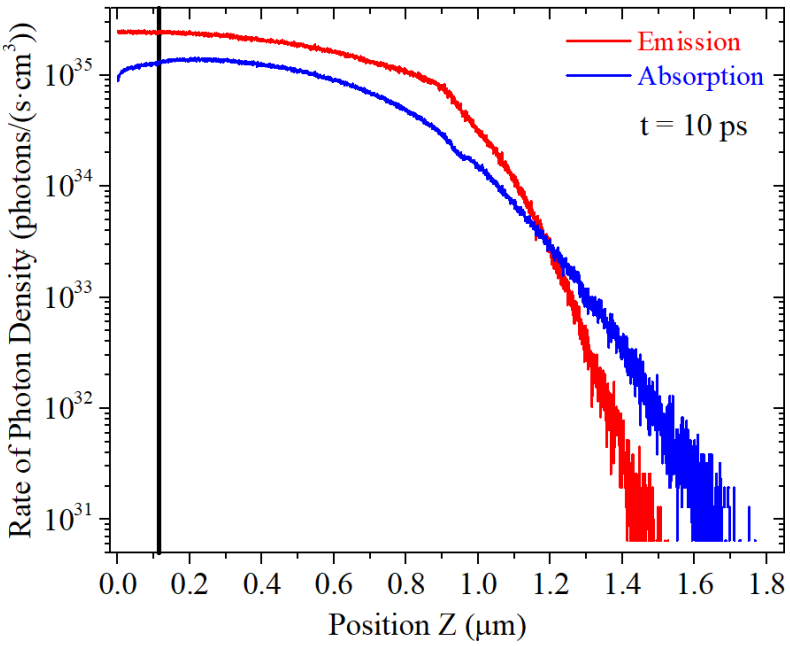

Fig. 46. Profiles of emitted and absorbed photons along the depth of a plasma at 10 ps.

The spectral energy flux of photons emitted into a vacuum at 10 ps is shown in Fig. 47. The energy spectrum of emitted photons is quite similar to that illustrated in Fig. 41 for 5 ps. X-ray portion of spectrum extends even more to the region of shorter wavelengths with the emission of X-rays in a number of characteristic spectral lines.

The angular distribution of photon energy flux emitted into a vacuum at 10 ps is shown in Fig. 48. It is quite similar in shape and magnitude to that illustrated in Fig. 42 for 5 ps.

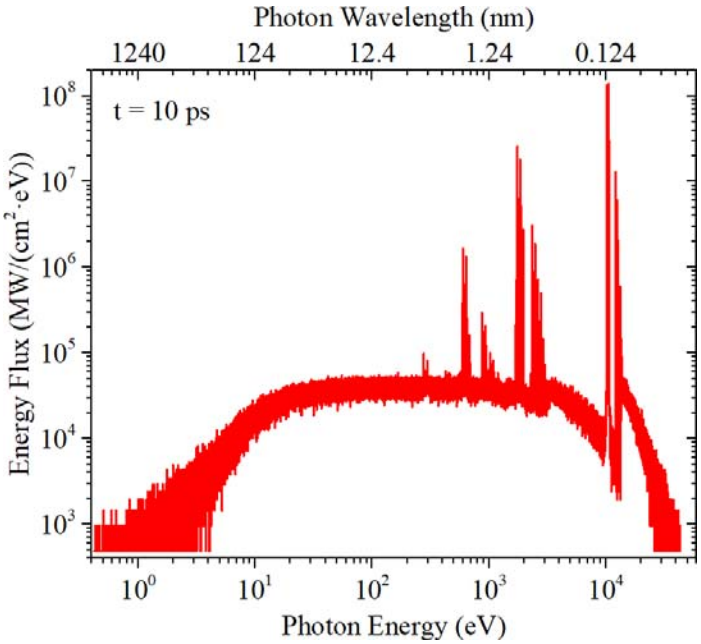

Fig. 47. Spectral energy flux of photons emitted from a plasma into a vacuum at 10 ps.

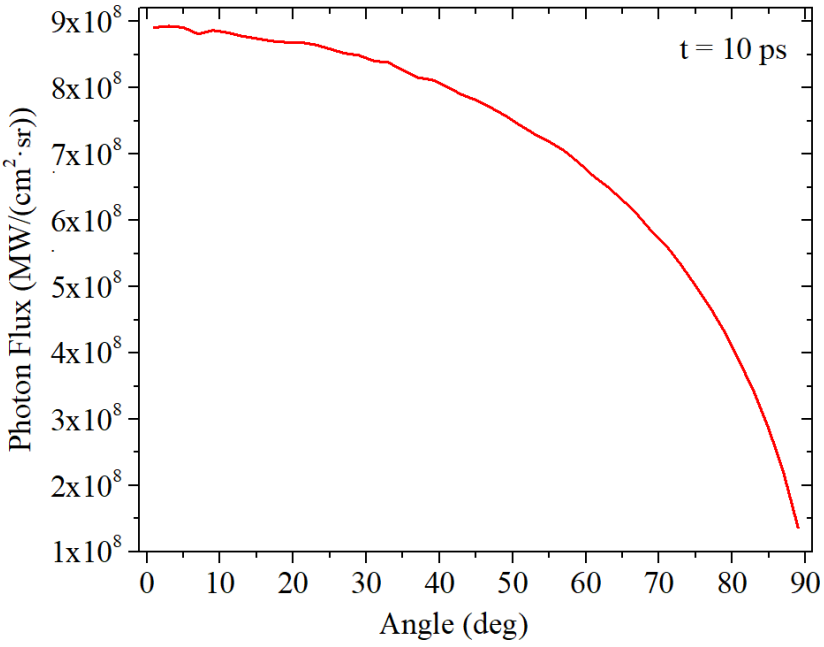

Fig. 48. Angular energy flux of photons emitted from a plasma into a vacuum at 10 ps.

2.8 Electrical and thermal conductivity of dense plasmas

The calculation of the ionization balance and electrical conductivity of WDPs with partially degenerated electrons and strong Coulomb couplings between ions is very important for the understanding of matter under extreme conditions such as the X-ray induced blow-off. In the nonideal dense plasma, the Coulomb interaction energy between the ions becomes comparable to the thermal energy and this ion coupling effect should be implemented into the models [8]. The theoretical approaches developed for dense cold solid and low density hot plasma are inapplicable. Therefore, many efforts have been focused on the development of comprehensive theoretical and computational models with the aim to provide the physical insight into transport properties of the warm and hot dense plasma states [48-53]. There are only a limited number of measurements of the electrical conductivities of WDPs that can serve as benchmark points for the computational models [54-57]. The experimental data were reviewed and compared to those calculated from the different theoretical models [58]. The WDP regime with a few of eV is the most difficult for studies. The compilation of the available experimental and computational data on the electrical conductivity of the most studied warm dense aluminum plasma is shown in Fig. 49. The electrical conductivity is shown as a function of mass density for temperature of 10,000 K (0.8617 eV). Fig. 49 clearly illustrates the difficulty for solving this problem. Large discrepancies are seen between the results obtained from various models and experiments. The discrepancy in electrical conductivity is around three orders of magnitude. The experimental points are also spread in a range of electrical conductivity values. Early Spitzer and Ziman models [59, 60] greatly overestimate and underestimate the electrical conductivity, respectively. With the availability of

measured data in late 90th, the computational models based on the different approximations were significantly improved to fit the experimental results [58]. Some of these models to list are the Kubo-Greenwood approach, the Lee-More model, the average-atom model, the linear mixture rule, and the linear response theory.

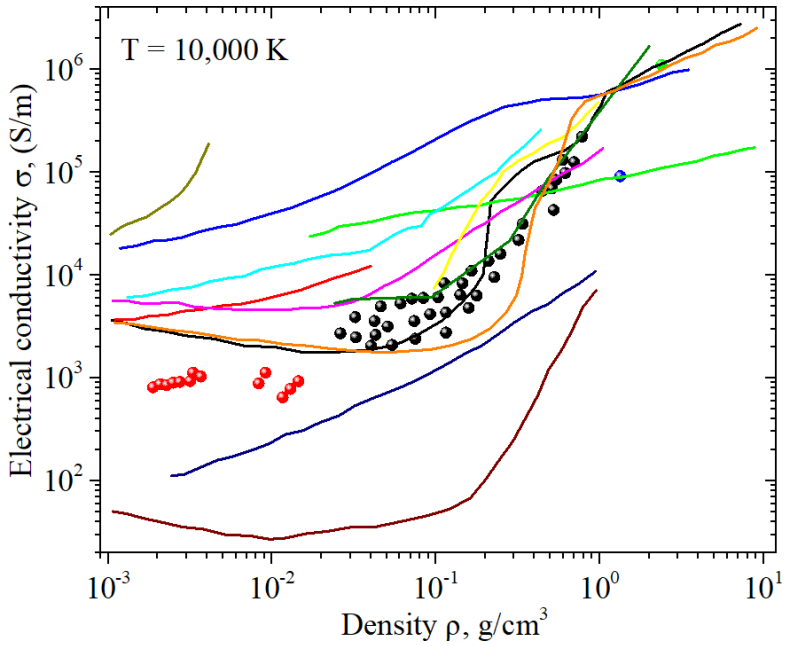

Fig. 49. Compilation of the available experimental and theoretical data on the electrical conductivity of warm dense aluminum plasma as a function of mass density at temperature of 10,000 K. Experiments: [56] (black spheres); [55] (red spheres); [54] (blue sphere); [57] (green sphere). Calculations: [51] (black line); [61] (red line); [62] (green line); [63] (blue line); [64] (cyan line); [65] (magenta line); [48] (yellow line); [59] (dark yellow line); [60] (navy line); [66] (wine line); [67] (olive line); [49] (orange line).

The electrical conductivity of WDP is calculated in this research using a linear mixture rule (LMR) [68] that treats various interactions among electrons, atoms, and ion species. The Coulomb coupling between ions is taken into account. The principal problem with high-fidelity calculation of the electrical conductivity is the need to determine the ion composition and free electron density in the WDP regime. The data on the ionization balance of WDP are calculated from the HFS-CRSS model and then used the LMR model. The LMR model is implemented in the REODP code and used to evaluate the electrical conductivity of Si and Ge WDPs. The foundations of LMR model, its implementation, benchmarks, and results on the electrical conductivity of Si and Ge WDPs are outlined below.

2.8.1 Linear Mixture Rule model

A linear mixture rule of additive collision frequencies for electron-ion and electron-neutral interactions can be formulated as [69]

$$\frac{1}{\sigma} = \frac{1}{\sigma_{ei}} + \frac{1}{\sigma_{en}}, \tag{48}$$

where σ is the total electrical conductivity, σ_{ei} and σ_{en} are the electrical conductivities associated with the electron-ion and electron-neutral collisions, respectively. These two electrical conductivities correspond to the limiting cases of complete (low-density and high-temperature plasma) and weak (high-density and low-temperature plasma) ionization and can be expressed using the exact formula. The different models are incorporated for the calculation of plasma ionization composition and electrical conductivity in the intermediate region between these two

limits. Equation (48) states that the total resistivity $\eta = 1/\sigma$ (reciprocal of total conductivity) of the plasma is simply the sum of resistivities $\eta_{ei} = 1/\sigma_{ei}$ and $\eta_{en} = 1/\sigma_{en}$ associated with charged and neutral particles, respectively. The SI unit of electrical conductivity is $\sigma\ [(s^3 \cdot A^2)/(kg \cdot m^3)] = [S/m] = [\Omega^{-1}m^{-1}]$, where $[S] = [(s^3 \cdot A^2)/(kg \cdot m^2)]$ is siemens and $[\Omega^{-1}m^{-1}]$ is reciprocal of Ohm meter.

2.8.1.1 The electron-neutral conductivity

The electron-neutral conductivity can be calculated as [50]

$$\sigma_{en} = \sqrt{\frac{\pi}{8m_e k_B T}} \frac{Z_{av} e^2}{\alpha_0 \bar{Q}_{en}}, \tag{49}$$

where

$k_B = 1.380649 \times 10^{-23}\ [J/K]$ is the Boltzmann constant $[J = (kg \cdot m^2)/s^2]$

$m_e = 9.10956 \times 10^{-31}\ [kg]$ is the electron's rest mass

$e = 1.602176634 \times 10^{-19}\ [C]$ is the electron charge $[C = A \cdot s]$

$T\ [K]$ is the temperature of plasma

$Z_{av}\ [dimensionless]$ is the average ionization state of the plasma that is calculated using the HFS-CRSS model (REODP code)

$\alpha_0\ [dimensionless]$ is the proportion of the neutral species to the total number of heavy particles that is calculated using the HFS-CRSS model (REODP code)

The average electron-neutral momentum transport cross section $\bar{Q}_{en}$ is calculated in the Born approximation as [70]

$$\bar{Q}_{en} = \frac{\pi^3(\alpha_D/(2r_0 a_B))^2}{A_\kappa^2 + 3B_\kappa kr_0 + 7.5C_\kappa(kr_0)^2 - 3.4D_\kappa(kr_0)^3 + 10.6668E_\kappa(kr_0)^4}, \quad (50)$$

where

$\kappa = 1/\lambda_D\ [1/m]$ is the inverse screening length with λ_D is the Debye length

$k = m_e\bar{v}_e/\hbar\ [kg \cdot m \cdot s^2/(s \cdot kg \cdot m^2 \cdot s)] = [1/m]$ is the electron wave number with $\bar{v}_e = \sqrt{3k_BT/m_e}\ \left[\sqrt{kg \cdot m^2/kg \cdot s^2}\right] = [m/s]$ is the average electron velocity and $\hbar = h/2\pi = 1.054571817 \times 10^{-34}\ [J \cdot s]$ is the reduced Planck's constant

$\alpha_D\ [m^3]$ is the dipole polarizability. The mean dipole polarizability of Si and Ge atoms are 37.4 $a.u.$ and 41.0 $a.u.$, where 1 $a.u. =\ 0.14818474$ Å$^3 = 0.14818474 \times\ 10^{-30}\ m^3$ [71]

$a_B = 4\pi\varepsilon_0\hbar^2/(m_e e^2) = 5.291772109\ \times\ 10^{-11}\ [m]$ is the Bohr radius

$r_0 = \sqrt[4]{\alpha_D a_B/(2Z^{1/3})}\ [m]$ is the cutoff radius

and

$$A_\kappa = 1 + 2\kappa r_0 + \frac{7}{\pi^2}(\kappa r_0)^2 + \frac{\pi}{7}(\kappa r_0)^3, \quad (51)$$

$$B_\kappa = exp(-18\kappa r_0), \quad (52)$$

$$C_\kappa = \frac{1 + 22\kappa r_0 - 11.3(\kappa r_0)^2 + 33(\kappa r_0)^4}{1 + 6\kappa r_0 + 4.7(\kappa r_0)^2 + 2(\kappa r_0)^4}, \quad (53)$$

$$D_\kappa = \frac{1 + 28\kappa r_0 + 13.8(\kappa r_0)^2 + 3.2(\kappa r_0)^3}{1 + 8\kappa r_0 + 10(\kappa r_0)^2 + (\kappa r_0)^3}, \quad (54)$$

$$E_\kappa = 1 + 0.1\kappa r_0 + 0.3665(\kappa r_0)^2. \quad (55)$$

The Debye length λ_D is expressed as

$$\frac{1}{\lambda_D^2} = \frac{1}{\lambda_{D_e}^2} + \frac{1}{\lambda_{D_i}^2} = \frac{n_e e^2}{\varepsilon_0 k_B T_e} + \sum_{j=0}^{Z} \frac{n_j Z_j^2 e^2}{\varepsilon_0 k_B T_i}, \tag{56}$$

where n_e $[m^{-3}]$ is the number density of electrons, n_j $[m^{-3}]$ is the number density of j-th ion species, Z_j is the number of unit charges for j-th ion species, j is running from $j = 0, 1, \ldots Z$ where $j = 0$ correcponds to a neutral atom, $j = 1$ corresponds to a singly ionized ion, etc., and $j = Z$ corresponds to a completely ionized atom (nucleus), T_e $[K]$ is the electron temperature, T_i $[K]$ is the ion temperature, and ε_0 is the permittivity of vacuum given by

$$\varepsilon_0 = 8.8541878 \times 10^{-12} \left[\frac{F}{m} = \frac{s^2 \cdot C^2}{m^2 \cdot kg} \cdot \frac{1}{m} = \frac{s^2 \cdot C^2}{m^3 \cdot kg}\right]. \tag{57}$$

The quasi-neutrality condition is

$$n_e \cong \sum_{j=0}^{Z} n_j Z_j. \tag{58}$$

In the case when $T_e = T_i = T$ $[K]$, the Debye length can be expressed as

$$\lambda_D = \sqrt{\frac{\varepsilon_0 k_B T}{n_e e^2 \left(1 + Z_{eff}\right)}}, \tag{59}$$

where the effective charge

$$Z_{eff} = \frac{\sum_{j=0}^{Z} n_j Z_j^2}{\sum_{j=0}^{Z} n_j Z_j} = \frac{\sum_{j=0}^{Z} n_j Z_j^2}{n_e}. \quad (60)$$

The average charge is

$$Z_{av} = \frac{n_e}{\sum_{j=0}^{Z} n_j} = \frac{n_e}{n_a}, \quad (61)$$

where n_a is the number density of heavy particles.

2.8.1.2 The electron-ion conductivity

The electron-ion conductivity can be given by the Spitzer-Härm expression for fully ionized plasma taking into account the electron-electron collisions [59] that was modified by Zollweg and Liebermann [48] as

$$\sigma_{ei} = \frac{T^{\frac{3}{2}}}{38 Z_{av}} \frac{\gamma_e(Z_{av})}{\ln \Lambda}, \quad (62)$$

where T $[K]$ is plasma temperature in Kelvin units and factor $\gamma_e(Z_{av})$ $[dimensionless]$ takes into account the electron-electron scattering and can be expressed as [72]

$$\gamma_e(Z_{av}) = \frac{3\pi}{32}\left(1 + \frac{153{Z_{av}}^2 + 509Z_{av}}{64{Z_{av}}^2 + 345Z_{av} + 288}\right). \quad (63)$$

The Coulomb logarithm $\ln\Lambda$ $[dimensionless]$ represents the classical collision cross-section integral for electron interaction with ions of charge Z_{av} and can be evaluated as [53]

$$\ln\Lambda = exp\left(\frac{3}{2\Lambda_s}\right)E_1\left(\frac{3}{2\Lambda_s}\right), \quad (64)$$

where $\Lambda_s = r_s/\bar{b}_0$ with $r_s = a_z$ is a characteristic screening distance and E_1 is the exponential integral given by

$$E_1(x) = \int_x^\infty \frac{e^{-t}}{t}dt. \quad (65)$$

The ion sphere radius a_z $[m]$ for the charge state z of the ion is given by

$$a_z = \left(\frac{3(z+1)}{4\pi n_a(1+Z_{av})}\right)^{1/3}. \quad (66)$$

It is seen that the Coulomb logarithm is affected by the ionization balance. The average impact parameter $\bar{b}_0$ $[m]$ can be expressed as

$$\bar{b}_0 = \frac{Ze^2}{12\pi\varepsilon_0 k_B T}. \quad (67)$$

The following approximation for the Coulomb logarithm with a maximum error less than 5% can be used

$$\ln \Lambda \approx \frac{1.0 + ln(1 + 0.1377\Lambda_s)}{1.0 + \frac{1.5}{\Lambda_s}}. \tag{68}$$

2.8.1.3 Ionization potential depression model

The model of ionization potential depression (IPD) (continuum lowering) described in the 2020 Annual Report was slightly modified to account for the fact that the different z-fold ions have the different size of ion sphere. The lowering of ionization energies of z-fold ion is expressed as

$$\Delta I_z = \frac{(z+1)e^2}{4\pi\varepsilon_0 R_z}, \tag{69}$$

where $z = 0, 1, \ldots Z$ is the charge state of the ion with $z = 0$ corresponding to a neutral atom and R_z is the characteristic radius expressed as

$$R_z = \sqrt{\lambda_D^2 + \left(\frac{2}{3}a_z\right)^2}, \tag{70}$$

where λ_D is the Debye length and a_z is the ion-sphere radius.

2.8.2 Validations of the LMR model

The electrical conductivity strongly depends on the ionization degree of nonideal plasma. Therefore, the calculation of the electrical conductivity using the LMR model requires the knowledge of number density of different ionic species and free electrons for a wide range of plasma densities and temperatures. These are calculated by solving the system of kinetic equations within the HFS-CRSS model implemented in the REODP code. The average charge (mean ionization state or ionization degree) of Al plasma is shown in Fig. 50 as a function of plasma density at temperature of 10000 K and REODP results are compared to the measured [55] and calculated [65] data available in the literature. It is seen that the data on ionization degree of plasma measured at 10000, 12000, and 14000 K are confined between the Ebeling and REODP curves calculated at 10000 and 30000 K. The values of calculated average charge at 10000 K are lower than the measured ones. Although there are some discrepancies, the REODP results are consistent with Ebeling's results in the low-density region ($< \sim 0.1 - 0.2\ g/cm^3$) where the thermal ionization dominates. The ionization degree decreases with density increase due to the contribution of recombination. The average charge of plasma increases abruptly due to the pressure ionization dominating in the density range of $\sim 0.1 - 1\ g/cm^3$. The ionization degree predicted by Ebeling *et al.* is ~2 at $\rho = 1\ g/cm^3$, while the REODP result is 3 that is in agreement with previously published data [49, 51]. The stepwise shape of REODP profiles in a high-density region reveals the abrupt transitions from bound to free electronic states. For the case with 10000 K, the outer 3p electron of aluminum atoms is density ionized (ionization potential is 5.98 eV) at $\sim 0.2\ g/cm^3$ with the average charge state of plasma remaining at 1 up to density of $\sim 0.63\ g/cm^3$. With further

increase of density the two 3s electrons are also density ionized (ionization potentials are 18.82 eV and 28.44 eV, respectively) and the ionization degree of plasma becomes 3. The weighting factors [53] or fluctuations in the free electron density [73] are usually used to approximate the average charge state as a continuous function, thus providing smooth transition between bound and free states. This option is yet to be implemented in the REODP's IPD model.

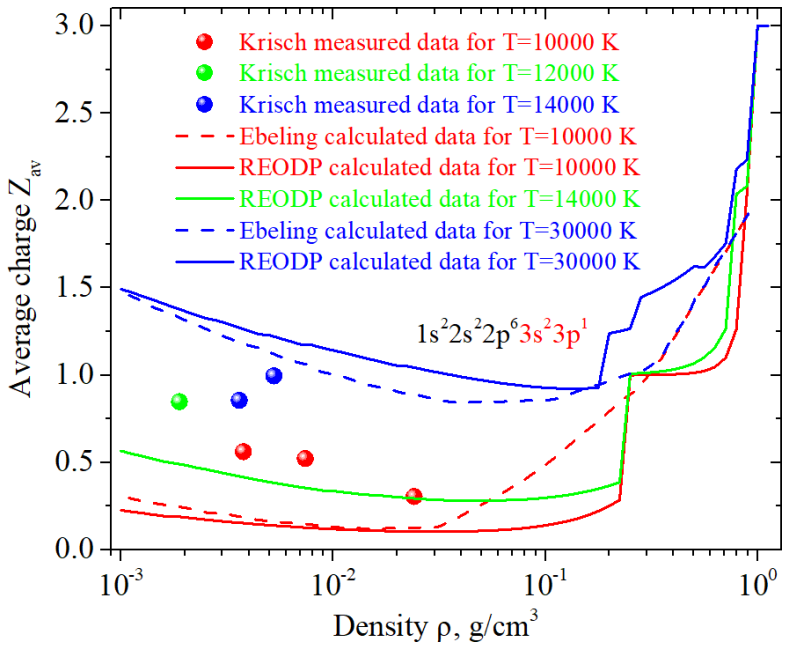

Fig. 50. REODP calculated average charge in Al plasma at 10000 K as a function of mass density compared to measured and calculated literature data.

In Fig. 51, the REODP calculated electrical conductivity of Al plasma as a function of density at temperature of 10000 K (red curve) is compared with the measured and calculated results. The experimental data points by Krisch *et al.*, DeSilva *et al.*, Mostovych *et al.* and Benage *et al.* [54-57] are the same as those in Fig. 49. The most accurate, up-to-date theoretical results by

Kim *et al.* and Fu *et al.* [49, 51] from Fig. 49 are also shown as black and green curves. As can be seen in Fig. 51, the REODP profile is in reasonable agreement with the measured data and other computational results. The experimental points by Krisch *et al.* [55] are located below all the computational curves in the low-density range. The electrical conductivity decreases with increasing density and reaches a minimum at $\sim 0.025\ g/cm^3$. And then, it increases with further density increase due to the nonmetal to metal transition. The sharp edges in the REODP's conductivity are due to the abrupt density-induced ionization transitions.

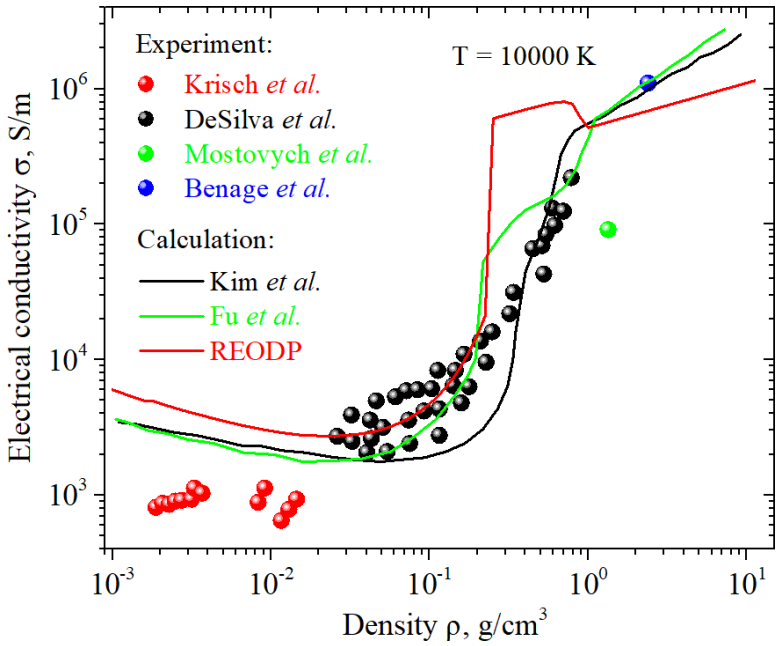

Fig. 51. Electrical conductivity of aluminum plasma as a function of mass density at temperature of 10000 K, compared with other experimental and computational results.

Experimental data of DeSilva *et al.* [56] on the electrical conductivity of iron are compared in Fig. 52 with the present REODP results and the theoretical results of Kuhlbrodt *et al.* [74]

calculated within the linear response theory for plasma temperature of 10000 K. The REODP curve is in reasonable agreement within the spread of experimental data points. The theoretical data calculated from the linear response theory are positioned consistently lower than the measured conductivities.

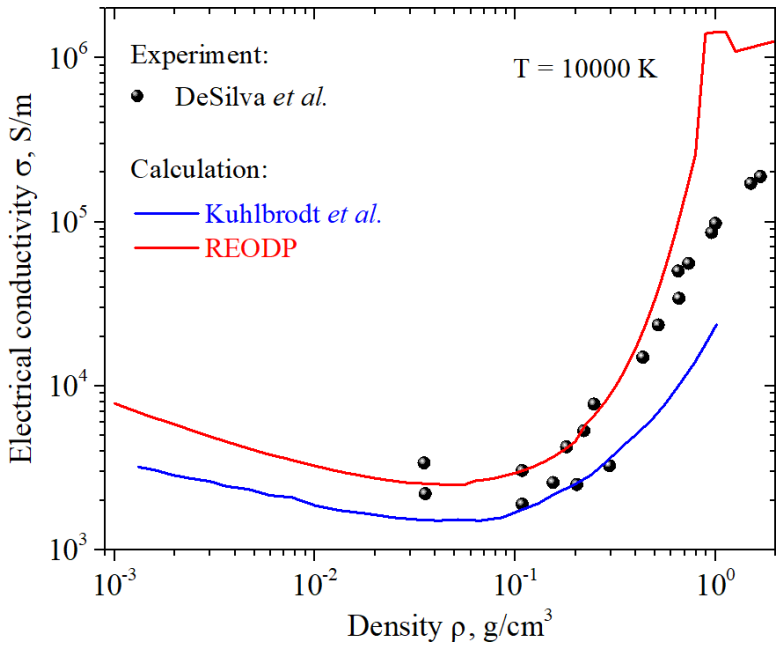

Fig. 52. Electrical conductivity of iron plasma as function of mass density for 10000 K. The REODP calculated conductivity is compared with experimental points of DeSilva *et al.* [56] and theoretical curve of Kuhlbrodt *et al.* [74].

2.8.3 Average charge state and electrical conductivity of Si and Ge plasmas

The average charge (ionization degree) and electrical conductivity of Si and Ge plasmas are calculated using the LMR model in a wide range of densities for temperatures of 1-3 eV. The

ionization degree Z_{av} represents the average number of free electrons generated in a plasma per heavy particle. The average charge as a function of density is shown in Fig. 53 for Si and in Fig 54 for Ge plasmas at temperature of 10000, 20000 and 30000 K. The behavior of ionization degree in density-temperature space is very similar for both Si and Ge plasmas. In the low-density region, Z_{av} decreases with increasing density. It is slightly greater for Ge plasma. Approaching solid state density, Z_{av} increases rapidly toward a value of 4 due to the lowering of ionization potential of Si and Ge atoms known as pressure ionization. The minimum of Z_{av} is located at $\sim 0.1\ g/cm^3$ for Si plasma and $\sim 0.2\ g/cm^3$ for Ge plasma. It is seen that at solid density four electrons from the outer s- and p-shells of Si and Ge atoms are ionized. The Si and Ge ions with a higher charge than 4 do not occur in a plasma at temperatures of 1–3 eV. At any fixed value of density, Z_{av} increases with increasing temperature at densities lower than $\sim 0.1\ g/cm^3$.

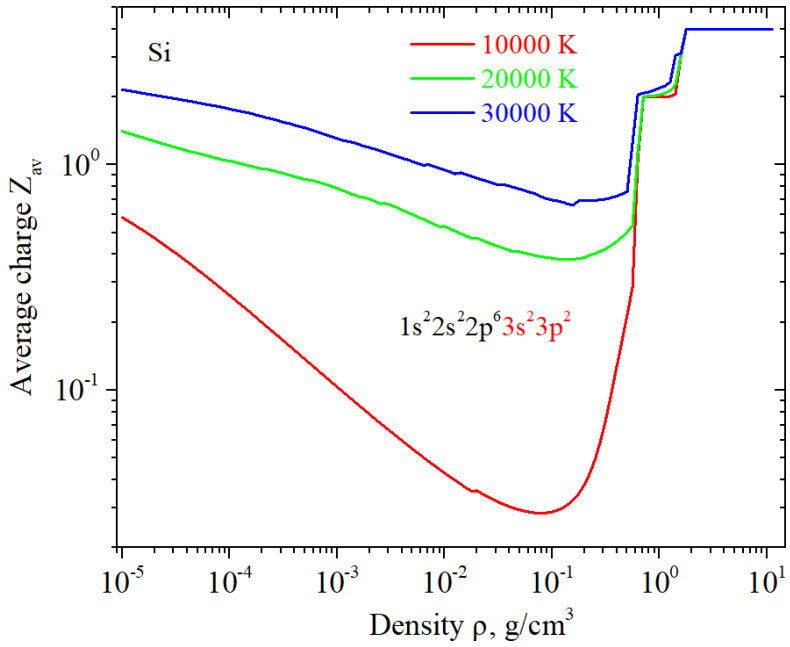

Fig. 53. The ionization degree of Si plasma as a function of mass density for temperature of 10000, 20000 and 30000 K.

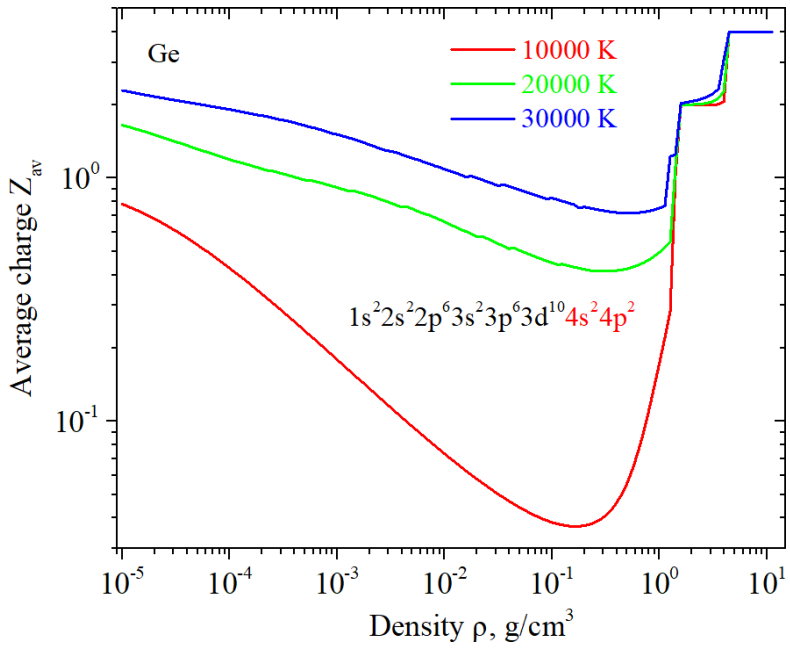

Fig. 54. The ionization degree of Ge plasma as a function of mass density for temperature of 10000, 20000 and 30000 K.

The average charge Z_{av}~2 (plateau) at ~0.6 g/cm^3 for Si and ~1.5 g/cm^3 for Ge corresponds to the plasma state with two electrons ionized from p-shell. Z_{av}~4 is constant when the density becomes higher than ~2 g/cm^3 for Si plasma and ~4 g/cm^3 for Ge plasma.

The electrical conductivity for Si and Ge plasma are shown in Figs. 55 and 56 as a function of mass density for temperature of 10000, 20000 and 30000 K. It is seen that the electrical conductivity decreases with increasing density in low-density region, passes through a minimum, and then shows a sharp increase due to the pressure ionization. The behavior in low-density region is governed by the decreasing fraction of free electrons due to the recombination and their decreasing mobility due to the collisions with neutral atoms.

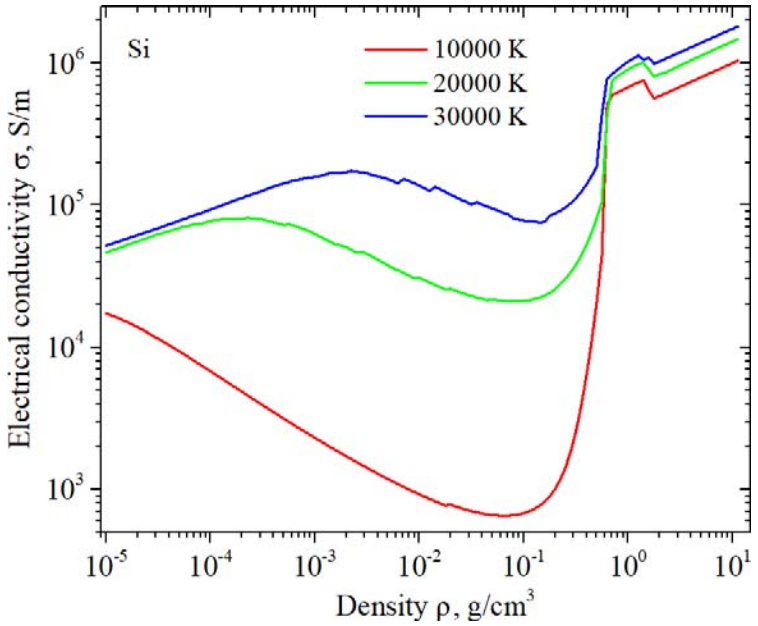

Fig. 55. The electrical conductivity of Si plasma as a function of mass density for temperature of 10000, 20000 and 30000 K.

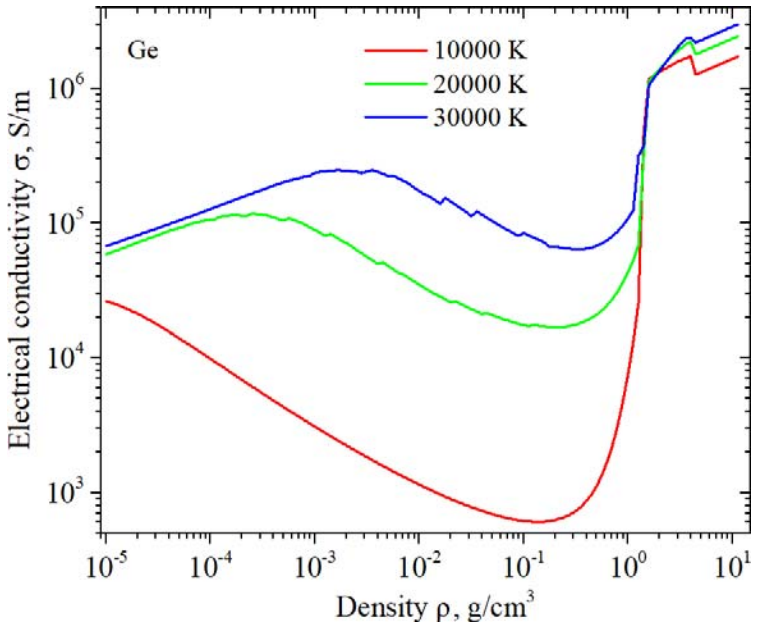

Fig. 56. The electrical conductivity of Ge plasma as a function of mass density for temperature of 10000, 20000 and 30000 K.

At higher temperatures, the population of neutral atoms, the role of recombination, and the electron-neutral collisions decrease as a result of higher thermal effects leading to flattening a minimum. The position of minimum is shifted towards higher density with increasing temperature. It is seen that the electrical conductivity increases with increasing temperature. Overall, it is slightly higher for Ge plasma.

Published papers and presentations acknowledging support from HDTRA1-18-1-0025 and HDTRA1-19-1-0019 grants

Peer-reviewed papers

1. Miloshevsky G. *PIC Modeling of OMEGA Experiments on Ablation of Plasmas*. IEEE Transactions on Plasma Science, Vol. 51, 2023, 980 - 986 https://doi.org/10.1109/TPS.2022.3220184
2. Miloshevsky G. *Ultrafast laser matter interactions: modelling approaches, challenges, and prospects*. Modelling and Simulation in Materials Science and Engineering. Vol. 30, No. 8, 2022, pp. 083001. https://doi.org/10.1088/1361-651X/ac8abc
3. Karasiev V. V., S. Hu, N. R. Shaffer and G. Miloshevsky. *A First-Principles Study of L-Shell Iron and Chromium Opacity at Stellar Interior Conditions*. Physical Review E, Vol. 106, 2022, 065202. https://doi.org/10.1103/PhysRevE.106.065202

Book chapter

1. Harilal S. S., P. K. Diwakar and G. Miloshevsky. *Ultrafast and Filament LIBS* in Laser-induced Breakdown Spectroscopy, edited by J. P. Singh and S. N. Thakur, Elsevier, Amsterdam, 2020, Chapter 6, pp. 139-166. https://www.elsevier.com/books/laser-induced-breakdown-spectroscopy/singh/978-0-12-818829-3

MS thesis

1. Derek J. Schauss, *Equations of State for Warm Dense Carbon from Quantum ESPRESSO*, Master of Science Thesis, Mechanical and Nuclear Engineering, Virginia Commonwealth University, Richmond, VA, May 4, 2021. Advisor: Dr. Gennady Miloshevsky. https://scholarscompass.vcu.edu/etd/6702/
2. Harrison C. Wenzel, *Generation of Warm Dense Plasma on Solar Panel Infrastructure in Exo-Atmospheric Conditions*, Master of Science Thesis, Mechanical and Nuclear Engineering, Virginia Commonwealth University, Richmond, VA, April 24, 2020. Advisor: Dr. Gennady Miloshevsky. https://doi.org/10.25772/AYXS-XV89
3. Myles Fogleman, *Cold X-ray Effects on Satellite Solar Panels in Orbit*, Master of Science Thesis, Mechanical and Nuclear Engineering, Virginia Commonwealth University, Richmond, VA, December 6, 2019. Advisor: Dr. Gennady Miloshevsky. https://doi.org/10.25772/BZXN-MC82

Conference/Technical review oral presentations

1. Abouhussien, Y., M. Polek, G. Miloshevsky, F. Beg, S. Harilal. *Investigation of Laser Produced Plasma Expansion in Ambient Gases for Aluminum and Silicon*. The 50-th IEEE International Conference on Plasma Science (ICOPS), Santa Fe, NM, May 21-25, 2023, Session: Laser Produced Plasmas, O-2.4.2. https://www.eventclass.org/contxt_icops2023/scientific/online-program/session?s=O-2.4#e57

2. Miloshevsky G. *Particle-In-Cell simulation of silicon laser ablation and formation of over-dense plasma*. The 64th Annual Meeting of the APS Division of Plasma Physics, Session YO06: Short-pulse Laser-plasma Interactions/Nonlinear Optics of Plasma, Spokane, WA, October 17-22, 2022. https://meetings.aps.org/Meeting/DPP22/Session/YO06.7

3. Karasiev V. V., S. Hu, N. R. Shaffer and G. Miloshevsky. *A First-Principles Study of L-Shell Iron and Chromium Opacity at Stellar Interior Conditions.* The 64th Annual Meeting of the APS Division of Plasma Physics, Session JO06: HEDP Laboratory Astrophysics on Z, Spokane, WA, October 17-22, 2022. https://meetings.aps.org/Meeting/DPP22/Session/JO06.12

4. Miloshevsky G. *PIC Modeling of OMEGA Experiments on Ablation of Plasmas*. The 49-th IEEE International Conference on Plasma Science (ICOPS), Sheraton Grand Seattle, Seattle, WA, May 22-26, 2022, Session: Laser Produced Plasmas, AO 2.3-4. https://ieeexplore.ieee.org/document/9813047

5. Abouhussien, Y. and G. Miloshevsky. *OpenFOAM CFD Modeling of Laser Ablated Plasma Plumes*. The 49-th IEEE International Conference on Plasma Science (ICOPS), Sheraton Grand Seattle, Seattle, WA, May 22-26, 2022, Session: Laser Produced Plasmas, AO 2.3-6. https://ieeexplore.ieee.org/document/9813123

6. Miloshevsky G. *Composition and Optical Properties of Warm Dense Germanium Plasma*. The 48-th Virtual IEEE International Conference on Plasma Science (ICOPS), September 12-16, 2021, Oral talk 1O-C-02. https://ieeexplore.ieee.org/document/9588553

7. Schauss, D. and G. Miloshevsky. *Thermodynamic and Optical Properties of Warm Dense Carbon*. American Physical Society Virtual Meeting, Session J23: Materials in Extremes:

Carbon and Related Materials, March 15-19, 2021. https://meetings.aps.org/Meeting/MAR21/Session/J23.7

8. Miloshevsky G. *Spatiotemporal Evolution of High-Density Surface Plasmas Produced by Prompt X-rays.* 2019 DTRA Radiation Effects Technical Review, Ballston (Arlington), VA, June 25, 2019.
9. Fogleman M., C. Wenzel, and G. Miloshevsky. *Dynamics and Properties of High-Density Surface Plasmas Induced by Cold X-rays*. The 10-th International Workshop on Warm Dense Matter (WDM 2019), Travemünde, Germany, May 5 - 9, 2019.
10. Dressman P. and G. Miloshevsky. *Soft X-ray Depth-Dose Profiles in Satellite Surface Materials*. The 45th IEEE International Conference on Plasma Science (ICOPS). Denver, CO, June 24-28, 2018. https://ieeexplore.ieee.org/document/9575763

Poster presentations

1. Wenzel C. and G. Miloshevsky. *Spatio-Temporal Evolution of Warm Dense Plasmas: Molecular Dynamics Modeling.* Abstracts of the 23rd Annual Graduate Research Symposium, Virginia Commonwealth University, Richmond, VA, April 21, 2020, P70. https://scholarscompass.vcu.edu/gradposters/70
2. Wenzel C. and G. Miloshevsky. *Cold X-ray Energy Deposition and Backscattering From Active Solar Cell Elements.* 2019 DTRA Radiation Effects Technical Review, Ballston (Arlington), VA, June 25, 2019.

3. Fogleman M. and G. Miloshevsky. *Power Density Distributions Produced by Cold X-rays in Multi-Layer Slab Targets.* 2019 DTRA Radiation Effects Technical Review, Ballston (Arlington), VA, June 25, 2019.
4. Fogleman M. and G. Miloshevsky. *Energy Deposition Distributions Produced by Cold X-rays in Multi-Layer Slab Targets*. Abstracts of the 22nd Annual Graduate Research Symposium, Virginia Commonwealth University, Richmond, VA, April 23, 2019, P13.
5. Wenzel C. and G. Miloshevsky. *Spectral Energy Distributions of Backscattered Photons and Electrons from Multi-Layer Slab Targets*. Abstracts of the 22nd Annual Graduate Research Symposium, Virginia Commonwealth University, Richmond, VA, April 23, 2019, P23.

Supported students

Table with the names and start/end dates for ten students who were paid on these grants

Name	Position	Start Date	End Date	Graduated, Degree
Phillip Dressman	PhD Student	03/23/2018	12/24/2018	N/A
Joshua Rudolph	PhD Student	03/23/2018	12/24/2018	N/A
Myles Fogleman	MS Student	03/25/2019	12/24/2019	MS thesis, December 2019
Harrison Wenzel	MS Student	03/25/2019	05/09/2020	MS thesis, April 2020
Derek Schauss	MS Student	08/10/2020	12/24/2020	MS thesis, May 2021
Jesse McFall	Undergrad	09/25/2021	02/09/2022	N/A
Amber Wren Walton	Undergrad	09/10/2021	06/24/2022	N/A
Youssef Abouhussien	PhD Student	05/10/2022	12/24/2022	Continuing
Juniper C. Savchick	PhD Student	05/10/2022	12/24/2022	Continuing
Cheng Zhang	PhD Student	07/10/2022	05/09/2023	Continuing

Executive summary of accomplished work

The transport of cold X-rays (~1 keV) in layers of solar cell materials and their energy deposition and redistribution by secondary radiation, material disintegration, heating, melting and vaporization, formation of blow-off and its spatiotemporal evolution, atomic and optical properties of WDPs and HDPs, radiative transfer and energy redistribution in WDPs/HDPs expanding into vacuum, and their electrical properties are studied. In order to accomplish this research the different models are coupled and integrated for transport and energy deposition by X-rays in materials, molecular dynamics of blow-off and plasma expansion into vacuum, radiative transfer and energy redistribution in plasmas based on pre-calculated dataset of optical properties, and electrical conductivity of WDPs. The modeling results provide valuable insights into the physical mechanisms of blackbody X-ray interactions with materials of solar arrays, formation of warm/hot dense surface plasmas, and their optical and electrical properties.

The MC modeling of X-ray transport in stacked layers of solar cell materials predicts that blackbody X-rays with thermal energy >~1 keV deposit the energy and power into an active semiconductor of solar cells resulting in its damage. The layers of AR and CMX cover materials are not thick enough to shield a GaInP/GaAs/Ge semiconductor element from cold X-rays. The layer of unshielded Ge semiconductor in gaps between solar cells can be directly affected and damaged by cold X-rays at incidence angles in the range from $>\sim 5^0$ to $<\sim 80^0$ with respect to the normal to the surface of solar cell. The higher energy is deposited in the near-surface region of Ge material at small angles of X-ray incidence. The power density in Ge material increases with increasing the thermal energy of a fireball. The backscattering yield of photons and electrons is

found to be negligible for 0.1 keV, 1.0 keV, and 10 keV blackbody X-rays meaning that X-ray energy is entirely deposited into solar cell slabs.

The disintegration of Ge material and formation of WDP phase induced by absorption of X-rays are observed during the time interval less than 0.5 ps due to the development of large positive and negative stresses resulting in melting of Ge material, formation of WDP, and its subsequent expansion into vacuum. The decompression (distress) occurs locally at some tiny points during the initial stage of relaxation of the solid-state Ge material after the absorption of X-rays. At later times from ~2 ps to ~4 ps, the highest value of positive stresses reaches ~168 Mbar in the HDP region below the original surface of Ge material. The transient WDP state (<100 eV and ~10^{23} atoms/cm^3) localized below the surface is found to be short lived during ~1.5 ps. At later times, the expanding HDP (>>100 eV and ~10^{23} atoms/cm^3) forms below and above the original surface of solid Ge material.

Atomic data for Ge atoms and ions are calculated using the HFS model. The detailed information on the ionization potential of atomic electrons, energies of atomic levels, energies and wavelengths of radiative transitions, and many other atomic parameters are stored in a dataset. These data serve as the basis in the computational models for calculating the radiative transfer and electrical conductivity of WDP. The CRSS model that utilized the atomic data of Ge atoms and ions was used to predict the WDP ionization balance. The ionization of four outer electrons from 4s and 4p Ge shells that results in the charge state z ~ 4 is observed for solid-state Ge at temperatures ~1-10 eV. The charge state of WDP increases with further increase in temperature reaching z ~ 11 at temperature of 100 eV. The ionic composition of the solid-density Ge WDP

ranges from Ge V to Ge XV ions in the temperature range from 1 to 100 eV. The emission spectra of Ge WDP demonstrate that there is greater X-ray emission in soft X-ray and UV ranges, and shift of X-ray emission in spectral lines to shorter wavelengths with the increase in temperature. The suppression of X-ray and UV emission in spectral lines occurs with the increase in density. It is vanished at the solid-state density of WPD.

The radiative transfer in the expanding WDP/HDP is studied. The calculated emission coefficients (HFS-CRSS model) and profiles of density and temperature along the depth of Ge material (MSM-MD model) were used as an input data in the MCOURT code. At early times (< 1 ps) of Ge WDP expansion, it is observed that below the original surface, there is a large region of Ge WDP with solid density, 5.323 g/cm^3, and relatively high temperature, ~6 - 70 eV. A significant portion of emitted radiation is redeposited into a solid-density plasma. The absorbed power density within the solid-density region is much higher than the power density emitted into vacuum. At later times (≥ 5 ps) of Ge WDP expansion, the density drops several times and temperature rises to keV range below the original surface. The rates of emission, absorption, and escape of radiation increase by several orders of magnitude. The absorption of radiation becomes lower in the bulk Ge WDP compared to the emission of radiation, but the absorption overcomes the emission in the vicinity of the front of expanding plasma. The radiation emission from a considered plasma volume into a vacuum and into a bulk Ge material becomes comparable. The spectral energy flux of photons emitted into a vacuum covers a range from near-infrared light to hard X-rays. At later times ~10 ps, X-ray portion of spectrum extends to the region of shorter wavelengths with the emission of X-rays in characteristic spectral lines. The redistribution of energy in Ge WDP and

HDP due to the radiative transfer is found to be quite important phenomenon that should be taken into account in the modeling, especially on the early stages of Ge WDP expansion.

The LMR model is developed, implemented into the REODP code, and used for calculating the electrical conductivity of Si and Ge WDPs. The ionic composition, free electron density, and average charge state in WDP calculated from the HFS-CRSS model are used as an input data in the LMR model. This model is able to accurately treat the interactions of electrons with atoms and ion species, and it takes into account the Coulomb coupling between ions that is quite important in the WDP regime. In order to validate the developed LMR model, the REODP-calculated average charge and electrical conductivity of Al and Fe WDPs are benchmarked against the measured and calculated data available in the literature. A reasonable agreement with measured data and other computational results is found. The average charge state and electrical conductivity of Si and Ge WDPs are then calculated in a wide range of densities for temperatures of 10000 K, 20000 K, and 30000 K. The analysis in density-temperature space shows that the average charge of Si and Ge WDPs decreases with increasing density, reaches a minimum, and then increases rapidly toward a value of 4 due to the pressure ionization. The average charge increases with increasing temperature at densities lower the solid-state density of WDP. The analysis of the electrical conductivity of Si and Ge WDPs in density-temperature space demonstrates its decrease with increasing density in low-density region, passage through a minimum, and then a sharp increase due to the pressure ionization. The electrical conductivity increases with increasing temperature.

References

[1] A.R. Jha, Solar Cell Technology and Applications, Taylor and Francis Group, Boca Raton, London, New York, 2010.

[2] E.E. Conrad, G.A. Gurtman, G. Kweder, M.J. Mandell, W.W. White, Collateral damage to satellites from an EMP attack, Defense Threat Reduction Agency report, DTRA-1R-10-22, (2010).

[3] H.L. Abrams, Nuclear Radiation in Warfare - Rodblat,J, Am Sci, 71 (1983) 422-422.

[4] P. Dressman, G. Miloshevsky, Soft X-ray depth-dose profiles in satellite surface materials, 2018 IEEE International Conference on Plasma Science (ICOPS), IEEE, 2018, pp. 1-1.

[5] M. Fogleman, C. Wenzel, G. Miloshevsky, Dynamics and Properties of High-Density Surface Plasmas Induced by Cold X-rays, The 10-th International Workshop on Warm Dense Matter (WDM 2019), Travemünde, Germany, 2019.

[6] G. Miloshevsky, Comparison of Equations of State for Warm and Hot Dense Matter from REODP and PIMC Modeling, APS Division of Plasma Physics Meeting Abstracts 2021, Pittsburgh, PA, 2021, pp. JO03.014.

[7] J.J. Barnard, J. Armijo, R.M. More, A. Friedman, I. Kaganovich, B.G. Logan, M.M. Marinak, G.E. Penn, A.B. Sefkow, P. Santhanam, P. Stoltz, S. Veitzer, J.S. Wurtele, Theory and simulation of warm dense matter targets, Nucl Instrum Meth A, 577 (2007) 275-283.

[8] D.O. Gericke, K. Wunsch, A. Grinenko, J. Vorberger, Structural Properties of Warm Dense Matter, J Phys Conf Ser, 220 (2010) 012001.

[9] E.G. Saiz, G. Gregori, D.O. Gericke, J. Vorberger, B. Barbrel, R.J. Clarke, R.R. Freeman, S.H. Glenzer, F.Y. Khattak, M. Koenig, O.L. Landen, D. Neely, P. Neumayer, M.M. Notley, A. Pelka, D. Price, M. Roth, M. Schollmeier, C. Spindloe, R.L. Weber, L. van Woerkom, K. Wunsch, D. Riley, Probing warm dense lithium by inelastic X-ray scattering, Nat Phys, 4 (2008) 940-944.

[10] A.N. Souza, D.J. Perkins, C.E. Starrett, D. Saumon, S.B. Hansen, Predictions of x-ray scattering spectra for warm dense matter, Phys Rev E, 89 (2014) 023108.

[11] D. Kalantar, R. Lee, J. Molitoris, Warm Dense Matter: An Overview, The LLNL Warm Dense Matter Workshop, Lawrence Livermore National Laboratory, Livermore, CA, 2004.

[12] M. Koenig, A. Benuzzi-Mounaix, A. Ravasio, T. Vinci, N. Ozaki, S. Lepape, D. Batani, G. Huser, T. Hall, D. Hicks, Progress in the study of warm dense matter, Plasma Physics and Controlled Fusion, 47 (2005) B441.

[13] F. Graziani, M.P. Desjarlais, R. Redmer, S.B. Trickey, Frontiers and challenges in warm dense matter, Springer Science & Business2014.

[14] D. Saumon, C. E. Starrett, J. A. Anta, W. Daughton, G. Chabrier, The structure of warm dense matter modeled with an average atom model with ion-ion correlations, arXiv:1311.3986, (2013).

[15] G. Miloshevsky, A. Hassanein, Atomic and optical properties of warm dense copper, Phys Rev E, 92 (2015) 033109.

[16] A. McEvoy, T. Markvart, L. Castañer, T. Markvart, L. Castaner, Practical handbook of photovoltaics: fundamentals and applications, Elsevier2003.

[17] J.E. Granata, J.H. Ermer, P. Hebert, M. Haddad, R.R. King, D.D. Krut, J. Lovelady, M.S. Gillanders, N.H. Karam, B.T. Cavicchi, Triple-junction GaInP/GaAs/Ge solar cells-production status, qualification results and operational benefits, Conference Record of the Twenty-Eighth IEEE Photovoltaic Specialists Conference-2000 (Cat. No. 00CH37036), IEEE, 2000, pp. 1181-1184.

[18] J. Li, A. Aierken, Y. Liu, Y. Zhuang, X. Yang, J. Mo, R. Fan, Q. Chen, S. Zhang, Y. Huang, A brief review of high efficiency III-V solar cells for space application, Frontiers in Physics, 8 (2021) 631925.

[19] D. Dance, G.A. Carlsson, INTERACTIONS OF PHOTONS, CRC Press, Boca Raton, 2007.

[20] H. Hall, The theory of photoelectric absorption for x-rays and γ-rays, Rev Mod Phys, 8 (1936) 358.

[21] S.M. Stewart, R.B. Johnson, Blackbody radiation: A history of thermal radiation computational aids and numerical methods, CRC Press2016.

[22] J. Allison, K. Amako, J. Apostolakis, P. Arce, M. Asai, T. Aso, E. Bagli, A. Bagulya, S. Banerjee, G. Barrand, Recent developments in Geant4, Nuclear instruments and methods in

physics research section A: Accelerators, Spectrometers, Detectors and Associated Equipment, 835 (2016) 186-225.

[23] https://geant4.web.cern.ch/.

[24] J. Apostolakis, M. Pia, S. Giani, P. Nieminen, M. Maire, L. Urbán, Geant4 low energy electromagnetic models for electrons and photons, 1999.

[25] G. Miloshevsky, J.A. Caffrey, Electron deposition and charging analysis for the Europa Lander Deorbit Stage, NASA/TM-2019-220139 Technical Report, 2019, pp. 57-67.

[26] G. Miloshevsky, A. Hassanein, Energy-angle correlation of neutrons and gamma-rays emitted from an HEU source, Nucl Instrum Meth A, 749 (2014) 47-56.

[27] J.G. Lockwood, E.L. Ruggles, H.G. Miller, A.J. Halbleib, Calorimetric measurement of electron energy deposition in extended media - Theory vs experiment, Sandia National Laboratories report SAND79-0414, Albuquerque, New Mexico, 1987.

[28] E. Furio, A molecular dynamics primer, International School for Advanced Studies, Italy, (1997).

[29] S. Reich, Numerical Simulation in Molecular Dynamics: Numerics, Algorithms, Parallelization, Applications, SIAM Review, 52 (2010) 213.

[30] http://lammps.sandia.gov/.

[31] A.P. Thompson, H.M. Aktulga, R. Berger, D.S. Bolintineanu, W.M. Brown, P.S. Crozier, P.J. in't Veld, A. Kohlmeyer, S.G. Moore, T.D. Nguyen, LAMMPS-a flexible simulation tool for

particle-based materials modeling at the atomic, meso, and continuum scales, Computer Physics Communications, 271 (2022) 108171.

[32] M.S. Daw, M.I. Baskes, Embedded-atom method: Derivation and application to impurities, surfaces, and other defects in metals, Phys Rev B, 29 (1984) 6443.

[33] J. Tersoff, New empirical approach for the structure and energy of covalent systems, Phys Rev B, 37 (1988) 6991.

[34] J. Tersoff, Empirical interatomic potential for silicon with improved elastic properties, Phys Rev B, 38 (1988) 9902.

[35] J. Tersoff, New empirical model for the structural properties of silicon, Physical review letters, 56 (1986) 632.

[36] S. Sonntag, C. Trichet Paredes, J. Roth, H.R. Trebin, Molecular dynamics simulations of cluster distribution from femtosecond laser ablation in aluminum, Applied Physics A, 104 (2011) 559-565.

[37] J. Roth, S. Sonntag, J. Karlin, C.T. Paredes, M. Sartison, A. Krauß, H.-R. Trebin, Molecular dynamics simulations studies of laser ablation in metals, AIP Conference Proceedings, American Institute of Physics, 2012, pp. 504-523.

[38] A. Miloshevsky, M.C. Phillips, S.S. Harilal, P. Dressman, G. Miloshevsky, Generation of nanoclusters by ultrafast laser ablation of Al: Molecular dynamics study, Physical Review Materials, 1 (2017) 063602.

[39] http://www.openrasmol.org/doc/rasmol.html.

[40] G.V. Miloshevsky, V.I. Tolkach, S. Rozin, G. Shani, Elastic scattering of electrons by gadolinium and barium atoms, Nucl Instrum Meth B, 168 (2000) 467-472.

[41] S.S. Harilal, G.V. Miloshevsky, T. Sizyuk, A. Hassanein, Effects of excitation laser wavelength on Ly-alpha and He-alpha line emission from nitrogen plasmas, Phys Plasmas, 20 (2013) 013105

[42] C.F. Fischer, Self-Consistent-Field (Scf) and Multiconfiguration (Mc) Hartree-Fock (Hf) Methods in Atomic Calculations - Numerical-Integration Approaches, Comput Phys Rep, 3 (1986) 273-326.

[43] C.D. Sherrill, H.F. Schaefer, The configuration interaction method: Advances in highly correlated approaches, Advances in Quantum Chemistry, 34 (1999) 143-269.

[44] V. Tolkach, V. Morozov, A. Hassanein, Development of comprehensive models for opacities and radiation transport for IFE systems, Argonne National Laboratory, 2002.

[45] G. Miloshevsky, Composition and Optical Properties of Warm Dense Germanium Plasma, 2021 Virtual IEEE International Conference on Plasma Science (ICOPS), 2021.

[46] A. Ishii, N. Ohnishi, H. Nagakura, H. Ito, S. Yamada, Parallel computing of radiative transfer in relativistic jets using Monte Carlo method, High Energ Dens Phys, 9 (2013) 280-287.

[47] J.M. Marr, F.P. Wilkin, A better presentation of Planck's radiation law, Am J Phys, 80 (2012) 399-405.

[48] R. Zollweg, R. Liebermann, Electrical conductivity of nonideal plasmas, J Appl Phys, 62 (1987) 3621-3627.

[49] D.K. Kim, I. Kim, Calculation of ionization balance and electrical conductivity in nonideal aluminum plasma, Phys Rev E, 68 (2003) 056410.

[50] M.R. Zaghloul, A simple theoretical approach to calculate the electrical conductivity of nonideal copper plasma, Phys Plasmas, 15 (2008) 042705.

[51] Z.J. Fu, W.L. Quan, W. Zhang, Z.G. Li, J. Zheng, Y.J. Gu, Q.F. Chen, Equation of state and transport properties of warm dense aluminum by ab initio and chemical model simulations, Phys Plasmas, 24 (2017) 013303.

[52] M.R. Zaghloul, On the Cutoff Distance and the Classical Energy-Averaged Electron–Ion Momentum Transport Cross Section in Ideal and Nonideal Plasmas, Ieee T Plasma Sci, 46 (2018) 390-394.

[53] M.R. Zaghloul, On the Calculation of the Electrical Conductivity of Hot Dense Nonideal Plasmas, Plasma Physics Reports, 46 (2020) 574-586.

[54] A.N. Mostovych, Y. Chan, Reflective probing of the electrical conductivity of hot aluminum in the solid, liquid, and plasma phases, Phys Rev Lett, 79 (1997) 5094.

[55] I. Krisch, H.-J. Kunze, Measurements of electrical conductivity and the mean ionization state of nonideal aluminum plasmas, Phys Rev E, 58 (1998) 6557.

[56] A.W. DeSilva, J.D. Katsouros, Electrical conductivity of dense copper and aluminum plasmas, Phys Rev E, 57 (1998) 5945-5951.

[57] J. Benage, W. Shanahan, M. Murillo, Electrical resistivity measurements of hot dense aluminum, Phys Rev Lett, 83 (1999) 2953.

[58] J.F. Benage Jr, Review of electrical resistivity measurements of dense aluminum and comparison to theory, Phys Plasmas, 7 (2000) 2040-2045.

[59] L. Spitzer Jr, R. Härm, Transport phenomena in a completely ionized gas, Phys Rev, 89 (1953) 977.

[60] J.M. Ziman, Principles of the Theory of Solids, Cambridge university press, London, 1972.

[61] S. Ichimaru, S. Tanaka, Theory of interparticle correlations in dense, high-temperature plasmas. V. Electric and thermal conductivities, Physical Review A, 32 (1985) 1790.

[62] Y.K. Kurilenkov, A. Valuev, The electrical conductivity of plasma in wide range of charge densities, Beiträge aus der Plasmaphysik, 24 (1984) 161-171.

[63] Y.T. Lee, R. More, An electron conductivity model for dense plasmas, The Physics of fluids, 27 (1984) 1273-1286.

[64] Z. Djurić, A.A. Mihajlov, V. Nastasyuk, M. Popović, I. Tkachenko, Coulomb conductivity of strongly coupled plasmas, Physics Letters A, 155 (1991) 415-418.

[65] W. Ebeling, A. Förster, V. Fortov, V. Gryaznov, A.Y. Polishchuk, Thermophysical properties of hot dense plasmas, Teubner Verlagsgesellschaft, Stuttgart, 1991.

[66] G.A. Rinker, Electrical conductivity of a strongly coupled plasma, Phys Rev B, 31 (1985) 4207.

[67] M. Desjarlais, J. Kress, L. Collins, Electrical conductivity for warm, dense aluminum plasmas and liquids, Phys Rev E, 66 (2002) 025401.

[68] M. Mitchner, C.H. Kruger Jr, Partially ionized gases, Wiley, New York, 1973.

[69] K. Günther, R. Radtke, Electric properties of weakly nonideal plasmas, De Gruyter, Basel, 1984.

[70] M.P. Desjarlais, Practical improvements to the Lee-More conductivity near the metal-insulator transition, Contrib Plasm Phys, 41 (2001) 267-270.

[71] G. Maroulis, Atoms, Molecules and Clusters in Electric Fields: Theoretical Approaches to the calculation of electric polarizability, World Scientific2006.

[72] I. Bespalov, A.Y. Polishchuk, Method for calculating the degree of ionization and the thermal and electrical conductivity over a wide range of density and temperature, Sov. Tech. Phys. Lett, 15 (1989) 39-41.

[73] C.A. Iglesias, P.A. Sterne, Fluctuations and the ionization potential in dense plasmas, High Energ Dens Phys, 9 (2013) 103-107.

[74] S. Kuhlbrodt, R. Redmer, Electrical conductivity of dense aluminium fluid, J Phys a-Math Gen, 36 (2003) 6027-6032.